Impact ionization in $AlAs_{0.56}Sb_{0.44}$ photodiodes

Xin Yi

A thesis submitted for the degree of Doctor of Philosophy

Department of Electronic and Electrical Engineering
The University of Sheffield

January 2020

Contents

Acknowledgements

I would like to thank, first and foremost, my supervisor Professor John P. R. David for his invaluable guidance and encouragement. This work would not have been possible without his supervision and support. He used countless time explaining the fundamental aspects of semiconductors especially about impact ionization theory. I would also like to thank Professor Jo S. Ng and Professor Chee H. Tan for their supervision.

I am thankful to Dr. Baolai Liang for providing the technology of growth, and I also deeply appreciate the support from Dr Shiyu Xie. I would like to thank Dr Xinxin Zhou for the initial stage works and valuable guidance. My appreciation is also extended to L. W. Lim, Dr J. S. Cheong, Dr S. Dimler and Dr P. Lucas for their fabrication, modelling, experimental set-up help and countless discussions.

Thanks are also due to entire members of the Impact Ionization Group (2015 - 2019) at the University of Sheffield for their assistance, especially Yuchen Liu.

I would like to thank H.Y. Liu and J.W. Zhuang for everything. I deeply appreciate the help from my friends.

Finally and most importantly, I am truly indebted to my parents for their constant financial and emotional support I also extend my thanks to all my family members. Because of your support, I can achieve it.

Abstract

The aim of this work is to characterize the impact ionization characteristics of $AlAs_{0.56}Sb_{0.44}$ towards its use as the avalanche medium in separate absorption and multiplication avalanche photodiodes (SAM-APDs) based on InP substrate for optical communication systems. The previous studies of the $AlAs_{0.56}Sb_{0.44}$ material were only undertaken on very thin p-i-n structures where we cannot accurately estimate the impact ionization coefficient and excess noise behavior due to "dead-space" effects. In this work, much thicker $AlAs_{0.56}Sb_{0.44}$ homojunction diodes were investigated systematically. The absorption coefficient was fitted by 1-D quantum efficiency model. Comprehensive multiplication and excess noise measurements based on $AlAs_{0.56}Sb_{0.44}$ homojunction diodes over a wide range of thickness were performed at room temperature. The bulk electron and hole ionization coefficients, α and β respectively, were found to be very disparate and 'silicon like' at low electric fields and $\alpha > \beta$ over the whole electric field range. The ionization coefficients were determined from 220-1250 kV/cm for α and from 360-1250 kV/cm for β. The β was found to rapidly drop at the low electrical field, but the α was similar to that of InP and InAlAs. Noise measurements carried out on the thickest p-i-n structure exhibits the best reported excess noise based on InP substrate, $k = 0.005$ at room temperature. The SAM-APDs using AlAsSb show potentially better performance than those using InP/InAlAs as the multiplication layer.

Publications

JOURNAL PUBLICATIONS

1. **X. Yi**, S. Xie, B. Liang, L. W. Lim, J. S. Cheong, M. C. Mukul, D. L. Huffaker, C. H. Tan & J. P. R. David, "Extremely low excess noise and high sensitivity $AlAs_{0.56}Sb_{0.44}$ avalanche photodiodes," *Nature Photonics*, vol. 13, pp. 683–686, 2019.
2. **X. Yi**, S. Xie, B. Liang, L. W. Lim, X. Zhou, M. C. Mukul, D. L. Huffaker, C. H. Tan & J. P. R. David, "Demonstration of large ionization coefficient ratio in $AlAs_{0.56}Sb_{0.44}$ lattice matched to InP", *Scientific Reports*, vol. 8, pp. 9107, 2018.

CONFERENCE PRESENTATIONS

1. **X. Yi**, S. Xie, B. L. Liang, L. W. Lim, D. L. Huffaker, C. H. Tan & J. P. R. David, "High performance $AlAs_{0.56}Sb_{0.44}$ avalanche photodiodes" SPIE Photonics West 2020, San Francisco, California, United States, 01/02/2020.

2. S. Xie, **X. Yi**, B. L. Liang, L. W. Lim, D. L. Huffaker, C. H. Tan & J. P. R. David, "High speed and high sensitivity $AlAs_{0.56}Sb_{0.44}$ avalanche photodiodes" Asia Communication Photonics, Chengdu, China, 02/11/2019.

3. D. L. Huffaker, S. Xie, **X. Yi**, B. L. Liang, L. W. Lim, C. H. Tan & J. P. R. David, "Large ionization coefficient ratio in $AlAs_{0.56}Sb_{0.44}$ avalanche photodiodes" Compound Semiconductor Week 2019, Kasugano International Forum, Nara, Japan, 19/05/2019

4. S. Xie, **X. Yi**, B. L. Liang, C. H. Tan, J. P. R. David & D. L. Huffaker, "AlAsSb avalanche photodiodes with high gain-bandwidth product over 300 GHz" Semiconductors and Integrated Opto-Electronics, Cardiff, UK, 16/04/2019

5. **X. Yi**, S. Xie, B. Liang, L. W. Lim, X. Zhou, M. C. Mukul, D. L. Huffaker, C. H. Tan & J. P. R. David, "Avalanche multiplication in $AlAs_{0.56}Sb_{0.44}$" Asia Communications and Photonics Conference, Hangzhou, China, 26/10/2018

6. S. Xie, **X. Yi**, B. L. Liang, L. W. Lim, X. Zhou, M. C. Debnath, C. H. Tan, J. P. R. David & D. L. Huffaker, "Breakdown voltages in $AlAs_{0.56}Sb_{0.44}$ avalanche photodiodes" UK Semiconductors, Sheffield, UK, 04/07/2018

7. **X. Yi**, Y. Liu, Z. Zhou, F. Harun, R. D. Richards, C. H. Tan & J. P. R. David, "Modification of hole ionization coefficients in GaAsBi based avalanche photodiodes" Semiconductors and Integrated Opto-Electronics, Cardiff, UK, 18/04/2017

CHAPTER 1:

INTRODUCTION

1.1 Overview

Photonics technology is widely used in retail, healthcare, transport and telecommunications and will more and more be embeded in artificial intelligence, the internet of things, cybersecurity, and quantum technologies. Without next-generation high speed and high sensitive sensors and cameras, such data transport would not be possible. In the future, the requirement of speed, data capacity and security is key to the digital transformation. The emerging field of telecommunication depends strongly on photonics technologies. Since the internet started to be used in 1993 [1], the global telecommunication market has been driven by new-generation telecommunication systems such as wireless communication and satellite communication. Transmission using an optical carrier wave guided along a glass fibre, called optical fibre transmission system, has various advantages, for example, large bandwidth, small size, long-distance transmission and low price. This technology can be used to address the limitations of radio frequency communications. Figure 1.1(a) shows a simplified optical fibre transmission system including optical transmitters, optical amplifiers, fibre cables and optical receivers operating in the near/short-wave infrared region (0.8 to 1.6 μm). A variety of semiconductor devices such as light-emitting diodes (LED) and laser diodes, can be used as an optical transmitter with little cost. Compared with an LED, the laser provides a higher output power, a narrower spectral width and higher rates; however it is more costly. Two factors that limit the maximum travel distance of the light are the power loss and the distortion. A high-quality fibre cable and amplifiers that directly amplify the optical single without converting the optical signal back into an electrical format are necessary for the whole system. Amplifiers are especially crucial for long-distance transmission. Receivers are used to convert optical signals into electrical signals so that the data can be extracted, and it is a crucial part of any optical telecommunication and LiDAR system. Over the past decade, the channel data rate has gone from 2.5 Gb/s to

10 Gb/s, and 40 Gb/s is under development. The next-generation standard for Ethernet requires speeds of 100 and 400 Gb/s. The next-generation system needs long-distance transmission and low cost per bit is also a significant factor. Free-space optics (FSO) system is a wireless communication technology where free space or air act as the medium for speed-of-light data transmission rather than guided through an optical fibre. The fundamental theory of FSO is essentially the same as that for fibre optic transmission, and it is capable of sending data up to 2.5 Gb/s. FSO links have many advantages like license-free bands, high data-rate transmission (≥ Gbps), and negligible signal interferences. The principal limiting issues are weather condition, background light sources, beam dispersion, and pollution.

Light detection and ranging (LIDAR) applications are used to measure the distance between the sensor and the target object accurately and is one of the significant increasing markets. Use of near/short-wave infrared laser pulses provides accurate continued photons, and an optical receiver detects the reflected photons. Then the distance can be calculated from the arrival time of the photons and the speed of light. It is widely used in autonomous vehicles, industrial robots, mapping & surveying, drones, and renewable energy. The market of laser-based distance measurement is expecting to achieve 921.2 million by 2022, as shown in Figure 1.1(b) [2].

(a)

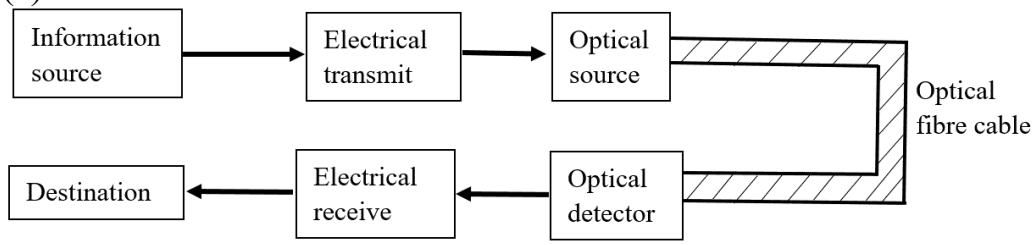

(b)

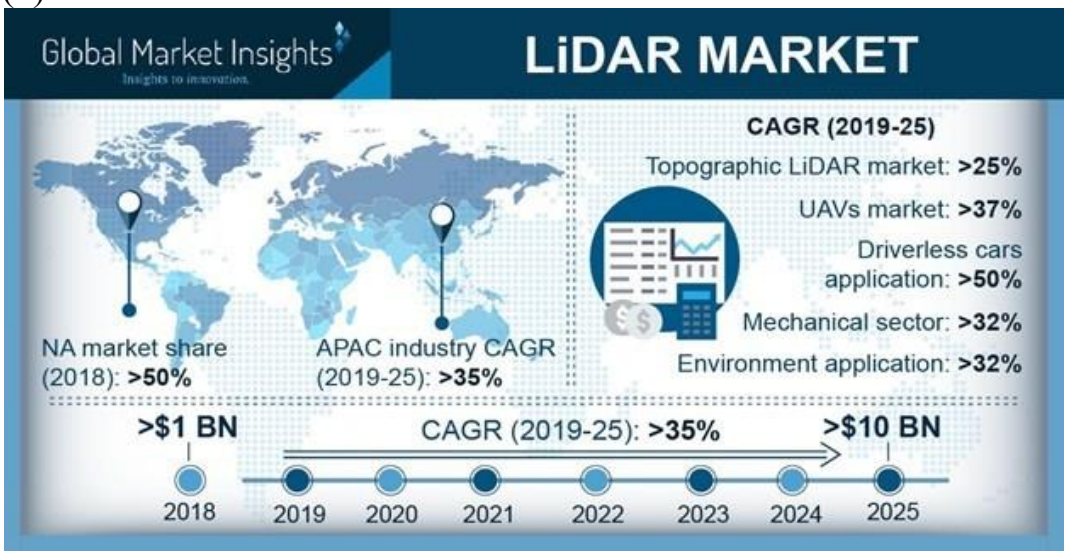

Figure 1.1. (a) The optical fibre communication system. (b) LiDAR market [2].

1.2 Photodetector

A photon with energy hf, where h is Planck's constant and f is frequency, is absorbed in a semiconductor when this energy is bigger than the bandgap of the semiconductor. Therefore, a free electron is introduced to the conduction band, E_c, while a free hole stays in the valance band, E_v. This is called the photoelectric effect. Photodetectors utilise the photoelectric effect and provide demodulation of the optical carriers and are at the heart of the receiver. Examples of photodetectors are photodiodes (p-n, p-i-n, or avalanche photodiodes), phototransistors and photoconductors. Photodetectors currently in use or under research for optical communication receivers must satisfy very stringent requirements such as high sensitivity at the operating wavelengths, high fidelity, suitable bandwidth, low noise, low bias, small size, stability, high reliability and

low cost. The incoming signal usually is weak and needs amplification. Avalanche photodiodes (APDs) are the most popular choice in optical communication applications due to their internal gain mechanism. Moreover, they have already been widely used by developing high speed and high sensitivity performance over the past five decades. The primary performance metric of a photodetector is determined by

1. Quantum efficiency, η

   The quantum efficiency is defined as the number of electron-hole pairs generated per incident photons. One of the critical factors is the absorption coefficient of the absorber. A low quantum efficiency can be caused by minority carrier recombination, low absorption coefficient, or reflection. The quantum efficiency can be expressed as

   $$\eta = \frac{\text{Number of electrons collected}}{\text{Number of incident photons}} \qquad (1.1)$$

   The related but more often used characteristic is responsivity, R. It is defined as the ratio of generated photocurrent over incident optical power, P and is calculated using

   $$R = \frac{I_{ph}}{P} = \frac{\eta q \lambda}{hc} \qquad (1.2)$$

   Where q is the electron charge and λ is wavelength. From quantum efficiency, we can also identify the photo-response region.

2. Response speed

   The response speed is a crucial parameter for a photodetector, which is limited by carrier diffusion time, carrier drift time, and capacitance of the depletion region. Carriers have to diffuse to the electrical field region if generated outside of the depletion region resulting in a longer response time. Carriers drift in the depletion region at their saturation velocities after applying sufficient reverse bias. The wider the depletion region, the longer the time spent here. If the depletion region is too thin, the $R_L C$ time constant will dominate speed, where R_L is the load resistance and C is the capacitance.

3. Device noise

Noise is also a significant parameter for photodetector as it determines the minimum detectable signal strength. The dark current, temperature, background radiation and internal device noise can limit the signal to noise ratio (SNR). The SNR can be expressed as [3]

$$SNR = \frac{P_{opt}}{N_s + N_{amp}}, \qquad (1.3)$$

Where P_{opt} is the signal power, N_s is shot noise, and N_{amp} is amplifier noise.

1.3 Device types

A wide choice of photodetectors for optical communication receivers are available, such as photoconductor, Photomultiplier Tube (PMT), phototransistor and photodiode (PD). A photoconductor includes a slab of semiconductor, with ohmic contacts in the opposite ends. The conductivity changes when the photoelectric effect illuminates it. The gain of a photoconductor, M, is expressed as

$$M = \frac{\tau}{T_{tr}} \qquad (2.1)$$

Where τ is the carrier lifetime and T_{tr} is the transit time. Photoconductors have been attractive for their simple structure, relatively low operating bias and high responsivity [4]. However, they suffer from long response time [5, 6]. There are photoconductors available for applications covering from visible to far-infrared (> 20 μm) wavelengths.

PMT is one of the external photoelectric devices to operate in the near-infrared region. They use high vacuum glass tubes with a photosensitive surface, an electron multiplier and output terminal. The advantages of PMTs are high gain, typically between 10^5 – 10^8 [7], low dark current and low noise, but high voltage for operation. The PMT is not suitable for optical receivers due to it is being incompatible with microelectronic monolithic integration in these systems and without a suitable work function for 1.3 - 1.5 μm wavelength light.

Phototransistors were demonstrated in 1953 and can sense light levels (μW). Phototransistors using III-V materials or heterojunctions have high gain and low noise, however, they have less bandwidth. This is because there is a large capacitance between base and collector junction, triggered by a large junction area.

p-i-n photodiodes (PDs) and avalanche photodiodes (APDs) are a popular choice for telecommunication applications. PDs and APDs typify the internal photoelectric device but APDs are normally operated at near the breakdown voltage. Nowadays, optoelectronic devices based on Si, Ge and III-V alloys can operate from ultra-violet to infrared wavelength, while providing high-sensitivity, high-speed response and low costs.

A typical p-i-n PD, shown in Figure 1.2, is grown on a lattice-matched substrate with fabricated metal contacts at both of the terminals. An intrinsic region is between the p^+ and n^+ layer. The thickness of i-region determines the quantum efficiency due to the increase of the volume of the absorbent material, and the doping of the i-region determines the electric field profile. The i-region must be fully depleted by applied reverse electrical field, V, cross PD to collect more photons. After carriers are generated in the i-region, they are swept to the p^+ and n^+ region by the electric field. The electric field is typically a constant value in the i-region due to low doping density and should be lower than the value need for triggering impact ionization and also enough maintain the saturated drift velocity. The disadvantage of PDs is poor sensitivity.

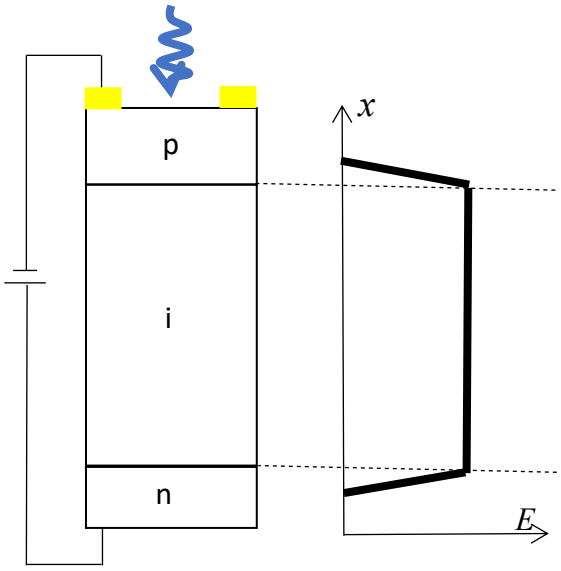

Figure 1.2. Electric field and photogeneration profile of a p-i-n structure.

Impact ionization in a semiconductor is one of carrier generation process which is usually observed at a high electric field. APDs is one importation application for impact ionization. Their fundamental advantage compared to standard p-i-n PDs is that they enable internal amplification of weak signals (internal multiplication/gain, M), but at the cost of additional excess noise (F). Excess noise happens because impact ionization is a stochastic process that introduces fluctuation in the overall gain value. We express the impact ionization process using impact ionization coefficients of electron and hole (α for electron and β for hole, α/β). The impact ionization ratio, α/β ratio, directly determines the gain-bandwidth products and the excess noise performance of an APD. A large α/β ratio is desirable for high-speed and high-sensitive APDs [8, 26]. A large amount of effort has been expended to reduce the excess noise of APDs and the disadvantage of excess noise for a receiver is discussed in the following section. The easiest way for achieving low noise performance is to select a bulk material with large electron and hole impact ionization coefficient ratio while initiating the impact ionization process by the higher ionizing carrier type [9]. The second way to achieve low excess noise is by reducing the multiplication region to take advantage of the non-local property of impact ionization [10-15]. Thirdly, people designed heterojunction structures to achieve low excess noise [16-20].

A Separate Absorption and Multiplication (SAM)-APD lattice-matched to InP substrates is one of the typical modern telecommunication-wavelength APDs which is used to achieve high multiplication, and low excess noise characteristics. Figure 1.3 shows the structure and the electric field in a commercial vertically illuminated SAM-APD. An optical signal injects from the top or backside. These APDs require the use of a narrow bandgap material to detect long wavelengths. However, narrow bandgap materials are not suitable for avalanche process due to tunnelling current at high reverse bias and the limitation of the α/β ratio. So we only use it as an absorber while a relatively wide bandgap multiplication material replaces the narrow bandgap material as the multiplication region. The absorption and multiplication layers are usually unintentionally doped (or lightly doped). It is necessary to keep the electric-field across the absorption region as low as possible to avoid tunnelling but thick enough to achieve a high quantum efficiency. There is also a charge sheet layer with a precisely controlled doping concentration and thickness between absorption and multiplication layers. This layer will allow us to go from a high electric-field in the multiplication layer offering enough

energy to undergo ionization process to a low electric field in the absorption layer avoiding tunnelling current. In the conventional vertically illuminated APDs, the first trade-off is between the quantum efficiency and the bandwidth. A shorter depletion width can provide a shorter transit time to enhance the -3 dB bandwidth, but the thinner absorption region will reduce quantum efficiency. The second trade-off is between the transit time and the RC-limited bandwidth.

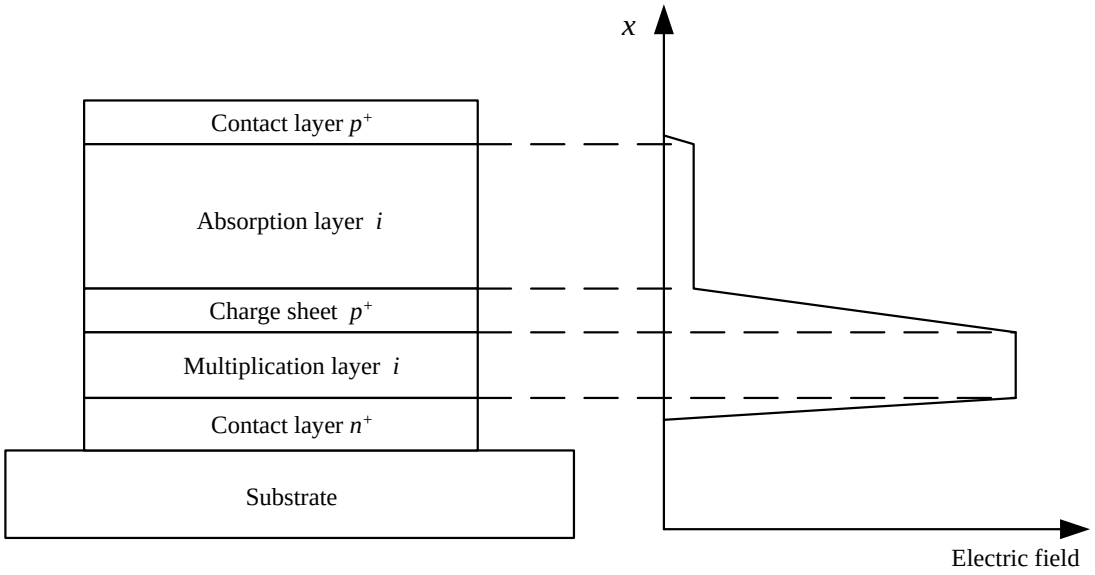

Figure 1.3. Schematic SAM-APD structure and its electric field profile.

Devices discussed in this thesis operate in the linear model. Nevertheless, APDs/SAM-APDs can operate in the Geiger mode, where the devices operate above the breakdown voltage. A Geiger mode APD is capable of detecting at a single photon level used in many cutting-edge light detection applications such as three-dimensional laser detection and ranging, single photon counting and quantum communication protocols [21-25].

1.4 Competing material for telecommunication application

The performance of semiconductor devices is mainly dependent on the physics of semiconductor materials, and the following section is a literature review of avalanche materials.

In 1966, optical fibre was used in optical communication by Kao and Hockham [27], to avoid degradation of the optical signal by the atmosphere. Initially, with the successful development of the AlGaAs based lasers, the operation wavelength was between 0.8 and 0.9 μm. Therefore, GaAs (E_g ~ 1.42 eV) and Si (E_g ~ 1.12 eV) are suitable materials to operate at such wavelengths. Si-based devices dominate the market in terms of volume due to their widely different ionization coefficients, very low excess noise, unrivalled technological maturity and low cost. However, these devices are limited by the detection of the near-infrared light. Nowadays, the driving force behind APDs has been the development of next-generation lightwave communication systems using the low-attenuation and low-dispersion wavelength of 1.31 and 1.55 μm of silica optical fibres. People recently utilised Ge (E_g ~ 0.67 eV) as the absorber in Si [28-30] to satisfy the longer wavelength requirement, but the lattice mismatch issue introduces a high dark current level ~ 10^{-5} A/cm^2 reducing its sensitivity. With the successful development of InAs/GaAs quantum dots on GaAs substrates [31, 32], and the successful growth of InGaAs nanopillar on GaAs substrates [33], optical detection at 1.31 and 1.55 μm is now possible on the GaAs platform, too.

Mercury Cadmium Telluride (HgCdTe) APDs with bandgap less than ~ 0.55 eV have been reported with ideal impact ionization characteristics where the hole ionization coefficient is found to be approximately zero at room temperature and an extremely low excess noise factor of 1-1.5 [34-36] is measured. However, they are grown on small and expensive substrates and tend to be used in high-end instruments for space and military applications. The primary driving force of developing InAs APDs (E_g ~ 0.34 eV) is a similar band structure with HgCdTe. Interestingly, the reported results showed comparable performance to HgCdTe. Several groups have demonstrated that extremely low excess noise of $F < 2$ can be measured in the mesa and planar device [37-41]. Frequency responses measured at room temperature shows a high gain-bandwidth product of 580 GHz [42]. However, the high dark leakage current, relative expensive substrates, sophisticated growth technology and temperature-sensitivity limit it for further development.

Recently, people have extended their research to $Al_xIn_{1-x}As_ySb_{1-y}$ lattice-matched to the GaSb substrate. Researchers at the University of Texas have thoroughly investigated this alloy material. Woodson M.E. et al. [43] demonstrated for the first time extremely

low excess noise with a *k*-value (β/α) of 0.015 and a peak quantum efficiency of 68% at 735 nm from the $Al_{0.7}In_{0.3}As_{0.3}Sb_{0.7}$ diode with 890 nm i-region grown by digital alloy growth technique. They attributed the reduction in β to high phonon scattering rates and the heavy effective hole mass associated with the large Antimony element, and recently reported a mini-gap hypothesis. The photo-response results demonstrated that over 60% Aluminium in $Al_xIn_{1-x}As_ySb_{1-y}$ could detect traditional telecommunication wavelengths (1.3 or 1.5 μm). However, the small bandgap when growing <50% Aluminium introduces very high dark current which gets worse when further reducing the percentage of Aluminium element. Ren M. et al. [44, 45] expanded their research into characteristics of $Al_xIn_{1-x}As_ySb_{1-y}$ (x = 0.3-0.7) avalanche photodiodes. They also demonstrated a SAM-APD configuration utilizing $Al_{0.4}In_{0.6}AsSb$ (lower Aluminium content layer for absorption) as an absorption layer and $Al_{0.7}In_{0.3}AsSb$ (higher Aluminium content layer for multiplication layer) as a multiplication layer to minimum dark current while achieved better low noise performance [46]. Their excess noise results are comparable with the excess noise performance of Si, which is very encouraging for the design of the next-generation APDs for telecommunication. Recently, Jones et al. [47] reported temperature dependence of avalanche breakdown of 6 mV/K and 15 mV/K on AlInAsSb p-i-n and SAM-APD structure, respectively. However, this material alloy has to been grown on the GaSb substrate, making it a harder and more expensive technology to develop and its small bandgap limits the dark current.

$In_{0.53}Ga_{0.47}As$ (hereafter referred to InGaAs), grown lattice-matched on InP substrates, is presently more attractive for use in SAM-APDs as the absorption material for telecommunication photodetector. InGaAs is a direct bandgap of ~ 0.75 eV at room temperature. The strong absorption coefficient up to 1.65 μm is ideal for absorbing telecommunication wavelengths. The impact ionization and excess noise of InGaAs lattice-matched on InP substrate have been reported by Ng J.S. et al. [48, 49]. InGaAs is not developed to be the avalanche region due to high tunnelling current occurring at the high-electric field. Fortunately, there are other semiconductors which can be grown lattice-matched on InP substrates.

InP was firstly used with InGaAs in SAM-APDs as the multiplication region. The impact ionization coefficients and excess noise based on InP diodes have been studied systematically. β is larger than α in InP, so pure hole injection introduces lower excess

noise performance [50-52]. The best excess noise was measured in n-i-p InP homojunction PDs with i-region ~ 0.25 μm by Li et al. [53] and Tan L.J.J. et al. further proved a low excess noise with k of 0.25 in n-i-p diodes with avalanche region of 0.25 μm [54]. For SAM-APDs excess noise have been reported with k = 0.3-0.4 with submicron multiplication region [55-57]. Further development of $In_{0.52}Al_{0.48}As$ (hereafter referred to InAlAs) has been used to replace InP as a multiplication material in InGaAs SAM-APDs. After extensive studying, it shows that α is larger than β in InAlAs, so electrons have to initiate ionization. Yuan [58] and Saleh [59] reported thin InAlAs p-i-n PDs. Goh Y.L. et al. [60] reported that the excess noise firstly increases due to the impact ionization coefficient ratios reducing, and then decreases because of the dead space effect (more details in Chapter 2) from a series of p-i-n InAlAs APDs with the avalanche region varying from 0.1 to 2.5 μm. The lowest excess noise by Goh Y.L. was corresponding to k ~ 0.25 in 2.5 μm. After substituting for the InP in an InGaAs SAM-APDs, a low excess noise was reported with k ~ 0.12-0.2 and a gain-bandwidth product of 320 GHz [61-63].

Figure 1.6 shows the performance of InGaAs-based APDs, operating at 1.3 and/or 1.55 μm compared with Si/Ge APDs. It suggests that using traditional avalanche materials, InP (k ~ 0.3-0.4) or InAlAs (k ~ 0.1-0.2), is worse compared with Si/Ge APDs due to InP or InAlAs has the broadly similar impact ionization ratio and serious tunnelling current at the very high electric fields. It also indicates that Si with a large α/β ratio can achieve both high speed and sensitivity with thicker avalanching structures. Recently, Xie S.Y. et al. [64] reported that a novel $Al_{0.85}Ga_{0.15}As_{0.56}Sb_{0.44}$ SAM-APD with a gain-bandwidth product of 424 GHz used a 100-nm–thick $Al_{0.85}Ga_{0.15}AsSb$ multiplication layer. $Al_{1-x}Ga_xAs_{0.45}Sb_{0.55}$ has a relative larger bandgap as shown in Figure 1.7 and was successfully demonstrated that it could also be grown lattice-matched on InP substrates. This relative larger bandgap could provide better dark current performance. Xie J.J. et al. reported that two p-i-n homojunction $AlAs_{0.45}Sb_{0.55}$ with nominal i-region of 100 nm and 250 nm produced very low excess under pure electron injection [65]. Zhou X.X. [66] and Pinel L.L.G. [67] found that low excess noise was observed in thin $Al_{1-x}Ga_xAs_{0.56}Sb_{0.44}$ APDs. An InGaAs/AlAsSb SAM-APDs incorporating a 40 nm AlAsSb multiplication region was reported with noise factor of k ~ 0.15 [68]; and there is no evidence of tunnelling current even above 1.07 MV/cm. These experimental results

show that $Al_{1-x}Ga_xAs_{0.45}Sb_{0.55}$ has the potential for the multiplication region in InP based telecommunication SAM-APDs.

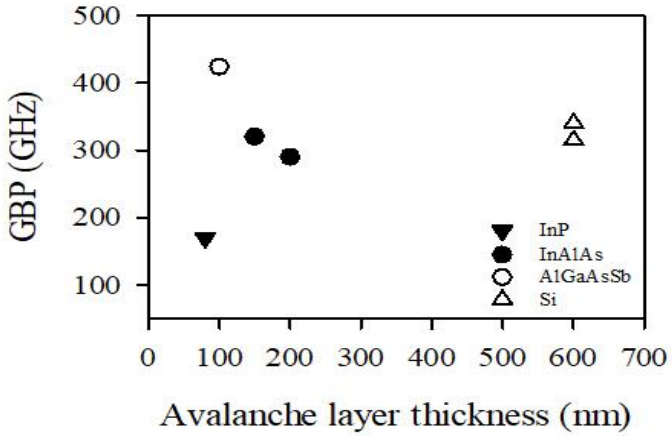

Figure 1.6. Gain-bandwidth for telecommunication APDs.

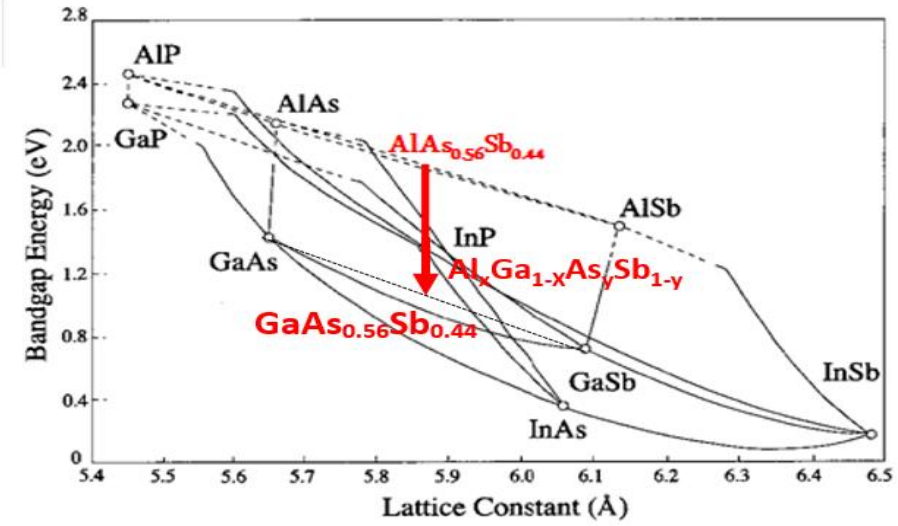

Figure 1.7. Lattice constant for $Al_{1-x}Ga_xAs_{0.45}Sb_{0.55}$ alloy.

1.5 Motivation

One of the challenges for APDs/SAM-APDs has been looking for avalanche materials of low dark current, low excess noise and large α/β ratio, which has motivated the detailed research into different III-V semiconductor materials. As discussed above, $Al_{1-x}Ga_xAs_{0.45}Sb_{0.55}$ shows low excess noise performance in the thin structure (< 250 nm); however, this low excess noise performance is possibly due to the well-known "dead-space" effect.

So far, we do not know for certain how the ionization coefficients and excess noise in bulk $Al_xGa_{1-x}As_{0.45}Sb_{0.55}$ vary with the ratio of Al/Ga. Our previous experience of undertaking ionization coefficient and excess noise measurements in $Al_xGa_{1-x}As$ on GaAs [69] and $Al_xGa_{1-x}InP$ on GaAs [70, 71] showed that the excess noise was a minimum for the largest Aluminium compositions, leading us to look at $AlAs_{0.56}Sb_{0.44}$. Therefore, this work aims to characterize and understand the impact ionization behavior of bulk $AlAs_{0.56}Sb_{0.44}$ (with a much thicker avalanche region to avoid the "dead-space" effect), which may be significant and provide useful knowledge for designing the next generation of high speed and high sensitivity InP based SAM-APDs for telecommunication applications.

1.6 The organisation of the thesis

The thesis is organized as follows:

Chapter 1 Talks about different photodetectors and competing semiconductor materials, the need for these in different applications and the structure of APDs/SAM-APDs for telecommunication application. Followed by the motivation for this work.

Chapter 2 Presents the background information of absorption of light in semiconductors and provides an overview of quantum efficiency in photodiodes. The background theory of impact ionization is reviewed. This is followed by a brief description of the mechanism of APDs and several conventional models of optoelectronic devices. Then it is a discussion of determination of impact ionization coefficients based on the measured multiplication results. The advantages and limitations of using an APD in the receivers are discussed.

Chapter 3 Describes the experimental techniques used for APD characterization which includes current-voltage (I-V), capacitance-voltage (C-V), spectral response, avalanche multiplication and avalanche excess noise.

Chapter 4 Reports of the detailed investigation of the I-V, C-V and low bias-dependent spectral response of AlAsSb didoes at room temperature. The absorption coefficients as a function of wavelength were extracted from the spectral response using a 1-D model. The band-gap energy was also estimated from the fitted absorption coefficients. The quality of new wafer grown in UCLA were examined by SEM, TEM and PL. Fabrication details of AlAsSb diode are discussed.

Chapter 5 Presents experimental multiplication results based on AlAsSb diodes at room temperature using two different wavelengths. The spectral response under high reversed bias are also shown in this chapter. They provided the support of the multiplication measurements. The local impact ionization coefficients were extracted from the measured multiplication results from seven different devices and were used to compare to other III-V materials, HgCdTe and Si. Our ionization coefficients are not only fitted for digital alloy devices, but also used for random alloy devices. The breakdown voltage of AlAsSb is shown not to follow the "universal" law introduced by Allam.

Chapter 6 Discusses the measured excess noise data of AlAsSb at room temperature using three different wavelengths and the mixed injection excess noise simulations. Extremely low excess noise were measured, corresponding to k of 0.0015 due to a large difference between electron and hole impact ionization coefficients. This is followed by modelling of gain-bandwidth products and sensitivity to reveal the effect of extremely low excess noise from InAlAs to $AlAs_{0.56}Sb_{0.44}$ in the multiplication region of a high-speed SAM-APD. This chapter aims to show for the first time making high-speed device with a thick avalanche region.

Chapter 7 Summarizes the key results of this thesis and some suggestions for further investigations.

1.7 References

[1] N. Dagli, "High Speed Photonic devices," R. G. W. Brown and E. R. Pike, Eds. Santa Barbara, USA: Taylor & Francis Group, LCC, 2007.

[2] https://www.prnewswire.com/news-releases/lidar-market-to-surpass-10-billion-by-2025-global-market-insights-inc-300839881.html

[3] G. E. Stillman and C. M. Wolfe, Avalanche photodiodes, Semiconductors and Semimetals vol. 12: New York: Academic, 1977.

[4] Y. Yu, Y. Jiang, K. Zheng, Z. Zhu, X. Lan, Y. Zhang, et al., "Ultralow-voltage and high gain photoconductor based on ZnS:Ga nanoribbons for the detection of low-intensity ultraviolet light," Journal of Materials Chemistry C, vol. 2, pp. 3583-3588, 2014.

[5] "CdS Light Dependent Photoresistors for Sensor Applications," Token Electronics Industry Co. Ltd.2010.

[6] X. Li, J. E. Carey, J. W. Sickler, M. U. Pralle, C. Palsule, and C. J. Vineis, "Silicon photodiodes with high photoconductive gain at room temperature," Optics Express, vol. 20, pp. 5518-5523, 2012.

[7] "Photomultiplier Tubes: Basics and Application Third Edition," Hamamatsu Photonics K. K.

[8] R. B. Emmons, “Avalanche photodiode frequency response,” J. Appl. Phys., vol. 38, no. 9, pp. 3705–3714, 1967.

[9] R. J. McIntyre, “Multiplication noise in avalanche photodiodes”, *IEEE Trans. Electron Devices*, vol. 13, no. 1, pp. 164–168, Jan. 1966.

[10] M. M. Hayat, B. E. A. Saleh, and M. C. Teich, “Effect of dead space on gain and noise of double-carrier-multiplication avalanche photodiodes,” IEEE Trans. Electron Devices, vol. 39, no. 3, pp. 546–552, Mar. 1992.

[11] X.W. Li,X.G. Zheng, S. L.Wang, F. Ma, and J. C. Campbell, “Calculation of gain and noise with dead space for GaAs and AlxGa1-xAs avalanche photodiode,” IEEE Trans. Electron Devices, vol. 49, no. 7, pp. 1112–1117, Jul. 2002.

[12] J. C. Campbell, S. Chandrasekhar, W. T. Tsang, G. J. Qua, and B. C. Johnson, “Multiplication noise of wide-bandwidth Inp/Ingaasp/Ingaas avalanche photodiodes,” J. Lightw. Technol., vol. 7, no. 3, pp. 473–478, Mar. 1989.

[13] P. Yuan et al., “Impact ionization characteristics of III-V semiconductors for a wide range of multiplication region thicknesses,” IEEE J. Quantum Electron., vol. 36, no. 2, pp. 198–204, Feb. 2000.

[14] M. A. Saleh et al., “Impact-ionization and noise characteristics of thin III–V avalanche photodiodes,” IEEE Trans. Electron Devices, vol. 48, no. 12, pp. 2722–2731, Dec. 2001.

[15] P. Yuan et al., “A new look at impact ionization—Part II: Gain and noise in short avalanche photodiodes,” IEEE Trans. Electron Devices, vol. 46, no. 8, pp. 1632–1639, Aug. 1999.

[16] P. Yuan, S.Wang, X. Sun, X. G. Zheng, A. L. Holmes, and J. C. Campbell,

“Avalanche photodiodeswith an impact-ionization-engineered multiplication region,” IEEE Photon. Technol. Lett., vol. 12, no. 10, pp. 1370–1372, Oct. 2000.

[17] O. H. Kwon et al., “Optimal excess noise reduction in thin heterojunction Al0.6Ga0.4 As-GaAs avalanche photodiodes,” IEEE J. Quantum Electron., vol. 39, no. 10, pp. 1287–1296, Oct. 2003.

[18] M.M. Hayat, O.H. Kwon, S.L. Wang, J.C. Campbell, B.E. A. Saleh, and M.C. Teich, “Boundary effects on multiplication noise in thin heterostructure avalanche photodiodes: Theory and experiment,” IEEE Trans. Electron Devices, vol. 49, no. 12, pp. 2114–2123, Dec. 2002.

[19] S. Wang et al., “Low-noise impact-ionization-engineered avalanche photodiodes grown on InP substrates,” IEEE Photon. Technol. Lett., vol. 14, no. 12, pp. 1722–1724, Dec. 2002.

[20] N. Duan et al., “High-speed and low-noise SACM avalanche photodiodes with an impact-ionization-engineered multiplication region,” IEEE Photon. Technol. Lett., vol. 17, no. 8, pp. 1719–1721, Aug. 2005.

[21] A. M. Pawlikowska, A. Halimi, R. A. Lamb, and G. S. Buller, \Single-photon three-dimensional imaging at up to 10 kilometers range," Opt. Exp. 25, pp. 11919{11931, May 2017.

[22] R. Tobin, A. Halimi, A. McCarthy, X. Ren, K. J. McEwan, S. McLaughlin, and G. S. Buller, “Long-range depth profiling of camouflaged targets using single-photon detection," Opt. Eng. 57(3), p. 031303, 2017.

[23] G.S. Buller, R. E. Warburton, S. Pellegrini, J. S. Ng, J. P. R. David, L. J. J. Tan, A. B. Krysa, and S. Cova, “Single-photon avalanche diode detectors for quantum key distribution," IET Optoelec. 1, pp. 249-254, December 2007.

[24] S. Cova, M. Ghioni, F. Zappa, A. Tosi, I. Rech, A. Gulinatti, and S. Tisa, “Single-photon avalanche detectors for quantum communications," in Conf. Optical Fiber Comm. (OFC/NFOEC),Nat. Fiber Optic Eng. Conf., pp. 1-3, March 2010.

[25] R.H. hadfield, “Aingle photon detectors fr optical quantum information applications,” Nat. Photon., vol. 3, pp. 696-705, Dec. 2009.

[26] R.B. Emmons and G. Lucovsky, "The frequency response of avalanching photodiodes," IEEE Trans. Electron Devices,, vol. 13, pp. 297-305, 1966.

[27] K.C. Kao and G.A. Hockla, “Dielectric-fibre surface waveguides for optical frequencies”, Proc. IEE, vol. 113, no. 7, pp. 1151-1158, July, 1966.

[28] D. Cannon, J. Liu, Y. Ishikawa, K. Wada, D. T. Danielson, S. Jongthammanurak, J. Michel, and L. C. Kimerling, “Tensile strained epitaxial Ge films on Si(100) substrates with potential application in L-band telecommunications,” Appl. Phys. Lett., 84, 906-908 (2004).

[29] G. Dehlinger and S.J. Koester and J. D. Schaub and J. O. Chu and Q.C. Ouyang and A. Grill, “High-Speed Germanium-on-SOI Lateral PIN photodiodes,” IEEE Photon. Technol. Lett. 16, 2547-2549 (2004).

[30] J. Liu, J. Michel, W. Giziewicz, D. Pan, K. Wada, D. Cannon, L.C. Kimerling, J. Chen, F. O. Ilday, F. X. Kartner and J. Yasaitis, “High-performance, tensile-strained Ge p-i-n photodetectors on a Si platform,” Appl. Phys. Lett. 87, 103501 (2005).

[31] S. Sauvage, P. Boucaud, J.M. Gerard, and V. Thierry-Mieg, “In-plane polarized

intraband absorption in InAs/GaAs self-assembled quantum dots,” Phys. Rev. B, vol. 58, pp. 10562-10567, Oct. 1998.

[32] D. Huffaker and D. Deppe, “A quantum leap in laser emission,” IEEE Circuit & Devices, vol. 15, pp. 8-13, May 1999.

[33] A.C. Farrell et al. “Plasmonic field confinement for separate absorption -multiplication in InGaAs nanopillar avalanche photodiodes,” Sci. Rep. vol. 5, pp. 17580, 2015.

[34] J.D. Beck, C-F. Wan, M.A. Kinch, J.E. Robinsonl, “MWIR HgCdTe avalanche photodiodes,” Proc. SPIE, Materials for Infrared Detectors, vol. 4454, pp. 188-197, 2001.

[35] J. Beck, C. Wan, M. Kinch, J. Robinson, P. Mitra, R. Scritchfield, F. Ma and J. Campbell, “The HgCdTe electron avalanche photodiode,” J. Electronic Materials, vol. 35, no. 6, pp. 1166-1173, 2006.

[36] X. Sun, J.B. Abshire, J.D. Beck, P. Mitra, K. Reiff and G. Yang, “HgCdTe avalanche photodiode detectors for airborne and spaceborne lidar at infrared wavelengths,” Opt. Exp., Vol. 25, No. 14, Jul. 2017.

[37] P.J. Ker, J.P.R. David and C.H. Tan, “Temperature dependence of gain and excess noise in InAs electron avalanche photodiodes,” Opt. Exp., Vol. 20, Iss. 28, Dec. 2012.

[38] P.J. Ker, A.R.J. Marshall, J.P.R. David and C.H. Tan, “Low noise high responsivity InAs electron avalanche photodiodes for infrared sensing,” Phys. Status Solidi C, No. 2, Dec. 2011.

[39] P.J. Ker, A.R.J. Marshall, A.B. Krysa, J.P.R. David and C.H. Tan, “Temperature Dependence of Leakage Current in InAs Avalanche Photodiodes,” IEEE J. Quantum Electron., Vol. 47, No. 8, Aug. 2011.

[40] A.R.J. Marshall, J.P.R. David, and C.H. Tan, “Impact Ionization in InAs Electron Avalanche Photodiode,” IEEE Trans. Electron Devices, Vol. 57, No. 10, Oct. 2010.

[41] B.S. White, I.C. Sandall, X. Zhou, A. Krysa, K. McEwan, J.P.R. David and C.H. Tan, “High-gain InAs planar avalanche photodiode,” J. Lightw. Technol., Vol. 34, No. 11, Jun. 2016.

[42] A.R.J. Marshal, P.J. Ker, A. krysa, J.P.R. David and C.H. Tan, “High speed InAs electron avalanche photodiodes overcome the conventional gain-bandwidth product limit,” Opt. Exp., Vol. 19, No. 23, pp. 23341-23349, Nov.2011

[43] M.E. Woodson, M. Ren, S.J. Maddox, Y. Chen, S. Bank and J. Campbell, “Low-noise AlInAsSb avalanche photodiode” App. Phy. Let., Vol. 108, Feb. 2016.

[44] M. Ren, Scott J. Maddox, Madison E. Woodson, Yaojia Chen, Seth R. Bank, and Joe C. Campbell, “Characteristics of AlxIn1-xAsySb1-y (x:0.3-0.7) avalanche photodiodes,” Lightwave Tech., vol. 35, no. 12, pp. 2380-2384, 15 June 2017.

[45] S.R. Bank et al., “Avalanche photodiodes based on the AlInAsSb materials system,” IEEE J. Sel. Top. Quantum Electron., vol. 24, no. 2, Mar./Apr. 2018, Art. no. 3800407.

[46] M. Ren, S.J. Maddox, Y. Chen, S.R. Bank, and J.C. Campbell, “AlInAsSb separate absorption, charge, and multiplication avalanche photodiodes,” Appl. Phys. Lett., vol. 108, no. 19, 191108, May 9, 2016.

[47] A.H. Jones, Y. Yuan, M. Ren, S.J. Maddox, S.R. Bank and J.C. Campbell, “AlInAsSb photodiode with low avalanche breakdown temperature dependence,” Opt. Exp., Vol. 25, No. 20, pp. 24340-24345, Oct. 2017.

[48] J.S. NG, C. H. Tan, J.P.R. David, G. Hill, and G.J. Rees, “Field dependence of InGaAs impact ionization coefficients,” IEEE Trans. Electron Devices, vol. 50, no. 4, pp. 901–905, Apr. 2003.

[49] J.S. Ng, C.H. Tan, J.P.R. David and G.J. Rees, “Effect of impact ionization in the InGaAs Absorber on excess noise of avalanche photodiodes” IEEE Journal of Quan. Elec., Vol. 41, No. 8, pp. 1092-1096, Aug. 2005.

[50] C.A. Armiento, and S.H. Groves, Impact ionization in (100), (110), and (111) oriented InP avalanche photodiodes Appl. Phys. Lett ., vol. 43, no. 2: pp. 198 200 1983.

[51] L.W. Cook, G.E. Bulman, and G.E. Stillman, Electron and hole impact ionization coefficients in InP determined by photomultiplication measurements Appl. Phys. Lett. Lett., vol. 40, no. 7, pp. 589-591, 1982.

[52] L.J.J. Tan, J.S. Ng, C.H. Tan, M. Hopkinson and J.P.R. David, "Effect of dead space on low field avalanche multiplication in InP", IEEE Trans. Electron Devices, vol. 54, no. 8, pp. 2051 – 2054, Aug. 2007.

[53] K.F. Li, S. A. Plimmer, J.P.R. David, R.C. Tozer, G.J. Rees, P.N. Robson, C.C . Button, J.C. Clark, Low avalanche noise characteristics in thin InP p-i-n diodes with electron initiated multiplication IEEE Photon. Tech. Lett. Lett., vol. 11, no. 3. pp. 364-366, 1999.

[54] L.J.J. Tan, J.S. Ng, C.H. Tan and J.P.R. David, "Avalanche noise characteristics in submicron InP diodes", IEEE J. of Quantum Electronics, vol. 44, no. 4, pp. 378 – 382, Apr. 2008.

[55] N. Susa, H. Nakagome, O. Mika mi, H. Ando, H. Kanbe, New InGaAs/InP avalanche photodiode structure for the 1 1.6 μm wavelength region IEEE J. Quantum Electron , vol. 16, no. 8: pp. 864-870, 1980.

[56] J.C. Campbell, S. Chandrasekhar, W.T. Tsang, G.J. Qua, B.C. Johnson, Multiplicati on noise of wide bandwidth InP/InGaAsP/InGaAs avalanche photodiodes J. Lightwave Technology , vol. 7, no. 3: pp. 473-478, 1989.

[57] S.R. Forrest, G.F. Williams, O.K. Kim, R.G. Smith, "Excess noise and receiver sensitivitymeasurements of In0.53Ga0.47As/ InP avalanche photodiodes." Electron Lett. Lett., vol. 17, no. 24: pp. 917-919, 1981.

[58] P. Yuan, C.C. Hansing, K.A. Anselm, C.V. Lenox, H. Nie, A.K. Holmes, Jr. B. G. Streetman, J.C. Campbell. "Impact Ionization Characteristics of III V Semiconductors for a Wide Range of Multiplication Region Thickness," IEEE J. Quan. Electron. vol. 36, no. 2: pp. 198-204 Feb. 2000.

[59] M. A. Saleh, M.M. Hayat, P.P. Sotirelis, A.L. Homes, J.C. Campbell, B. E. A. Saleh, M. C. Teich, "Impact ionization and noise characteristics of thin III-V avalanche photodiodes," IEEE Trans. Electron Devices , vol. 48, no. 12: pp. 2722-2731, 2001.

[60] Y.L. Goh, A.R.J. Marshall, D.J. Massey, J.S. Ng, C.H. Tan, M. Hopkinson, J.P.R. David, S.K. Jones, C.C. Button, S.M. Pinches, "Excess Avalanche Noise in $In_{0.52}Al_{0.48}As$", IEEE J. Quantum Electron . vol. 43, no. 6: pp. 503-507, 2007.

[61] D. Ning, S. Wang, X.G. Zheng, X. Li, L. Ning, J.C. Campbell, W. Chad, L.A. Coldren, "Detrimental effect of impact ionization in the absorption region on the frequency response and excess noise performance of InGaAs InAlAs SACM avalanche photodiodes IEEE J. Quantum Electron , vol. 41, no. 4: pp. 568-572, 2005.

[62] N. Li, R. Sidhu, X. Li, M. Feng, X. Zheng, S. Wang, G. Karve, S. Deminguel, A. L. Holmes, J. C.Campbell, "InGaAs/InAlAs avalanche photodiode with undepleted absorber," Appl. Phys. Lett. Lett., vol. 82, no. 13: pp. 2175-2177, 2003.

[63] G.S. Kinsey, J.C. Campbell, and A.G. Dentai, "Waveguide avalanche photodiode operating at 1.55 μm with a gain bandwidth product of 320 GHz", IEEE Photon Tech. Lett ., vol. 13, no. 8: pp. 842-844, 2001.

[64] S.Y. Xie, X.X Zhou, S.Y. Zhang, D.J. Thomson, X. Chen, G.T. Reed, J.S. NG and C.H. Tan, "InGaAs/AlGaAsSb avalanche photodiode with high gain-bandwidth product" Opt. Exp., Vol. 24, No. 21, pp. 24242-24247, 2016.

[65] J. Xie, S. Xie, R. C. Tozer and C.H.Tan. "Excess Noise Characterization of AlAsSb Avalanche Photodiodes" IEEE Trans. Electron. Devices. Vol.59, no.6. May 2012.

[66] X. Zhou, L.L. G. Pinel, S.J. Dimler, S. Zhang, J.S. Ng, and C.H. Tan, "Thin Al1-xGaxAs0.56Sb0.44 Diodes With Low Excess Noise," IEEE J. Sel. Top. Quantum Electron. 24(2), 3800105 (2018).

[67] L.L.G. Pinel, S.J. Dimler, X. Zhou, S. Abdullah, S. Zhang, C. H. Tan and J.S. Ng, "Effects of carrier injection profile on low noise thin Al0.85Ga0.15As0.56Sb0.44 avalanche photodiodes," Opt. Exp. Vol. 26, No. 3, pp. 3568-3576, Feb. 2018.

[68] C.H. Tan, S.Y Xie and J.J. Xie, "Low noise avalanche photodiodes incorporating a 40 nm AlAsSb avalanche region," IEEE J. of Quan. Elec., Vol. 48, No. 1, pp. 36-40, Jan. 2012.

[69] B. K Ng, J.P.R. David, G.J. Rees, R.C. Tozer, M. Hopkinson and R.J. Airey, "Avalanche multiplication and breakdown in AlxGa1-xAs (x<0.9)," IEEE Trans. Electr. Dev., Vol. 49, No. 12, pp. 2349-2351, Dec. 2002.

[70] J.S.L. Ong, J.S. Ng, A.B. Krysa and J.P.R. David, "Impact ionization coefficients in Al0.52In0.48P," IEEE Electr. Devi. Lett. Vol. 32, No. 11, pp. 1528-1530, Nov. 2011.

[71] R. Ghin, J.P.R. David, M. Hopkinson, M.A. Pate, G.J. Rees and P. N. Robson, "Impact ionization coefficients in GaInP p-i-n diodes," Appl. Phys. Lett., Vol. 70, No. 26, pp. 3567-3569, Jun. 1997.

CHAPTER 2:

BACKGROUND THEORY

2.1 Absorption of light in semiconductors

The properties of semiconductor materials determine the physics of semiconductor devices. The following section presents a summary of the absorption of light by a semiconductor. Free carriers can be excited to the conduction band via absorption of light with energy larger than the bandgap of the semiconductor. In a semiconductor material or semiconductor device, the cut-off wavelength refers to the longest detectable wavelength and is expressed by

$$\lambda(\mu m) = \frac{hc}{E_g} \approx \frac{1.24}{E_g} \qquad (2.1)$$

Where λ is the photon's wavelength, h is Planck's constant (~4.13×10^{-15} eV s), c is the speed of light (~3×10^{8} m/s), and E_g (eV) is the bandgap of the semiconductor.

The absorption coefficient of a semiconductor material, γ, describes the rate of decrease in the intensity of light as it passes through it. A high value of absorption coefficient indicates that the light will be absorbed near the surface of the material and a low value of absorption coefficient indicates the light will penetrate deeper. Photoexcitation does not happen if the wavelength is too long. The intensity of light, φ, when travelling through one of the semiconductors can be express as

$$\varphi = \varphi_0 \exp(-\gamma x) \qquad (2.2)$$

Where φ_0 is the initial intensity of light and x is the travelling distance. It is worth introducing that there is a short wavelength cut-off due to the carrier recombination. More details will be presented later.

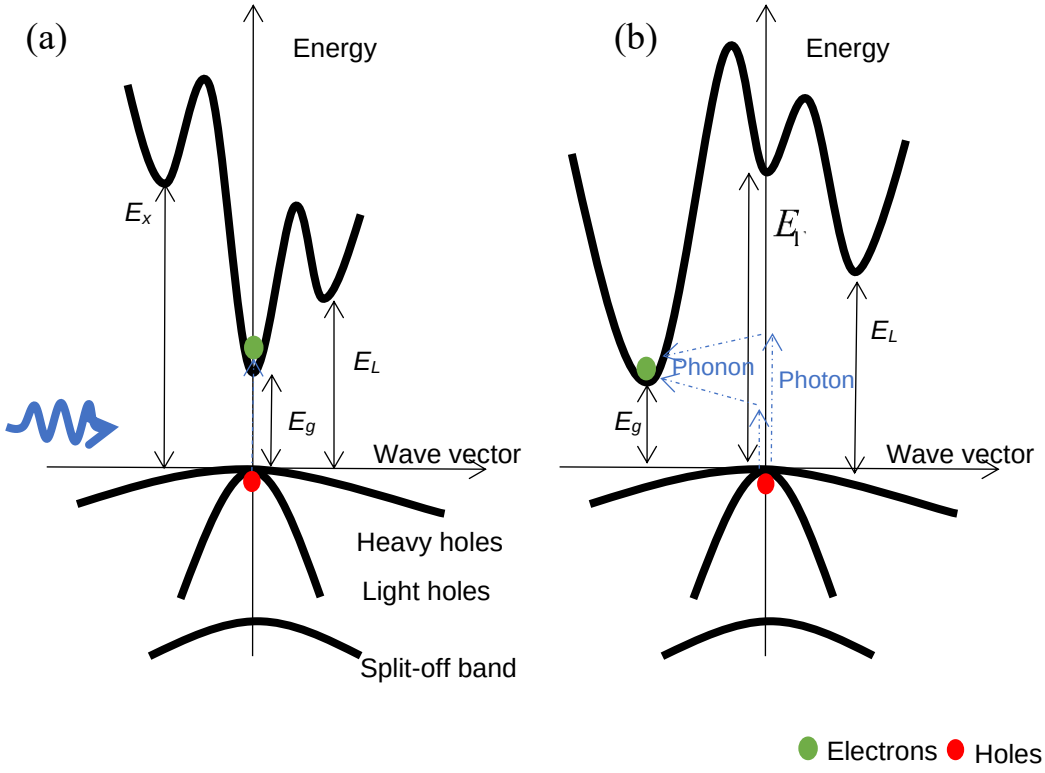

Figure 2.1. Examples of (a) the direct bandgap of GaAs, and (b) indirect bandgap of Si absorbed a photon with high energy.

The requirements for the transition of carriers (electrons, holes) between the valance band and the conduction band are energy has to be conserved and momentum has to be conserved. Typically, the conservation of energy is evident in direct and indirect bandgap semiconductors if the photon energy is larger than the energy between the maximum of the valance band and the minimum of the conduction band. This minimum energy gap is generally named bandgap of the semiconductor, E_g. It is a critical parameter for different semiconductors and is related to the cut-off wavelength, as shown in Equation 2.1. In a direct bandgap semiconductor, the momentum remains the same before and after transitions. However, the conservation of momentum has to be achieved by phonons in an indirect semiconductor. Let us consider a direct bandgap case, GaAs, shown in Figure 2.1(a), where the minimum of the conduction band is aligned with the maximum of the valance band at Γ -point of the Brillouin zone. The carriers start to be generated if the photon energy hf is larger than E_g. No phonon is required for the conservation of the momentum. Figure 2.1(b) shows the case of photon absorption in Si. Si with an indirect bandgap needs to interact with a phonon for the absorption of a photon, provided hf is larger than the bandgap. More details of the band structure will

be discussed in the following section. The probability of an absorption process in indirect materials are much lower than direct materials.

The absorption coefficients in direct bandgap materials and indirect bandgap materials can be express as respectively [1]

$$\begin{aligned} \gamma &\propto \left(hf - E_g\right)^{\frac{1}{2}} \quad , hf \geq E_g \\ \gamma &= 0 \qquad\qquad , hf < E_g \end{aligned} \tag{2.3}$$

$$\begin{aligned} \gamma &\propto \left(hf - E_g \mp \hbar\Omega\right)^2 \quad , hf \geq E_g \\ \gamma &= 0 \qquad\qquad , hf < E_g \end{aligned} \tag{2.4}$$

Where $\mp h\Omega$ is the phonon absorption and emission. The direct and indirect bandgap is determined by the horizontal intercepts of the γ^2 versus E plot and $\gamma^{0.5}$ versus E, respectively. In recent years, the absorption coefficients were widely investigated, as shown in Figure 2.2. The direct bandgap materials have an abrupt cut-off. Otherwise, indirect material shows smooth. Absorption coefficients of InGaAs and Ge show strong absorption between 1.3 and 1.6 μm.

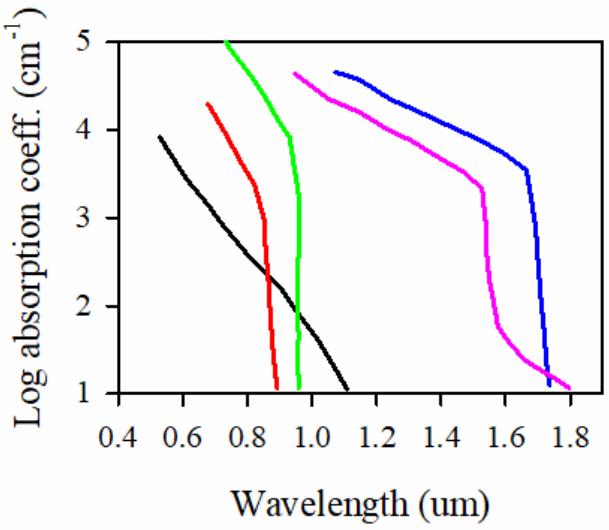

Figure 2.2. Measured optical absorption coefficients for Si (black) [2], GaAs (red), InP (green) [4, 5], Ge (pink) [4, 6] and InGaAs (blue) [7].

2.2 Quantum efficiency in photodiodes

It is very difficult to achieve unity quantum efficiency (η) in real semiconductors due to surface recombination, the minority carrier recombination and reflectivity at the surface of devices. Recombination is the inverse of direct optical absorption. Band-to-band, trap-assisted and auger recombination are three individual processes by which electrons and holes annihilate each other. The surface recombination is more conspicuous at shorter wavelengths with strong absorption coefficients and as a result, photodiodes also have short cut-off wavelengths when photo-response is very low. The reason is because of the deep trap recombination caused by dangling bonds [8], deformation of crystal lattice arrangement periodicity [9] and multiple phonon emissions [10]. The generated carriers have to diffuse and will not contribution to the photocurrent if they recombine before entering into the high electric field. Physically, diffusion is due to the random thermal motion of carriers as well as scattering. The diffusion length mainly depends on the crystal quality (associated with trap-assisted recombination) [11], doping concentration [12], temperature [12] and band structure (whether the semiconductor is a direct or indirect material) [13].

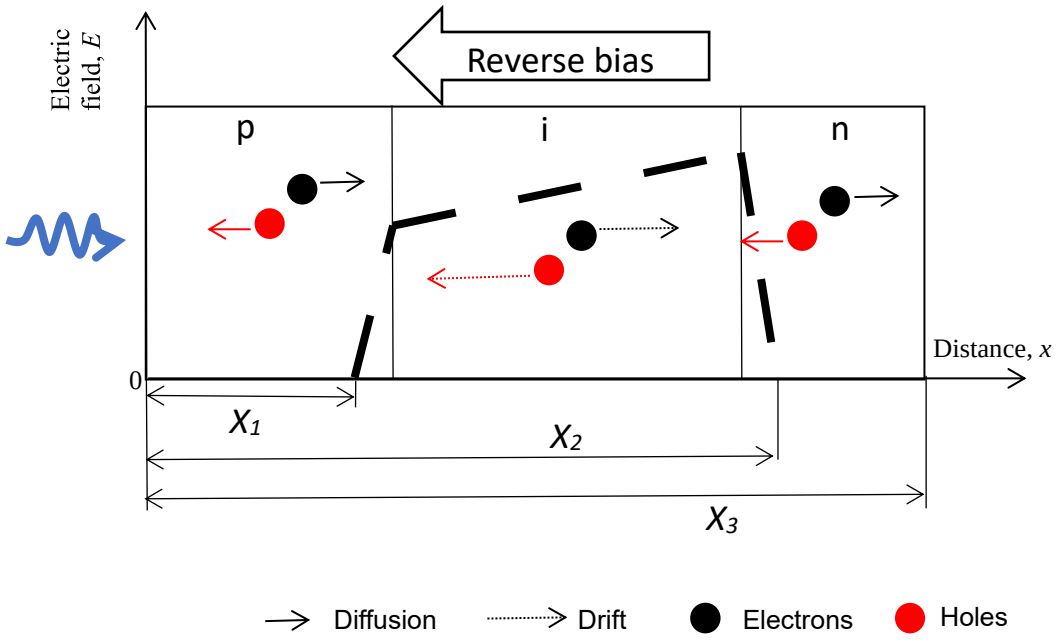

Figure 2.3. Electric field profile of a p-i-n structure.

The measured external quantum efficiency, η, of the photodiode is calculated using the equation

$$\eta = 1240 \times \frac{R}{\lambda(nm)} \qquad (2.5)$$

Where R is the measured responsivity. The external quantum efficiency results can be fitted by a 1-D quantum efficiency model based on current-continuity equation [14]. For a p-i-n structure, as shown in Figure 2.3, the total photocurrent measured externally consists of electrons collected from the p layer, electron-hole pairs generated in the i layer and holes collected from the n layer. The electron-hole pairs generated in the i layer are assumed to be collected with 100% efficiency due to the electric field. However, the current contributed by the carriers diffusing from the cladding layer strongly depends on their diffusion length.

The quantum efficiency component, η_1, due to electrons collected from the p layer is:

$$\eta_1 = \left(\frac{\gamma L_e}{\gamma^2 L_e^{\,2} - 1} \right) \left[\frac{\frac{S_e L_e}{D_e} + \gamma L_e - \exp(-\gamma X_1)\left(\frac{S_e L_e}{D_e}\cosh\frac{X_1}{L_e} + \sinh\frac{X_1}{L_e}\right)}{\frac{S_e L_e}{D_e}\sinh\frac{X_1}{L_e} + \cosh\frac{X_1}{L_e}} - \gamma L_e \exp(-\gamma X_1) \right] \qquad (2.6)$$

Similarly, the quantum efficiency component, η_2 due to holes collected from the n layer is

$$\eta_3 = \left(\frac{\gamma L_h}{\gamma^2 L_h^{\,2} - 1} \right) \exp\left[-\gamma(X_3 - X_2)\right] \left[\gamma L_h - \frac{\frac{S_h L_h}{D_h}\left[\cosh\frac{X_3}{L_h} - \exp(-\gamma X_3)\right] + \sinh\frac{X_3}{L_h} + \gamma L_h \exp(-\gamma X_3)}{\frac{S_h L_h}{D_h}\sinh\frac{X_3}{L_h} + \cosh\frac{X_3}{L_h}} \right] \qquad (2.7)$$

Then the quantum efficiency component due to electron-hole pairs generated in the i layer is

$$\eta_2 = \exp(-\gamma X_1)\left\{1 - \exp\left[-\gamma(X_2 - X_1)\right]\right\} \qquad (2.8)$$

Where L_e (L_h) is the minority electron (hole) diffusion length, D_e (D_h) is the electron (hole) diffusion constant which can be related to L_e (L_h) by

$$L_e(L_h) = \sqrt{D_e \tau_e}\,(\sqrt{D_h \tau_h})$$

where D_e (D_h) is the minority electron (hole) lifetime, S_e (S_h) is the surface recombination velocity in the p (n) layer surface, X_1, X_2 and X_3 are the distances from the surface of device to the top of depletion, to the bottom of depletion edge, and to the bottom of device, respectively. The total internal quantum efficiency, η_{int}, is the sum of equations (2.6), (2.7), and (2.8).

$$\eta_{\text{int}} = \eta_1 + \eta_2 + \eta_3 \qquad (2.9)$$

Therefore, the external quantum efficiency, η, of the photodiode is

$$\eta = (1-R)\eta_{\text{int}} \qquad (2.10)$$

Where R is the reflectivity at the top surface. More details can be found in [14].

2.3 Impact ionization in semiconductors

Impact ionization is a scattering process involving the generation of new electron-hole pairs, mainly observed at high electric fields in a semiconductor. Multiplication/Gain (M) in an APD originates from this phenomenon. The energy of free carriers travelling at high electric fields in a semiconductor is determined by the sum of the kinetic energy obtained from the high electric field and the loss through phonon scattering. In this process, some of the aforementioned carriers which exceed the minimum energy required for impact ionization can promote an electron from its bound state in the valence band into the conduction band, leaving behind a free hole in the valence band. The energy of the primary carrier always reduces after ionizing. Both the primary carrier and the newly-formed electron-hole pair continue to travel under the high electric field and then cause further ionization events, randomly. Figure 2.4 schematically illustrates the electron initiated (left) and hole initiated (right) impact ionization process on the E-K diagrams.

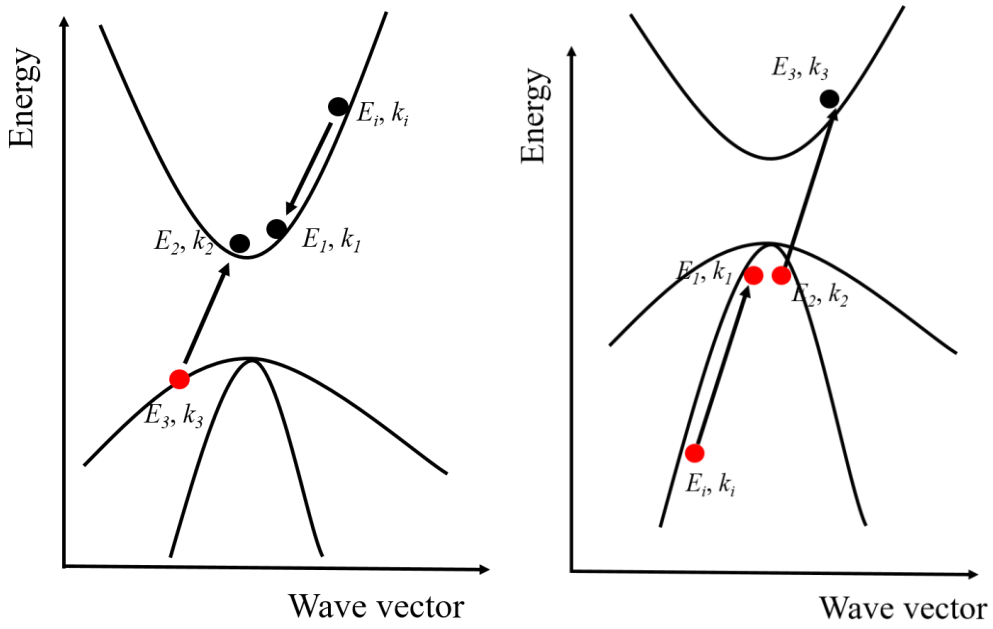

Figure 2.4. Schematic diagram illustrating electron (left) and hole initiated impact ionization process on E-K plot (right). Black circles present the electron, and red circles present the hole. E_i is the initial state of a carrier. E_1, E_2 and E_3 are the final states.

Free carriers can only initiate impact ionization when they reach the minimum energy required for impact ionization. This is commonly referred to as the threshold energy, E_{th}, which generally depends on the band structure of the semiconductor materials. Thus different band structures will involve correspondingly different E_{th}. E_{th} must be larger than the E_g of the semiconductors due to the conservation of energy and momentum. Wolff et al. [15] showed that E_{th} is equal to $1.5E_g$ by assuming simple parabolic band structures with equal electron and hole mass. Anderson and Crowell [16] estimated E_{th} for electrons, as shown in Equation (2.11)

$$E_{th} = E_g\left(1+\frac{m_e}{m_e+m_h}\right) \qquad (2.11)$$

Where m_e and m_h are the electron and hole masses of the parabolic, spherical band. However, in reality, the electron and hole mass are different and energy bands are complex. Figure 2.5 shows the calculated band structures of GaAs and Si [17]. The maxima of the valence band in GaAs and Si are both located in the zone centre. The conduction band in GaAs and Si has its minima in the Γ–valley and X-valley respectively. Thus, for GaAs, the lowest energy gap (E_g) lies at the zone centre (Γ–valley) and it is referred to as a direct bandgap material. While Si is defined as an indirect bandgap material.

Most III-V semiconductors crystallise into the zinc-blende structure where the conduction band has one Γ–valley, three X-valleys and four L-valleys. The valence band of semiconductor at the zone centre is even more complicated, consisting of a band with a large dispersion called the light hole band and a band with a small dispersion called the heavy hole band. There is one more band separated by spin-orbit splitting from the heavy hole, and light hole bands called the split-off band. The constant effective mass commonly used to characterise the various bands assume that it is parabolic near the zone centre. Figure 2.1 and Figure 2.5 both present band structures. Furthermore, several studies [18, 19] show that most of the carriers undergo ionization in higher energy bands which have a strongly non-parabolic relation between energy and wavevector due to the periodic potential of the lattice. Consequently, the value of E_{th} is frequently treated as an adjustable parameter to obtain agreement with experimental results [20, 21].

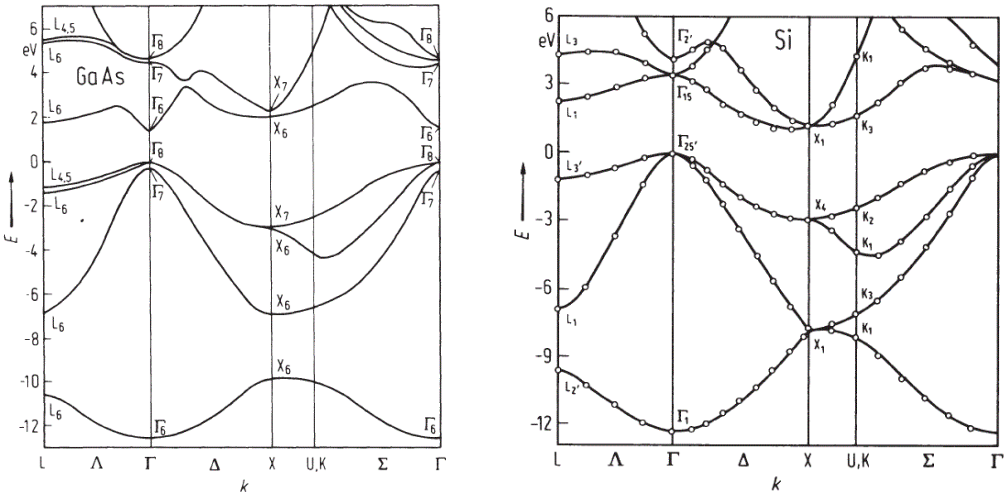

Figure 2.5. Band structure of GaAs (left) and Si (right) [17].

Phonons carry both energy and momentum and can scatter carriers from one state to another state within the band structure. Phonon scattering event is one of several non-ionization collision processes during which carriers can gain energy (absorption process, where the carrier gains energy equal to *hf*, lose energy (emission process, where the carrier loses energy equal to *hf* or exchanging momentum (elastic, where the carrier is involved only in a momentum exchange). In general, carriers will lose energy by phonon scattering as the phonon emission rate is proportional to N_{ph}+1, and phonon

absorption rate is proportional to N_{ph} [22]. Therefore, average carriers have to lose energy to phonons, which impedes their progress to become "hot" carriers where impact ionization occurs. The phonon occupation number, N_{ph}, is given as

$$N_{ph} = \frac{1}{\exp(\frac{hf}{k_B T} - 1)} \qquad (2.12)$$

Where k_B is Boltzmann's constant, hf is the photon energy and T is the absolute temperature. A reduction in temperature will increase the ionization probability of carriers as fewer phonons are involved. For most III-V avalanching materials, ionization coefficients increase as temperature reduces, such as in AlInP [23]. However, InAs is a particular case in which ionization coefficients reduce while temperature reduces [24]. The reason here is that InAs has a narrow bandgap and the relative bandgap change is bigger than the relative phonon scattering change.

Phonon scattering rates as an expression of the material parameters are derived from Fermi's Golden Rule of first-order time-dependent perturbation rule, which gives the probability per unit time that the transition may occur. Under the assumption that the scattering event is instantaneous, the transition rate $W(k_i, k_f)$ is expressed as

$$W(k_i, k_f) = \frac{2\pi}{\hbar} \left| \left\langle k_f \left| U_{pot} \right| k_i \right\rangle \right|^2 \delta(E_i - E_f) \qquad (2.13)$$

Where U_{pot} is a perturbing potential due to the movement of the lattice from the ideal place and $<k_f|U_{pot}|k_i>$ is the matrix element. The scattering rate then can be calculated by

$$\frac{1}{\tau(E)} = \sum_{k_f} W(k_i, k_f) \qquad (2.14)$$

Full details of the derivation can be found elsewhere [25].

For semiconductors with bandgap above 0.5 eV such as GaAs (E_g ~ 1.42 eV), carriers gain energy in the central valley (Γ−valley) so that they can scatter into the satellite valleys or into higher conduction bands where the density of states is larger. The phonons interacting in these transitions are mostly through longitudinal optical and longitudinal acoustic phonons with large momentum. However, the intervalley scattering process causes momentum randomisation of the particles due to the large momentum of the cooperating phonon.

Impact ionization coefficients in the Local Model, i.e. α for electron and β for hole, is the average numbers of ionization events experienced by a free carrier travelling in a unit distance in the direction of the electric field. The reciprocal of α (β) shows the mean distance a carrier travels before it initiates impact ionization. These coefficients describe the rate of creation of electron-hole pairs. The local magnitudes of α and β assume that the probability for a carrier to impact ionize depends only on the value of the local electric field. In general, coefficients depend on the band structure. The ratio of these two coefficients in one material is the impact ionization ratio, or k-factor (defined $k = \alpha/\beta$ in this chapter).

2.4 Avalanche multiplication and breakdown

The injected "cold" carriers can trigger a finite number of successive impact ionization events in the high field region, resulting in an increment in the number of free carriers to produce a current multiplication factor (M). This injected 'cold' carriers are called primary carriers and this chain of impact ionization events is called avalanche multiplication. In general, the features of the multiplication process can be seen by considering the high-field depletion region of an APD used in a specified avalanching semiconductor material. Figure 2.6(a) shows the electron transport schematically in a semiconductor which leads to three impact ionization events. The 'cold' carrier is accelerating by the high electric field and is only slowly gaining energy due to the energy loss by phonon scattering. At a particular time, impact ionization occurs. Figure 2.6(b) and (c) shows the multiplication process schematically for $M = 5$, in different materials ($k = 1$ and $k = 0$, respectively) due to an electron being injected into the high-field depletion region of an APD with length w. One electron is injected at the left boundary of the electric field ($x = 0$), and the direction of the field is assumed as shown in the figure. The electron, travelling from the left to the right and leaving the avalanche multiplication region at $x = w$, can generate a new electron-hole pair via impact ionization after travelling a random ionization path length, l. While the holes, drifting from right to left and leaving at position $x = 0$, can also generate a new electron-hole pair. The impact ionization events of the newly generated carriers and the primary carriers behave in a statistically identical manner by undergoing further ionization. The inherently random

nature of impact ionization guarantees fluctuation in the multiplication of multiple carriers, and we use M_{ind} for the random variable of avalanche gain ($M = \langle M_{ind} \rangle$). This randomness is attributed by the randomness in position at which the secondary carriers are produced, and the randomness in the number of secondary carriers produced. This multiplication process will end when all carriers exit the avalanche region. Figure 2.6 (d) shows the case of carriers generated within the avalanche region. Figure 2.7 shows a typical multiplication characteristic as a function of reverse bias. The black line shows the $\langle M_{ind} \rangle$ and the red line presents M_{ind}. The more fluctuation, the worse excess noise of an APD.

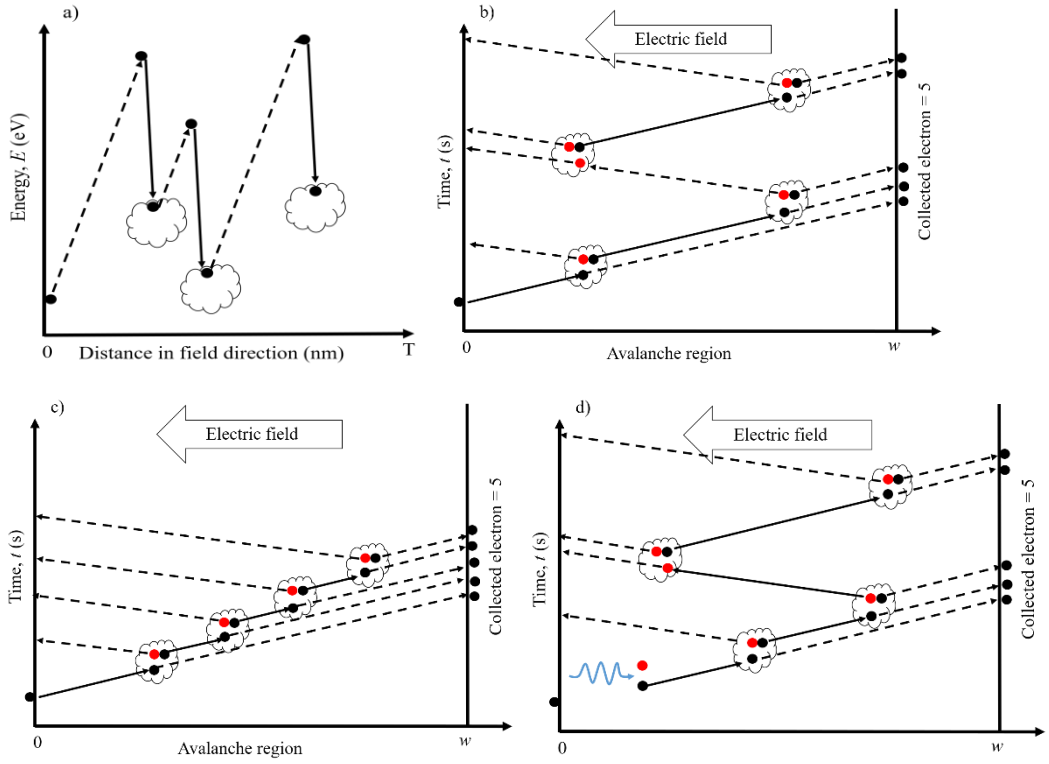

Figure 2.6. a) One electron transport in a semiconductor leading to impact ionization events. b) Schematic diagram illustrating the electron initiated avalanche multiplication process with $\alpha = \beta$ after diffusing into the high field region. c) Schematic diagram illustrating the electron initiated avalanche multiplication process with $\beta = 0$ after diffusing into the high field region. d) A photogenerated electron-hole pair within the high electric field with $\alpha = \beta$. Red circles are holes, and black circles are electrons.

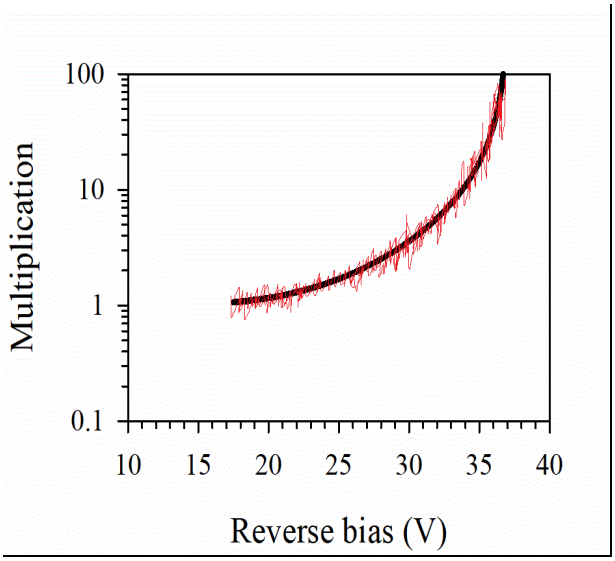

Figure 2.7. A typical avalanche multiplication characteristic as a function of reverse bias. Black line presents mean multiplication and red line shows noise on multiplication.

Stillman and Wolfe [27] determined an analytical expression for the mean multiplication factor by considering the current continuity equation for primary carriers generated within w, assuming the carrier's ionization probability only depends on the local electric field. The mean multiplication factor at x, $M(x)$, is expressed by

$$M(x) = \frac{\exp\left[-\int_{x}^{w} \alpha(x') - \beta(x')dx'\right]}{1 - \int_{0}^{w} \alpha(x') \exp\left[-\int_{x'}^{w} \alpha(x'') - \beta(x'')dx''\right]dx'} \qquad (2.15)$$

The multiplication factor for pure electron injection, M_e, where an electron is injected at $x = 0$, can be expressed as

$$M_e = M(0) = \frac{1}{1 - \int_{0}^{w} \alpha(x') \exp\left[-\int_{0}^{x} \alpha(x'') - \beta(x'')dx''\right]dx'} \qquad (2.16)$$

The multiplication factor for pure hole injection, M_h, where a hole is injected at $x = w$, can be similarly expressed as

$$M_h = M(w) = \frac{1}{1 - \int_{0}^{w} \beta(x') \exp\left[-\int_{x}^{w} \alpha(x'') - \beta(x'')dx''\right]dx'} \qquad (2.17)$$

Assuming the high field is uniform, for the case of ideal p+-i-n+/n+-i-p+ structures, Equation (2.16) and (2.17) can be further reduced to

$$M_e = \frac{1}{1-\frac{\alpha}{\alpha-\beta}\{\exp[(\beta-\alpha)w]-1\}} \quad , \quad M_h = \frac{1}{1-\frac{\beta}{\alpha-\beta}\{\exp[(\alpha-\beta)w]-1\}} \qquad (2.18)$$

To demonstrate the effects of the ionization coefficients on the avalanche multiplication mechanism in a uniform field, let us consider two special cases, $k = 1$ and $k = 0$. The build-up of the avalanche process with time is shown schematically in Figure 2.6 (b) and (c), respectively. For $\alpha = \beta$ ($k = 1$), Equation (2.18) can be simplified further to give

$$M_e = M_h = \frac{1}{1-\alpha w} \qquad (2.19)$$

As the electron travels in a high-field, it generates an electron-hole pair after a random ionization path. The hole from this pair can also generate a new electron-hole pair after acquiring enough energy and so on. Figure 2.6(b) show that there are relatively few carriers in the i-region at any given time even at high gain. For this case, the multiplication process with high carrier feed-back has both larger build-up time and more fluctuation in current, seen as a definite gain-bandwidth and a high excess noise. Thus, this is a worse case for the performance of APDs. Germanium is an example of such material.

On the other hand, the extreme case is $k = 0$ as s avalanche process shown in Figure 2.6(c). For $\beta = 0$ ($k = 0$), Equation (2.18) reduces to

$$M_e = \exp(\alpha w) \qquad (2.20)$$

The multiplication continues to increase exponentially with increasing values of αw. Under this condition, there are only electrons undergoing ionization, therefore, there is less fluctuation and a shorter build-up time. An example of such a material is HgCdTe.

The definition of avalanche breakdown is the voltage when the multiplication becomes infinite. In general, the breakdown condition can be expressed by equating the denominators of Equation (2.18) to zero. Thus, the avalanche breakdown voltage, V_{bd}, depends on the ionization coefficients, electric field is not affected by the carrier injection conditions. For the special cases, the breakdown condition is given by $\alpha w = 1$ for $k = 1$ and no avalanche breakdown occurs for $k = 0$ due to no carrier feedback.

The position independence α and β can be expressed in terms of M_e and M_h by rearranging Equation (2.18) as shown in Equation (2.21), which shows the simplest way to extract the impact ionization coefficients of a semiconductor. The value of M_e and M_h can be measured for p-i-n/n-i-p structures. Ideally, M_e and M_h should be measured on the same APDs to ensure identical electric field profile and scattering environment, however, this cannot be done easily without destroying the devices. Therefore, researchers try to grow similar i-region thickness and doping density with p-i-n and n-i-p configuration. It is worth noting that these equations assume that the high electric field in the i-region is a constant value. For a more accurate analysis, the doping levels in the cladding layers and i-region and the thickness of i-region are required to simulate the real electric field profile.

$$\alpha = \frac{1}{w}\left(\frac{M_e - 1}{M_e - M_h}\right)\ln\left(\frac{M_e}{M_h}\right), \quad \beta = \frac{1}{w}\left(\frac{M_h - 1}{M_e - M_h}\right)\ln\left(\frac{M_e}{M_h}\right) \qquad (2.21)$$

2.5 Avalanche excess noise

In an APD, the electrons and holes, promoted by the photoelectric effect, are swept away to be collected at the contacts if the electric field is applied. Assuming the incident photons are Poisson distributed, the means square shot noise current is given by

$$< i_s >= 2qIB \qquad (2.22)$$

Where B is the measurement bandwidth, and I is the current flowing through the APD. If an APD is considered ideal with multiplication, M. Then the means square noise current is given by

$$< i >= 2qI_{pr}FM^2B \qquad (2.23)$$

Where I_{pr} is the primary current and F is defined as

$$F = \frac{< M^2_{ind} >}{< M_{ind} >^2} \qquad (2.24)$$

In early work, it was shown that there is a positive feedback characteristic between α and β which can significantly increase any initial current fluctuations. And also predicted that the mean square fluctuation when $\alpha = \beta$ would be M times bigger than that of an ideal case where $\beta=0$, and this is given by

(2.25)

$$< i >= 2qI_{pr}M^3B$$

McIntyre [26] extended this analysis to the case of unequal ionization coefficients in an avalanche region with length w showed that F can be expressed as a function of the ratio of the ionization coefficients and the multiplication factor assuming the ionization probability only depends on the local electric field. The excess noise factor for pure electron initiated multiplication is expressed as

$$F_e = kM + (2 - \frac{1}{M})(1 - k) \qquad (2.26)$$

Where $k = \beta/\alpha$. similarly, the expression for hole initiated multiplication can be express as

$$F_h = kM + (2 - \frac{1}{M})(1 - k) \qquad (2.27)$$

Where $k = \alpha/\beta$. Figure 2.8 (a) shows F as a function of M for various values of k assuming pure electron initiated multiplication and $\alpha > \beta$. It indicates that the low excess noise can be achieved if $k = \beta/\alpha = 0$ in this case.

In recent years, the impact ionization coefficients and the excess noise performance were widely investigated in different semiconductors, as shown in Figure 2.8 (b) and (c). In general, the ratio of ionization coefficients, k, is similar ($k \approx 1$) at high electric fields and there is a small difference at the low electric fields (assuming $\alpha > \beta$). Si is an unusual case and has a better ratio even at the high electric field, and is widely used to design low excess noise APDs. Unluckily, the cut-off wavelength is not suitable for telecommunication applicants due to its large bandgap.

McIntyre's original theory pointed out that the excess noise factor is at a minimum for materials with a very different electron and hole impact ionization coefficients with the carrier having the larger ionization coefficient initiating the chain of impact ionizations. In reality, however, photons could be absorbed inside the multiplication region, as shown in Figure 2.6 (d). The generated parent electron and hole would independently and individually initiate the avalanche multiplication process, which is called mixed-carrier injection. More details about multiplication and excess noise performance for mixed-carrier injection will be discussed in Chapter 6.

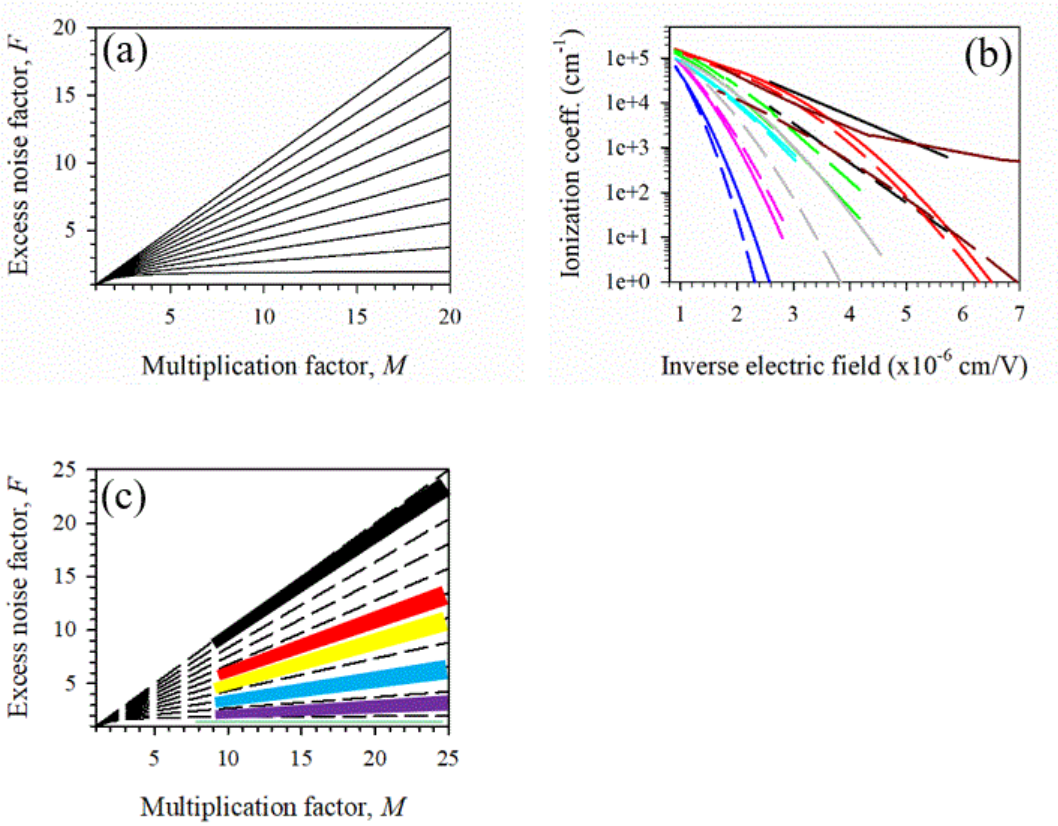

Figure 2.8. (a) McIntyre's local model excess noise predictions for $k = 0$ to 1 in the step of 0.1 for an electron injection when $\alpha > \beta$. (b) Measured ionization coefficients in several semiconductors as a function of the inverse electric field. Si (black), GaAs(red), InP (green), AlInP (blue), GaInP (pink), $Al_{0.6}Ga_{0.4}As$ (cyan), InAlAs (gray), and InGaAs (dark red) [28-35]. Solid lines are electron ionization coefficients, and dash lines are hole ionization coefficients. (c) Excess noise versus multiplication for different materials. Ge (black), GaAs (red), InP (yellow), AlInAs (blue), Si (purple) and InAs (green) [36-41]. Dashed lines are McIntyre's local model for $k = 0$ to 1 in the step of 0.1.

The McIntyre's local noise theory provided the direction for designing low excess noise APDs. Using a material with significant asymmetry between α and β reduces excess noise. However, the response time would be increased due to the large α/β ratio generally only occurring at the low electrical field in a thick multiplication region. In order to satisfy the high-speed requirement, researchers used a thin multiplication layer and applied a higher electric field to achieve the same gain as that of an APD with a thick multiplication region. Based on McIntyre's local noise theory, larger excess noise characteristics would be measured because of a low α/β value at the high electric field (assuming $\alpha>\beta$) but the opposite case was observed. The APDs with thinner multiplication

layers generally performed better with lower excess noise, as demonstrated by the recent measurements on III-V semiconductors [42-46]. Thus the McIntyre's local model is no longer valid as the avalanche width decreases.

Models used for an APD with the thin avalanching region can use Monte Carlo and non-local techniques. Both models take into account the "dead-space" effects. "Dead-space" is defined as the minimum distance that a carrier must travel in order to gain sufficient energy from the electric field to initiate an impact ionization event. When the multiplication region reduces, the dead space becomes a more signification fraction of the total distance travelled by the carriers before ionization. For a uniform electric field, d_e and d_h can be given by

$$d_e = \frac{E_{the}}{q\xi} \quad \text{and} \quad d_h = \frac{E_{thh}}{q\xi} \qquad (2.28)$$

Where q is the electronic charge, ξ is the electric field, E_{the} and E_{thh} is the threshold energy of the electron and hole. E_{th} is a significant factor which influences the probability of ionization.

Monte Carlo (MC) models, in general, provide the most realistic approach to simulating high field carrier scattering but require long computation time. For the non-local model, Hayat *et al.* [47] developed the recursive technique based on the probability distribution function (PDF) of the ionization path length of a carrier in the electric field which is capable of simulating the multiplication and excess noise down to avalanche widths of 0.1 μm [48]. Ong et al. [37] introduced the random path length model (RPL), which depends on randomly chosen ionization path lengths to calculate the probability of carrier ionization. The displaced ionization path length PDFs are utilised within a MC framework to predict the multiplication and excess noise in APDs. Both techniques can predict similar gain and noise results. It is well-known that the Local Model suggests accurate results when $d_e\alpha$ and $d_h\beta \leq 0.3$. Details of RPL model which was used in this work is discussed below.

2.6 Random path length model

Consider an electron injected into the avalanche width, w with a constant electric field at x_0. The ionization behaviour of carriers is also characterised by the ionization path

length PDFs, *P(x)*, which present the probability of the carrier ionizing for the first time after drifting a distance of *x* from the injecting position of x_0 and is given by [49]

$$P_e(x) = \begin{pmatrix} 0 & , x - x_0 < d_e \\ \alpha^* \exp\left[-\alpha^*(x - x_0 - d_e)\right] & , x - x_0 \geq d_e \end{pmatrix} \qquad (2.29)$$

Where electrons are assumed to travel in the *x*-direction, α^* is defined as the electron ionization coefficient which is the ionization coefficient after the electron travels its "dead-space", d_e as related to the electric field shown in Equation 2.29. Then the average probability of ionizing within *x* is given by integrating the PDF from $x_0 + d_e$ to *x* to give,

$$G_e(x_0 < x' < x) = \begin{pmatrix} 0 & , x - x_0 < d_e \\ 1 - \exp[-\alpha^*(x - d_e)] & , x - x_0 \geq d_e \end{pmatrix} \qquad (2.30)$$

Following Equation (2.30), the probability of electrons not ionizing, S_e, is given by,

$$S_e(x_0 < x' < x) = \begin{pmatrix} 1 & , x - x_0 < d_e \\ \exp[-\alpha^*(x - d_e)] & , x - x_0 \geq d_e \end{pmatrix} \qquad (2.31)$$

Rearranging Equation (2.31) if we substitute S_e with a uniformly distributed random number (a value from 0 to 1) gives,

$$x = d_e - \frac{\ln(r)}{\alpha^*} \qquad (2.32)$$

Where *r* is a uniformly distributed random number, and *x* is the distance an electron travels before it ionizes for the first time. Similar derivation procedures can be obtained for holes. A pseudo-random-number generator is used to generate a random number, *r*, to determine the ionizing length of carriers, and these random numbers are independent of each other. In each trial, the process keeps a record of the position of impact ionization of all carriers until no carriers stay in the avalanche region. To achieve reliable simulation results, simulation using the RPL model needs to repeat many trials, *N*. Then the mean multiplication, *M*, and excess noise, *F*, of carriers injected at a position of x_0 is given by,

$$M(x_0) = \frac{1}{N}\sum_{N=1}^{N} M_N \qquad (2.33\ a)$$

and

$$F(x_0) = \frac{1}{NM^2(x_0)}\sum_{N=1}^{N} M_N^2 \qquad (2.33\ b)$$

2.7 Advantage of APD/SAM-APD in an optical receiver

APDs/SAM-APDs are widely used in many diverse applications requiring high speed, high bandwidth and high sensitivity. The fundamental advantage of APDs is their internal gain. In the optical receiver, the signal-to-noise ratio (SNR) for an APD incorporated with a preamplifier can be expressed as [50]

$$SNR = \frac{P_s}{FN_{sn} + N_{preamp} / M^2} \qquad (2.34)$$

Where P_s is the electrical signal power at unity gain, M and F are the multiplication and excess noise factors relative with the multiplication material N_{sn} is the unity gain shot noise power of the APD and N_{preamp} is the noise power of the preamplifier. Figure 2.9 shows the case of $P_s > N_{preamp}$ and $P_s < N_{preamp}$ for $N_{preamp} >> N_{sn}$, respectively. For both cases, the SNR of a receiver is a significant enhancement by operating the APD with gain. However, this is limited by excess noise. A lower APD noise can let us operate APD at a higher gain, making the SNR of a receiver better.

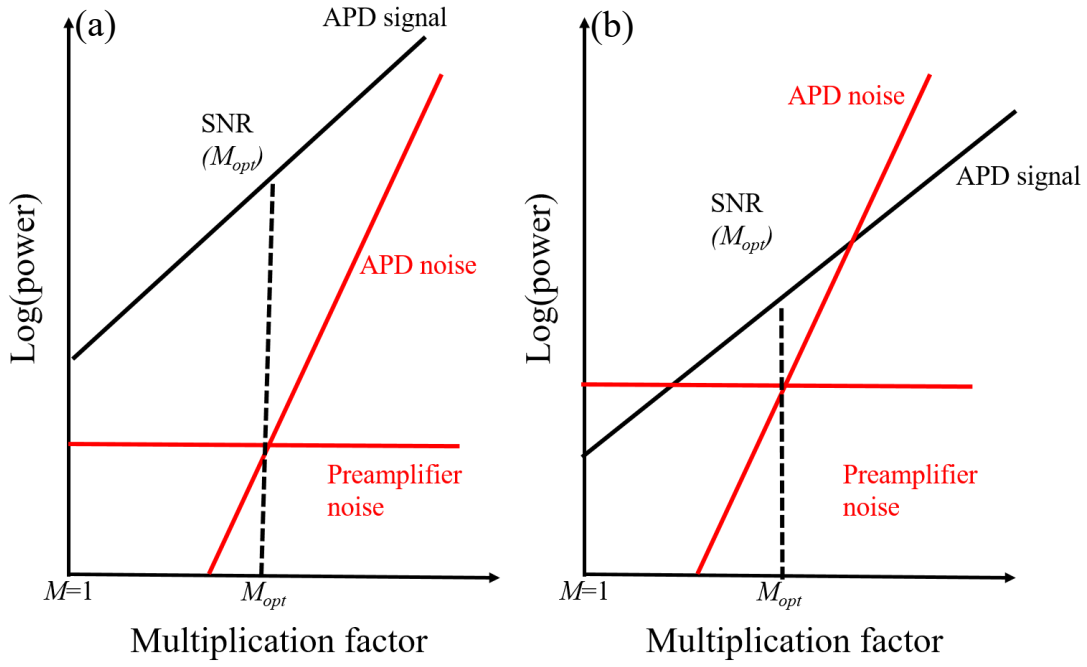

Figure 2.9. Schematic diagram illustrating the advantage of an APD over a p-i-n photodiode in an optical receiver. (a) When the electrical signal power is bigger than the preamplifier noise. (b) When the electrical signal power is smaller than the preamplifier noise

2.8 Avalanche limited bandwidth

The bandwidth of an APD is usually defined as the frequency at which the signal is reduced by 3-dB, and the gain-bandwidth product (GBP) is defined as the product of the avalanche gain and the 3-dB bandwidth of an APD. The resistance-capacitance RC limited time, the carrier transit time, the carrier diffusion time (if carriers are generated outside of the electric field) and the avalanche build-up time affect the bandwidth of an APD. Practically, at high gain, the bandwidth of device is mainly limited by the avalanching build up time. Previously, k of 0 demonstrated that an APD could have the lowest excess noise, even at high multiplication, producing better sensitivity. Emmons [51, 52] reported theoretically for the first time that the 3-dB bandwidth of an APD is reduced at a particular value of M, depending on the the ionization coefficient ratio and the frequency response is independent of M until the product of $kM \sim 1$. Figure 2.10 shows that the 3-dB bandwidth can be independent of M if we utilize an avalanche material with k of 0 and the worst case is at k of 1.

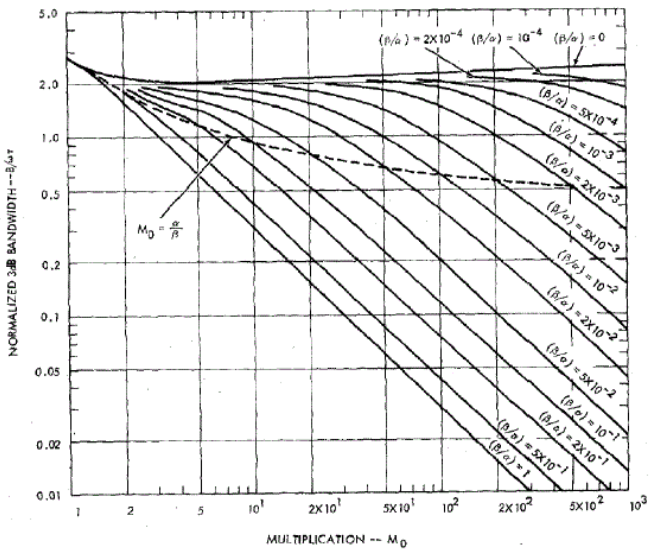

Figure 2.10. Simulation of -3 dB bandwidth versus multiplication with a various ratio of ionization [51].

2.9 References

[1] L. Hall, J. Bardeen, and F. Blatt, "Infrared absorption spectrum of germanium," Physical Review, vol. 95, p. 559, 1954.

[2] G.G. Macfarlane and V. Roberts, "Infrared Absorption of Silicon Near the Lattice Edge," Physical Review, vol. 98, pp. 1865-1866, 1955.

[3] H.C. Casey, D.D. Sell, and K.W. Wecht, "Concentration dependence of the absorption coefficient for n− and p− type GaAs between 1.3 and 1.6 eV," Journal of Applied Physics, vol. 46, pp. 250-257, 1975.

[4] D.E. Aspnes and A.A. Studna, "Dielectric functions and optical parameters of Si, Ge, GaP, GaAs, GaSb, InP, InAs, and InSb from 1.5 to 6.0 eV," Physical Review B, vol. 27, pp. 985-1009, 01/15/ 1983.

[5] H. Burkhard, H.W. Dinges, and E. Kuphal, "Optical properties of In1−xGaxP1−yAsy, InP, GaAs, and GaP determined by ellipsometry," Journal of Applied Physics, vol. 53, pp. 655-662, 1982.

[6] G.G. Macfarlane and V. Roberts, "Infrared Absorption of Germanium near the Lattice Edge," Physical Review, vol. 97, pp. 1714-1716, 1955.

[7] S.Adachi, Physical Properties of III-Y Semiconductor compounds. John Wiley and Sons.1992.

[8] J.P. Zheng, L. Shi, F.S. Choa, P.L. Liu, and H.S. Kwok, "Intensitydependent photoluminescence spectra of semiconductor - doped glasses," Applied Physics Letters, vol. 53, pp. 643-645, 1988.

[9] G. Allan, C. Delerue, and M. Lannoo, "Nature of Luminescent Surface States of Semiconductor Nanocrystallites," Physical Review Letters, vol. 76, pp. 29612964, 1996.

[10] C.H. Henry and D.V. Lang, "Nonradiative capture and recombination by multiphonon emission in GaAs and GaP," Physical Review B, vol. 15, pp. 9891016, 1977.

[11] D.K. Schroder, "Carrier lifetimes in silicon," Electron Devices, IEEE Transactions on, vol. 44, pp. 160-170, 1997.

[12] S.S. Li and W.R. Thurber, "The dopant density and temperature dependence of electron mobility and resistivity in n-type silicon," Solid-State Electronics, vol. 20, pp. 609-616, 1977.

[13] H.A. Zarem, J.A. Lebens, K.B. Nordstrom, P.C. Sercel, S. Sanders, L. E. Eng, et al., "Effect of Al mole fraction on carrier diffusion lengths and lifetimes in AlxGa1−xAs," Applied Physics Letters, vol. 55, pp. 2622-2624, 1989.

[14] M. I. Yernaux, C. Battochio, P. Verlinden, and F. Van De Wiele, "A onedimensional model for the quantum efficiency of front-surface-field solar cells," Solar Cells, vol. 13, pp. 83-97, 1984.

[15] P.A. Wolff, "Theory of electron multiplication in silicon and germanium", Phys. Rev., vol. 95, no. 6, pp. 1415-1420, 1954.
[16] C.L. Anderson and C.R. Crowell, “Threshold energies of electron hole pair production by impact ionization in semiconductors,” Phys. Rev. B, vol. 5, pp. 2267-2272 (1972).
[17] O. Madelung (Ed.), Semiconductor-Basic Data, 2nd Ed., John Wiley and Sons, 1996.
[18] J. Bude and K. Hess, "Thresholds of impact ionization in semiconductors", J. Appl. Phys., vol. 72, no. 8, pp. 3554-3561, Oct. 1992.
[19] J. Allam, "Universal dependence of avalanche breakdown on bandstructure: choosing materials for high-power devices", Jpn. J. Appl. Phys., vol. 36, no. 1(3B), pp. 1529-1542, Mar. 1997.
[20] K.F. Li, D. S. Ong, J.P.R. David, G.J. Rees, R.C. Tozer, P.N. Robson and R. Grey, “Avalanche multiplication noise characteristics in thin GaAs P-i-n diodes,” IEEE Trans. Electron Devices, vol. 45, pp. 2102-2107, Oct. 1998.
[21] C.H. Tan, J.C. Clark, J.P.R. David, G.J. Rees, S.A. Plimmer, R.C. Tozer, D.C. Herbert, D.J. Robbins, W.Y. Leong and J, Newey, “Avalanche noise measurement in thin Si p-i-n diodes,” Appl. Phys. Lett., vol. 76, pp. 3926-3928, Jun. 2000.
[22] W. Fawcett, A.D. Boardman and S. Swain, “Monte Carlo determination of electron transport properties in gallium arsenide”, J. Phys. Chem. Solids, Vol. 31, pp. 1963-1990, Oct. 1970.
[23] J.S.L. Ong, J.S. Ng, A.B. Krysa and J.P.R. David, “Temperature dependence of avalanche multiplication and breakdown voltage in $Al_{0.52}In_{0.48}P$,” J. of Applied Phys, vol. 115, pp. 604507, Feb, 2014.
[24] A.R.J. Marshall, J.P.R David and C.H. Tan, “Impact ionization in InAs electron avalanche photodiodes,” IEEE Trans. On Elec. Devoces, vol. 57, no. 10, Oct. 2010.
[25] C.R. Conwell, “High field transport in semiconductors” Solid State Phys., Suppl. No. 9, eds. F. Seitz, D. Turnbull and H. Ehrenreich, Academic Press, New York, 1967.
[26] R. J. McIntyre, “Multiplication noise in avalanche photodiodes”, IEEE Trans. Electron Devices, vol. ED-13, no. 1, pp. 164 - 168, Jan. 1966.
[27] G.E. Stillman and C. M. Wolfe, “Avalanche Photodiodes”, in Semiconductors and Semimetals, vol. 12, Edited by R. K. Williardson and A. C. Beer, New York: Academic Press, pp. 291 - 300, 1977.
[28] S.A. Plimmer, J.P.R. David, G.J. Rees, and P.N. Robson, "Ionization coefficients in Al x Ga 1- x As (x = 0 - 0.60)," Semiconductor Science and Technology, vol. 15, p. 692, 2000.
[29] R. Van Overstraeten and H. De Man, "Measurement of the ionization rates in diffused silicon p-n junctions," Solid-State Electronics, vol. 13, pp. 583-608, 1970.

[30] L.W. Cook, G.E. Bulman, and G.E. Stillman, "Electron and hole impact ionization coefficients in InP determined by photomultiplication measurements," Applied Physics Letters, vol. 40, pp. 589-591, 1982.
[31] J.S.L. Ong, J.S. Ng, A.B. Krysa, and J.P.R. David, "Impact Ionization Coefficients in Al0.52In0.48P," Electron Device Letters, IEEE, vol. 32, pp. 1528-1530, 2011.
[32] G.E. Bulman, V.M. Robbins, G.E. Stillman, and G.E. Stillman, "The determination of impact ionization coefficients in (100) Gallium Arsenide using avalanche noise and photocurrent multiplication measurements," Electron Devices, IEEE Transactions on, vol. 32, pp. 2454-2466, 1985.
[33] Y.L. Goh, D.J. Massey, A.R.J. Marshall, J.S. Ng, C.H. Tan, W.K. Ng, et al., Avalanche Multiplication in InAlAs, IEEE Transactions on Electron Devices, vol. 54, pp. 11-16, 2007.
[34] R. Ghin, J.P.R. David, S.A. Plimmer, M. Hopkinson, G.J. Rees, D.C. Herbert, et al, Avalanche multiplication and breakdown in Ga0.52In0.48P diodes, IEEE Transactions on Electron Devices, vol. 45, pp. 2096-2101, 1998.
[35] J.S. Ng, C.H. Tan, J.P.R. David, G. Hill and G.J. Rees, “Field dependence of impact ionization coefficients in InGaAs,” IEEE Trans. On Elect. Devices, vol. 50, No. 4, Apr. 2003.
[36] S. Scansen and S.O. Kasap, “Excess noise, gain, and dark current in Ge avalanche photodiodes,” Can. J. Phys., Vol. 70, pp.1070-1075, 1992.
[37] D.S. Ong, K.F. Li, G.J. Rees, J.P.R. David, and P.N. Robson, “A simple model to determine multiplication and noise in avalanche photodiodes”, Journal of Applied Physics, vol. 83, pp. 3426-3428, 1998.
[38] L.J.J. Tan, J.S. Ng, C.H. Tan, and J.P.R. David. Avalanche Noise Characteristics in Submicron InP Diodes, Quantum Electronics, IEEE Journal of 44, no. 4, pp. 378-382, 2008.
[39] Y.L. Goh, A. R. J. Marshall, D. J. Massey, J. S. Ng, C. H. Tan, M. Hopkinson, et al.,Excess Avalanche Noise in In0.52Al0.48As, IEEE Journal of Quantum Electronics, vol. 43, pp. 503-507, 2007.
[40] C.H. Tan, J.C. Clark, J.P.R. David, G.J. Rees, S.A. Plimmer, R.C. Tozer, et al., “Avalanche noise measurement in thin Si p+-i-n+ diodes”, Applied Physics Letters, vol. 76, pp. 3926-3928, 2000.
[41] A.R.J. Marshall, C.H. Tan, M.J. Steer, and J.P.R. David, “Extremely low excess noise in InAs electron avalanche photodiodes,” IEEE Photon. Tech. Lett., vol. 21, no. 13, July 2009.
[42] C. Hu, K. A. Anselm, B.G. Streetman, and J.C. Campbell, “Noise characteristics of thin multiplication region GaAs avalanche photodiodes,” Appl. Phys. Lett., vol.6 9, pp. 3734-3736, Dec. 1996.
[43] K.F. Li, D. S. Ong, J.P.R. David, G.J. Rees, R.C. Tozer, P.N. Robson, and R. Grey, “Avalanche multiplication noise characteristics in thin GaAs p+-i-n+ diodes,” IEEE Trans. Electron Devices, vol. 45, pp. 2102-2107, Oct. 1998.

[44] K.F. Li, S.A. Plimmer, J.P.R. David, R.C. Tozer, G.J. Rees, P.N. Robson, C.C. Button, and J. C. Clark, “Low avalanche noise characteristics in thin InP p+-i-n+ diodes with electron initiated multiplication,” IEEE Photon. Technol. Lett., vol. 11, pp. 364-366, Mar. 1999.
[45] C. Hu, K.A. Anselm, B.G. Streetman, and J.C. Campbell, “Excess noise in GaAs avalanche photodiodes with thin multiplication regions,” IEEE J. Quantum Electron., vol. 33, pp. 1089-1093, Jul. 1997.
[46] K.F. Li, D. S. Ong, J.P.R. David, R.C. Tozer, G.J. Rees, P.N. Robson, and R. Grey, “Low excess noise characteristics in thin avalanche GaAs diodes,” Electron. Lett., vol. 34, pp. 125-126, Jan. 1998.
[47] M.M. Hayat, B.E.A. Saleh, and M.C. Teich, “Effect of dead space on gain and noise of double-carrier-multiplication avalanche photodiodes,” IEEE Trans. Electron Devices, vol. 39, pp. 546-552, Mar. 1992.
[48] M.A. Saleh, M.M. Hayat, O.-H. Kwon, A.L. Holmes, J.C. Campbell, B. E. A. Saleh, et al., "Breakdown voltage in thin III–V avalanche photodiodes," Applied Physics Letters, vol. 79, pp. 4037-4039, 2001.
[49] M.A. Saleh, M.M. Hayat, O.-H. Kwon, A.L. Holmes, J.C. Campbell, B.E.A. Saleh, et al., "Breakdown voltage in thin III–V avalanche photodiodes," Applied Physics Letters, vol. 79, pp. 4037-4039, 2001.
[50] G.E. Stillman and C.M. Wolfe, “Avalanche photodiodes,” in Semiconductors and Semimetals, vol. 12, Eds. R. K. Willardson and A. C. Beer, New York: Academic Press, 1977, pp. 291-393.
[51] R.B. Emmons, “Avalanche photodiode frequency response,” J. Appl. Phys., vol. 38, no. 9, pp. 3705–3714, 1967.
[52] R.B. Emmons and G. Lucovsky, "The frequency response of avalanching photodiodes," IEEE Trans. Electron Devices,, vol. 13, pp. 297-305, 1966.

CHAPTER 3:

EXPERIMENTAL TECHNIQUES

3.1 Electrical characterization details

3.1.1 Capacitance-voltage (CV) measurement

Capacitance-voltage (CV) characteristics of the device under test (DUT) were performed using a HP4275A LCR meter. The capacitance of DUT as a function of reverse bias was measured by applying a sinusoidal test signal with 50 mV at a frequency of 1 MHz. CV measurements were used to obtain the capacitance, built-in voltage, total depletion width and doping profile of the DUT. Devices of three different diameters were measured to ensure that the capacitance per unit area is constant.

To estimate information about the doping profile and depletion region of the DUT, the CV measurements were calculated using an electrostatic model. Using Poisson's equation and assuming that the doping profile is abrupt, the electric field gradient was expressed as

$$\frac{dE}{dx} = \frac{qN}{\varepsilon_0 \varepsilon_r} \qquad (3.1)$$

Where E is the electric field, q is the elementary electronic charge, ε_r is the dielectric constant of the device's material, ε_0 is the permittivity of free space, and N is the doping density. The total area under the curve of the electric field profile is equal to the sum of the applied voltage (V_{app}) and built-in voltage (V_{bi}). So the CV measurements can be fitted by an algorithm that uses the doping density and the thickness as adjustable parameters. The calculated depletion width obtained from the electric field profile should fit the measured capacitance as much as possible.

Furthermore, the capacitance of the DUT at a given applied reverse bias voltage and the doping density at a certain reverse bias can be, respectively, determined by

$$C = \frac{\varepsilon_0 \varepsilon_r A_D}{w} \qquad (3.2)$$

$$N(w) = \frac{2}{q\varepsilon_0\varepsilon_r A_D^{\,2}} \left[\frac{dV_t}{d(\frac{1}{C^2})} \right] \qquad (3.3)$$

Where A_D is the area of the DUT, w is the total depletion length, and V_t is the total voltage across the DUT. The V_{bi}, at equilibrium, can be estimated by plotting $1/C^2$ against bias and a straight line intercept at $1/C^2 = 0$ give V_{bi}. It is worth observing that this method of estimating the V_{bi} is based on the assumption on an abrupt single-sided junction with constant doping density. The dielectric constant for AlAsSb is assumed to be 10.95 [1].

3.1.2 Current-voltage (IV) measurement

Current-voltage (IV) measurement is the most fundamental characterization methodology used. This measurement can be achieved by applying a bias voltage across the DUT and measuring the value of the resulting current. Either a Hewlett Packard HP4140B pico-ammeter or a Keithley 236/237 source measurement unit (SMU) were used to measure the forward and reverse IV, and they are controlled by a computer. From IV measurements, we may discover the characteristics of a fabricated diode, such as reverse leakage current, I_d, breakdown voltage, V_{bd}, series resistances, R_s and ideality factor, n. Therefore, this is normally the first test after the device fabrication and needs to repeat on devices with different size.

The dark leakage currents, which is a fundamental parameter for an APD, come from either bulk and/or edge leakage currents. Bulk leakage is generated by generation-recombination and tunnelling processes, which scales with the area, and edge leakage is affected by leakage paths at the mesa periphery and therefore scales with the device perimeter. The contributions of the bulk and edge leakage currents were found by

$$J_{Area} = \frac{I_{dark}}{\pi r^2} \qquad (3.4.a)$$

$$J_{Perimeter} = \frac{I_{dark}}{2\pi r} \qquad (3.4.b)$$

Where r is the radius of the DUT.

From the dark forward IV measurements, the quality of the material, the formation of the junction and the quality of the contacts can be obtained. The ideal forward IV characteristics can be expressed by [2]

$$I_F = I_o\left[\exp\left(\frac{qV_t}{nk_BT}\right)-1\right] \qquad (3.5a)$$

$$I_F = I_o\left[\exp\left(\frac{q(V_t - IR)}{nk_BT}\right)-1\right] \qquad (3.5b)$$

Where I_0 is the saturation current depending on the cladding doping concentration and the electron and hole diffusion lengths, V_t is the total voltage drop across the DUT, q is the electron charge, k_B is Boltzmann's constant, T is the temperature, and n is the ideality factor with a value between 1 and 2. A value of n near to 1 means that diffusion is the core mechanism, while a value of n closer to 2 indicates that generation-recombination is dominant. Hence, the device has significant defects when $n \sim 2$. Normally, there is an equivalent series resistance, R, due to the effect of series resistance as shown in Equation (3.5b). The multiplication characteristics are profoundly affected by equivalent series resistance when there is a significant voltage drop across it as it reduces the applied voltage across the depletion region. This therefore, limits the maximum achievable measured gain and a high value of R has to be avoided when measuring multiplication. Figure 3.1 shows an example of measured multiplication with high series resistance.

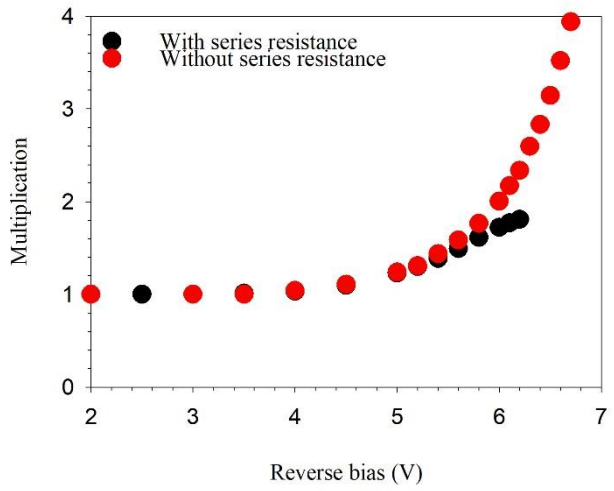

Figure 3.1. Illustration of the effect of voltage drop on the multiplication.

There are a few mechanisms that can occur as the reverse bias increases, which will directly raise the dark current and degrade the SNR of an APD. These typically include diffusion (I_{diff}), generation and recombination ($I_{G\&R}$), band to band tunnelling (I_{tunn}) and surface leakage (I_{surf}). The relationship is given by the following equations [2].

$$I_{diff} = I_o\left[\exp\left(\frac{qV}{k_BT}\right)-1\right] \qquad (3.6)$$

$$I_{G-R} = \frac{qn_iAw}{\tau_{eff}} \qquad (3.7)$$

$$I_{tunn} = \frac{(2m^*)^{0.5}q^3EVA}{4\pi^2\hbar E_g^{0.5}}\exp\left(-\frac{\alpha_T(m^*)^{0.5}E_g^{0.5}}{q\hbar E}\right) \qquad (3.8)$$

$$I_{surf} = \frac{V_b}{R} \qquad (3.9)$$

Where n_i is the intrinsic carrier density, A is the cross-sectional area of the junction, τ_{eff} is the effective carrier lifetime, m^* is the electron effective mass, $\hbar$ is the reduced Plank's constant, and α_T is a parameter dependent on the detailed shape of the barrier and is of the order of unity. The surface leakage current is mainly due to the conducting surface of an etched mesa.

3.2 Photo-response measurement

Photo-response measurements were performed to discover the optical responsivity of the photo-sensitive material in the APDs. The photo-response setup is shown in Figure 3.2. As we can see, light from a 100 W tungsten bulb source on the right-hand side is injected into a monochromator after the focusing lenses. The light from the output of monochromator was focused onto the DUT using another pair of focusing lenses. The image of the DUT and excitation light spot were shown on a monitor through the beam splitting cube (BSC) that was illuminated by a white light source on the top. The light from the output of a monochromator was modulated at 180 Hz by a mechanical chopper. There is a Keithley 236 or 237 source meter unit (SMU) to bias the DUT and a Stanford Research SR830 lock-in amplifier (LIA) to detect the resultant photocurrent. A software program called SCADAS was used to collect the data and control the wavelength of the monochromator. A Hamamatsu PD S5973-02 [3] was used as the reference photodiode to calculate the quantum efficiency of the DUTs due to the similarity of photo-response performance. It is worth indicating that the 210 μm radii devices in this work have a similar photosensitive area as the commercial photodiode, but the optical power on DUTs is not similar to the power on the commercial device. This is because some of the top metal contact blocks the light going in. We estimated that the photosensitive area of 210 radii devices was 63% of that of a commercial device by comparing the area difference between the 210 μm radii devices and the commercial device. The resultant photocurrent is calculated by

$$I_{ph} = \frac{\frac{LIA}{10} \times Sensitivity}{0.45 \times resistance} \qquad (3.10)$$

Where LIA means the reading of LIA and Sensitivity means the sensitivity of LIA. The choice of sensitivity was dependent on the highest signal level.

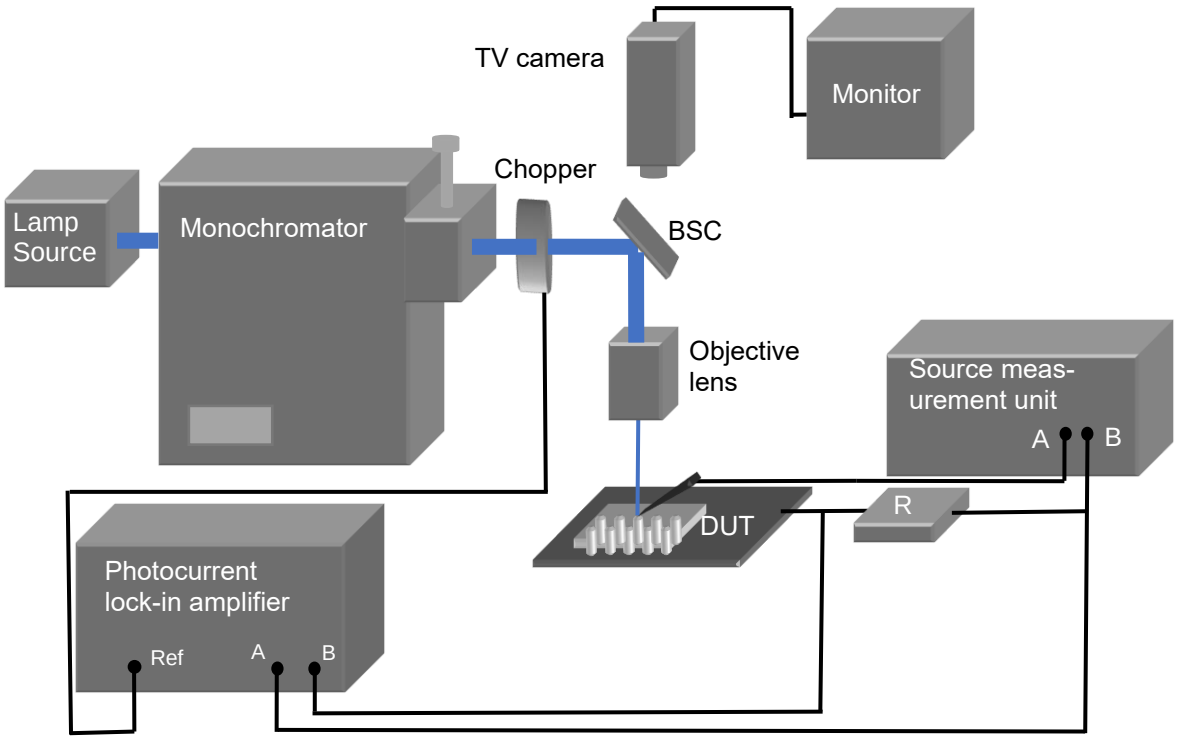

Figure 3.2. Schematic diagram of photo-response characteristics experimental setup.

3.3 Photo-multiplication measurement

Avalanche multiplication resulting from impact ionization is an important process in APDs. An accurate determination of impact ionization coefficients needs pure electron and hole initiated multiplication characteristics from p-i-n and n-i-p structure with a range of avalanching thickness. Figure 3.3 shows a schematic of the phase-sensitive photomultiplication measurements setup. A small laser spot (about ~10 um diameter) was focused onto either the top of a p-i-n or n-i-p device by some adjustable mirrors and focusing lenses. The image of the device and the laser spot were also viewed on a monitor via a camera and a beam splitting cube (BSC), which is similar to the photo-response measurement setup. A Keithley 236 or 237 SMU was used to bias the DUT and the resistor. The laser source was modulated at about 180 Hz by a mechanical chopper. A LIA measured the resultant photocurrent via the voltage drop across a resistor. It is well known that the photocurrent results from DUT are a function of the applied voltage. Multiplication value, ideally, are not affected by optical power. However, the multiplication value is sometimes lower at high optical power due to local temperature heating. It is necessary to check the absence of heating effects by changing the intensity

of the laser source using different neutral density (ND) filters. Obtaining a pure injection of holes and electrons was controlled by the wavelength of the laser source, which will be detailed later.

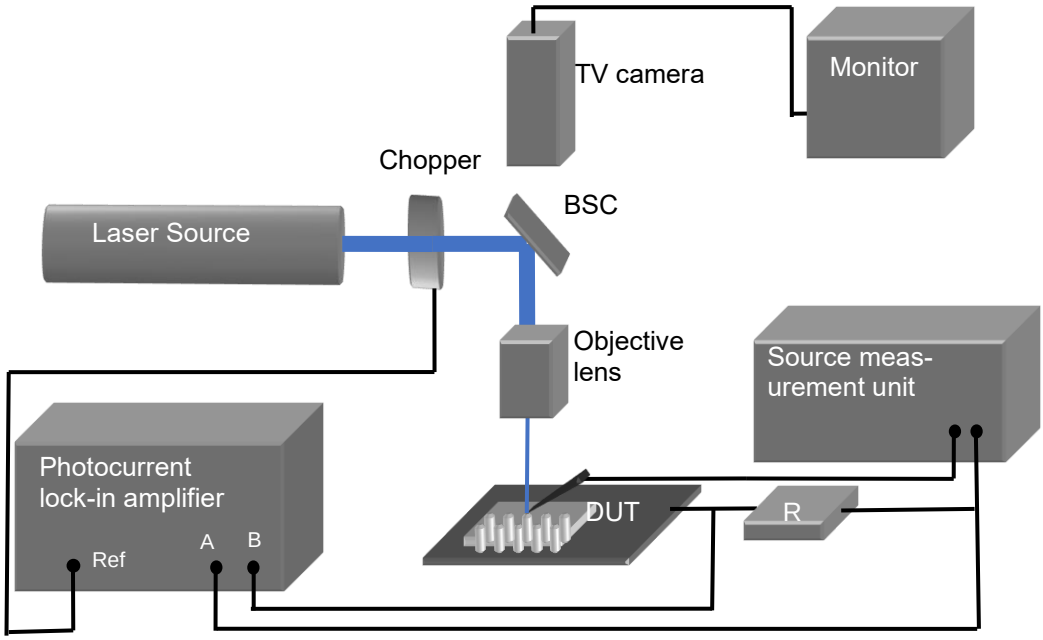

Figure 3.3. Schematic diagram of the AC photo-multiplication set-up for top illumination.

When the dark current was significantly lower than I_{ph} (by >2orders of magnitude), the SMU could be used to measure both the dark current and the total current. The dark current, I_{dark}, was without laser illumination and the total current, I_{total}, was with laser illumination. We could determine the multiplied photocurrent as a function of bias through I_{total}-I_{dark}. However, a direct measurement was only used for the low dark current cases. The measurement set-up for DC method is similar except for the resistor and LIA. In this work, due to the relatively high surface dark currents, the photocurrent measurements used phase sensitive detection techniques.

The multiplication characteristics were calculated by normalising the total photocurrent, I_{ph}, and primary photocurrent, I_{pr}. The I_{pr} increases as the reverse bias increases because of the distance between the surface and the edge of the depletion region varies under high reverse bias, which is similar to the early effect in a bipolar junction transistor. Woods et al. [4] estimated the I_{pr} in an abrupt p-n junction as

$$Ipr = \frac{qG_0}{\cosh(L / L_{pn})} \qquad (3.11)$$

where G_o is the carrier photogeneration rate at the cladding region, L is the distance between the illuminated surface and the depletion edge, L_{pn} is the minority carrier diffusion length. However, in reality, Equation 2.10 can simplify as

$$Ipr = aV + b \qquad (3.12)$$

Where a and b are constants if $L(V) >> L_{pn}$.

As we mentioned before, there are two type carriers, electrons and holes, undergoing impact ionisation in a large electric-filed (avalanching region). During multiplication measurements, it is possible to control the primary photocurrent injected into the multiplication region. As shown in Figure 3.4, the top cladding layer of a p-i-n or n-i-p structure is illuminated with the incoming light of two different wavelengths ($\lambda_1 < \lambda_2$), respectively. It is obvious that the selected shorter wavelength, λ_1, is no longer absorbed after the top cladding layer. And the selected longer wavelength, λ_2, can generate carriers in the avalanche i-region almost uniformly throughout the structure due to a very low absorption coefficient. Therefore, the shorter-wavelength light will provide pure carrier injection into the avalanche region giving M_e on the p-i-n or M_h on the n-i-p while the longer-wavelength light will provide a mixed carrier injection multiplication characteristic (M_{mix}). Side injection is shown in Figure 3.5. In this case, the shorter-wavelength light accidentally enters the avalanche region due to the relatively large laser spot or when used on the smallest diameter device. Light is absorbed and carriers are generated everywhere.

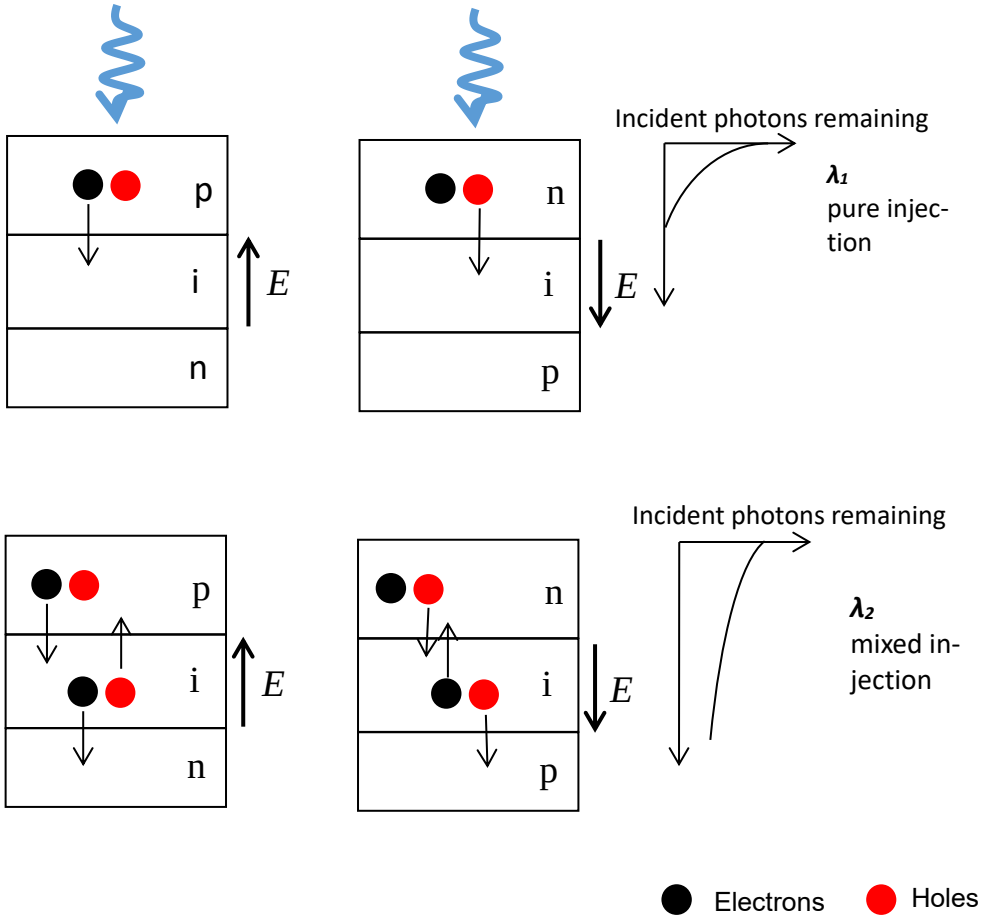

Figure 3.4. Schematic diagram of single carrier injection and a mix injection through different wavelengths. Red circle presents electrons and blue circle presents holes. The arrows show the diffusion direction.

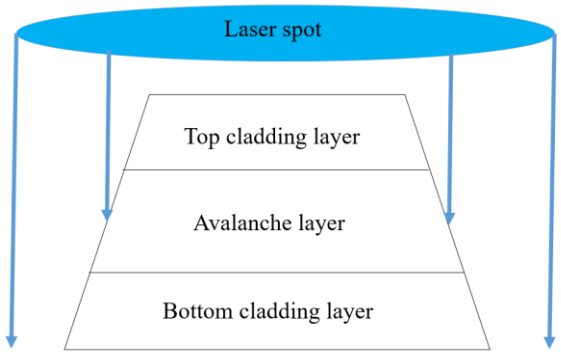

Figure 3.5. Schematic diagram of side injection due to the unfocused laser spot or used the smallest diameter device.

3.4 Excess noise measurement

Avalanche excess noise was measured using the setup as shown in Figure 3.6. Similar

to the previous multiplication setup, the DUT was biased using an SMU and light through a mechanical chopper was aligned on the optical window of the DUT. A trans-impedance amplifier (TIA), which applied a gain of 2200 VA^{-1} was used to convert the photocurrent signal into a proportional square waveform voltage signal at the chopper frequency. The signal amplified by a unity-gain amplifier was measured by one of LIAs to determine the photocurrent. The output of the TIA (signal of photocurrent and its multiplied noise) is then connected to the bandpass filter (MiniCircuit SBP 10.7) with a centre frequency of 10 MHz and a bandwidth of 4.2 MHz for removing the photocurrent signal. An additional amplifier stage was used to further amplify the resulting noise voltage from the output of the bandpass filter before it is converted to the mean square value by a power meter (a squaring and averaging circuit). The output of a power meter was fed into another LIA to measure the noise power. An attenuator was placed between the amplifier output and the noise power meter in the cascade to restrict very high signal to the power meter. Both LIAs have an identical frequency at the frequency of the mechanical chopper. A detailed description of the noise measurement system can be found in [5, 8].

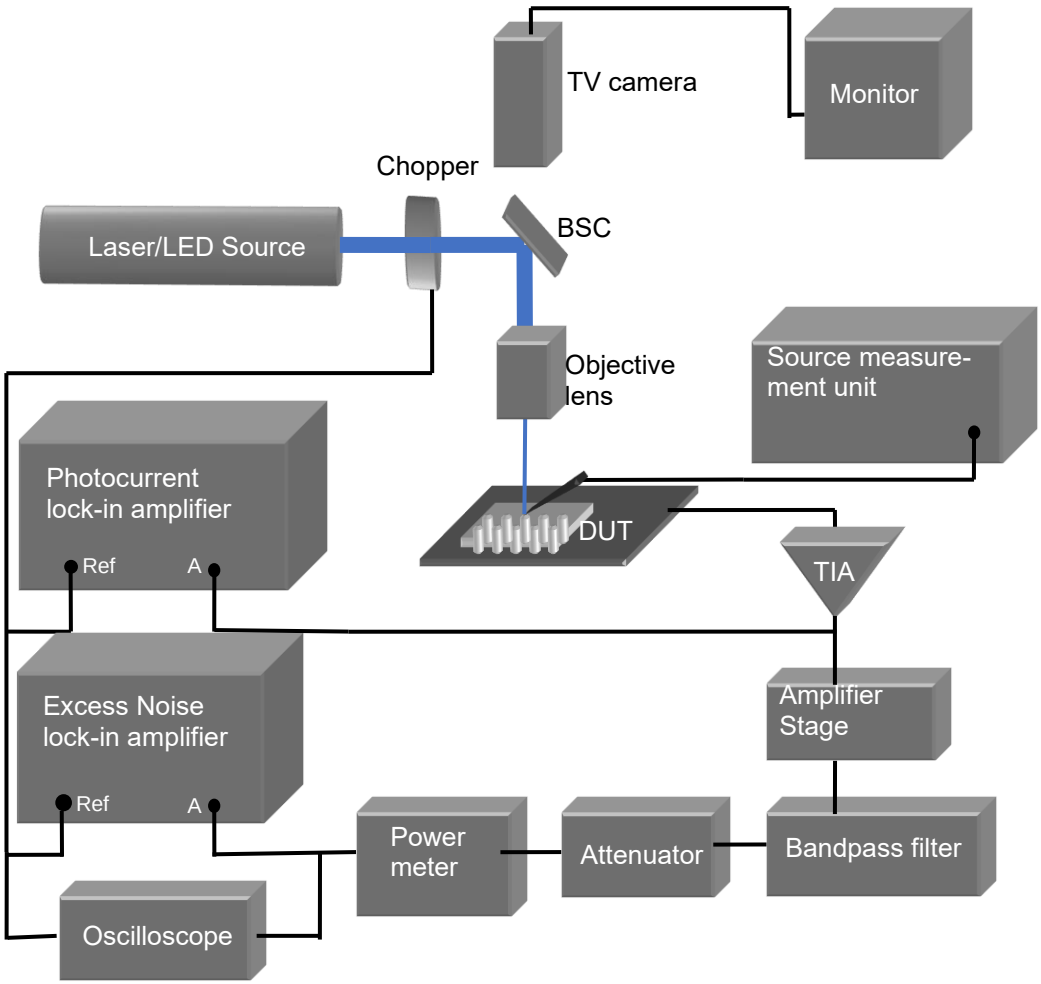

Figure 3.6. Schematic diagram of the experimental set up used to measure the excess noise.

The analysis of photocurrent to determine M is similar to the multiplication measurement shown in the previous section. The excess noise factor, F for a given M, is determined by [6]

$$F = \frac{N_{DUT}}{N_{ref}} \qquad (3.13)$$

In this work, the reference device selected was a commercial Si p-i-n photodiode (BPX65). BPX65 has a unity gain ($M = 1$) and has a well-known junction capacitance. Figure 3.7 shows the measured noise power (LIA2) as a function of photocurrent (LIA1) of BPX65 with a reverse bias voltage of 5 V using a different wavelength of light. These results present full shot noise due to operating under non-avalanching conditions. Therefore, for any DUTs operating under the avalanching model, the actual excess

noise can be determined by referring to BPX65.

The ratio of the noise power to photocurrent for an ideal device is expressed by

$$K = \frac{N_{si}}{I_{ph}} = 2eB_{eff}(C_{si})A^2 \qquad (3.14)$$

Where $B_{eff}(C_{si})$ is the effective noise bandwidth (ENBW), which is the variation of the transimpedance gain with capacitance. A is the total gain of the system. For a unity gain device such as BPX65, the noise power versus photocurrent is linear, and the slope is also given in Equation (3.14). The noise power of the DUT is given by

$$N_{DUT} = 2eIB_{eff}(C_{DUT})A^2MF(M) \qquad (3.15)$$

Where N_{DUT} is the measured noise power, $B_{eff}(C_{DUT})$ is the effective noise bandwidth of the DUT at a particular capacitance. M is the multiplication, and I is the multiplied photocurrent. By arranging Equation (3.14) and (3.15), the excess noise factor was calculated using

$$F(M) = \frac{N_{DUT}}{K \times MI} \times \frac{B_{eff}(C_{si})}{B_{eff}(C_{DUT})} \qquad (3.16)$$

The excess noise measurement was also performed using different optical powers on devices to ensure consistency and reproducibility. Figure 3.7 shows the photocurrent noise power against photocurrent for a commercial silicon reference device (BPX65) under different wavelengths and intensity while at unity gain and for P1 with 420 nm excitation under increasing reverse bias.

More detail on the phase detection technique can be found in [7].

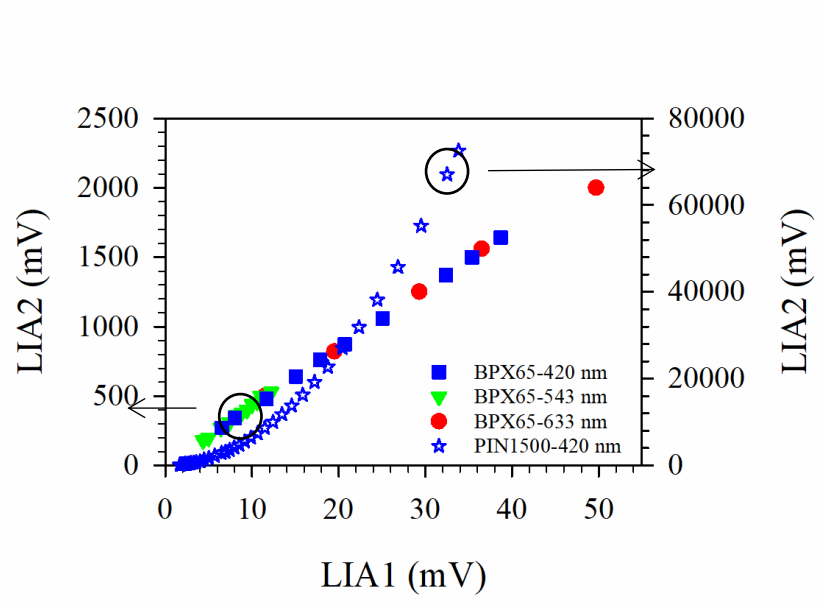

Figure 3.7. Measured noise power for BPX65 with different wavelengths and optical powers as well as that for an AlAsSb diode.

3.4 References

[1] D.W. Palmer, www.semiconductors.co.uk, 2006.02.

[2] S. M. Sze and K. K. Ng, "Physics of semiconductor devices, 3rd. Edition," John Wiley and Sons Inc., 2007.

[3] "High speed photodiodes (S5973 series: 1 GHz)," Hamamatsu Photonics K. K.1 Sept 2015 2012.

[4] M. H. Woods, W. C. Johnson, and M. A. Lampert, "Use of a Schottky barrier to measure impact ionization coefficients in semiconductors," Solid-State Electronics, vol. 16, pp. 381-394, 1973.

[5] K. F. Li, “Avalanche noise in submicron GaAs and InP structures,” PhD Thesis,

University of Sheffield, 1999.

[6] K. F. Li, D. S. Ong, J. P. R. David, G. J. Rees, R. C. Tozer, P. N. Robson, and R. Grey, "Avalanche multiplication noise characteristics in thin GaAs p+-i-n+ diodes", IEEE Trans. Electron Dev., vol. 45, no. 10, pp. 2102-2107, Oct. 1998.

[7] Sandford Research System, “SR830 DSP Lock-in Amplifer,” Operating manual and programming reference rev. 1.4, Dec. 1995.

[8] K.S. Lau, C.H. Tan, B.K. Ng, K.F. Li, R.C. Tozer, J.P.R. David and G.J. Rees, “Excess noise measurement in avalanche photodiodes using a transimpedance amplifier front-end,” Meas. Sci. Technol., vol. 17, pp. 1941-1946, Jun. 2006.

CHAPTER 4:

GROWTH, FARBICATION AND ABSORPTION COEFFICIENTS IN AlAsSb

4.1 Introduction

The semiconductor material $AlAs_{0.56}Sb_{0.44}$ (hereafter referred to AlAsSb), lattice-matched on InP has been widely investigated for high-speed optoelectronic device applications such as ultrafast cross-phase modulators [1], quantum-cascade lasers [2], distributed Bragg reflectors [3], multi-junction solar cells [4], and more recently, it has been used for demonstrating high gain-bandwidth product and low excess noise avalanche photodiodes [5, 6]. In several of these devices, an accurate knowledge of the material absorption coefficient as a function of wavelength is needed to optimize their performance. A thicker AlAsSb is sometimes required to extract the properties of bulk material. In this chapter, three p-i-n structures and two n-i-p structures were grown using a digital alloy growth technology by Molecular beam epitaxy reactor and fabricated by standard optical lithography and wet etching. Several methods were used to determined growth quality like X-ray diffraction and transmission electron microscopy. By looking at the photo-response spectrum at low reverse bias, absorption coefficient was determined.

4.2 Layer details

4.2.1 Digital alloy growth technology

Random alloy (RA) growth is normally used to grow mixed-anion alloys by molecular beam epitaxy (MBE) reactor. The atoms are directly deposited on the sample surface with correct growth conditions to achieve the targeted alloy composition. RA growth technique has been successfully demonstrated in many semiconductors such as GaAs, AlGaAs, InP, InAlAs and InGaAs. These materials have only one group-V element which could be much easier to be grown as they have unit sticking coefficient on the

growth surface. Therefore, setting atoms/flux on the surface based on the mole ratio in the alloy is used to achieve the targeted alloy composition. The commercial company, IQE, successfully provided two thin wafers to Sheffield (namely P4 and P5 in this thesis) using RA growth technique in 2011. Unfortunately, The third wafer with 1 μm thickness showed strong oxidation and was not usable. The grown structure comprises a top AlAsSb cladding layer of 400 nm (p^+), a nominal AlAsSb undoped avalanche layer of 100/250 nm and a bottom AlAsSb layer of 50 nm (n^+). These two p-i-n configurations are sandwiched between a 50 nm heavily doped InGaAs on the top and a 1000 nm InGaAs at the bottom. Ref [6, 7] reported the reverse dark current, the wavelength dependence of multiplication, the temperature dependence of multiplication and the wavelength dependence of excess noise from P4 and P5. The National Epitaxy Facility at Sheffield started to regrow the same structure but with much thicker avalanche region since 2015, unfortunately, most wafers were unacceptable. It is because that our targeted alloy, AlAsSb, has one group-III and two group-V elements, and the growth is much more complicated than that of alloys with only one group-V element. The sticking coefficients on the growth surface for the group-V element are normally varied as functions of growth rate, growth temperature and their mole ratio. Undesired crystalline disorders are easily created by the wide miscibility gap [8, 9], therefore, it is very difficult to grow a thick structure using RA technology.

Zhang Y.H. [10] has demonstrated an accurate method for growing $AlAs_xSb_{1-x}$ by modulated molecular beam epitaxy (MMBE). This is generally called digital alloy (DA) growth technology. This method uses short-period superlattices, and the advantages of DA are giving identical structural, optical and electronic properties while providing precise control over alloy composition and reproducibility. Compared with RA growth technique growing digitally by MBE shifts the emphasis placed on control of incident fluxes (hard) to shutter timing and layer thicknesses control (easy). In 2016, J. Campbell's group successfully demonstrated $Al_xIn_{1-x}As_ySb_{1-x}$ lattice-matched to GaSb substrates used DA growth technology by MBE. The layers used a digital alloy period of 10 monolayers (ML) [11] or 3 nm [12], and the binary alloys follow the shutter sequence AlSb, AlAs, InSb and InAs. Therefore, DA technology looks like a promising technology for growing thick AlAsSb homojunction wafers.

4.2.2 AlAsSb device growth and fabrication

The AlAsSb p-i-n and n-i-p structures are grown on epi-ready n-InP (001) and p-InP (001) substrates, respectively, via DA growth technology in a Veeco GEN930 MBE reactor, in which both As_2 and Sb_2 fluxes are supplied using valved cracker cells by Dr Liang in the University of California, Los Angeles (UCLA). Before the material growth, the InP substrate temperature was raised to 540^0C for 3 mins under As_2 to desorb the surface oxide. After oxide removal, the substrate was cooled to 500^0C for material growth. The digital AlAsSb layer was realised by periodically alternating the As_2 and Sb_2 shutter while maintaining a steady Al flux during deposition, resulting in AlSb and AlAs equivalent sequence of 4.0 and 0.44 monolayers. The layers grown include five homojunction p-i-n/n-i-p structures (The structures are labelled P1-P3 and N1-N2 to enable easy reference). The nominal multiplication region thicknesses are w = 1.5, 1.0 and 0.6 μm, respectively. The multiplication region is sandwiched between a 300-nm p^+/n^+ AlAsSb and a 100-nm p^+/n^+ AlAsSb cladding layers with Be(p+) and Te(n+) doping concentrations of 2.0×10^{18} cm^{-3}. The structure also has a highly doped (1.0×10^{19} cm^{-3}) top 20-nm and bottom 500-nm InGaAs contact layers. The top thin InGaAs cap prevents oxidation of AlAsSb and also helps form a good metal contact.

Figure 4.1(a) shows an example of X-ray diffraction (XRD) results. The clear peak and fringes show that InGaAs and AlAsSb are reasonably lattice-matched to InP substrates. Figure 4.1(b) shows a measured cross-section high-resolution transmission electron microscopy (TEM) picture of the digital AlAsSb layer. A clear sign of bright (AlAs)/dark (AlSb) layer separation is observed suggesting that the alternating shutter sequence has produced modulated contrast in the digital layer. Figure 4.1(c) shows scanning electron micrograph cross-section demonstrating close agreement with the design thickness and no dislocations at the InGaAs/AlAsSb interface. Results shown in Figure 4.1(a)-(c) were done by Dr. Liang at UCLA. However, some parts of wafers are extremely unstable, as shown in Figure 4.1(d), and P1 is significantly damaged during the shipping. Photoluminescence (PL) measurements demonstrate a strong light emission at ~770 nm, as shown in Figure 4.2. The measurements were under different laser power. Results in Figure 4.2 were done by a colleague at Sheffield. Here, initial material characterisation demonstrated that the layer surface had specular reflection

and both InGaAs and AlAsSb layers show near latticed matching to theInP substrate. So it is promising to continue the further device characterisation.

(a)

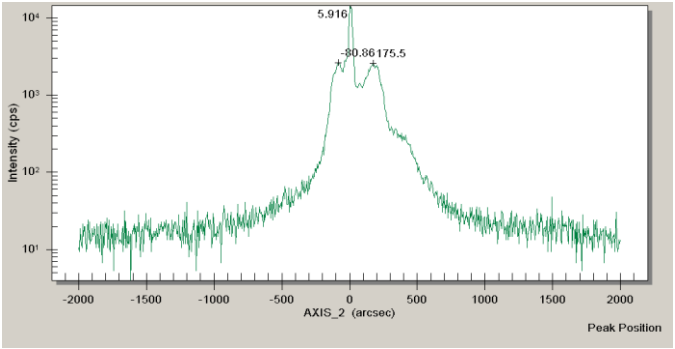

(b)

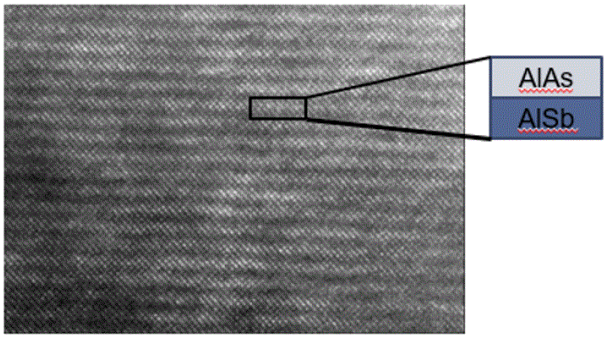

(c)

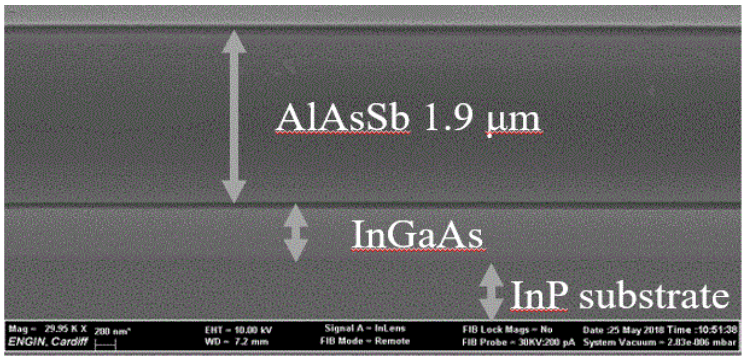

(d)

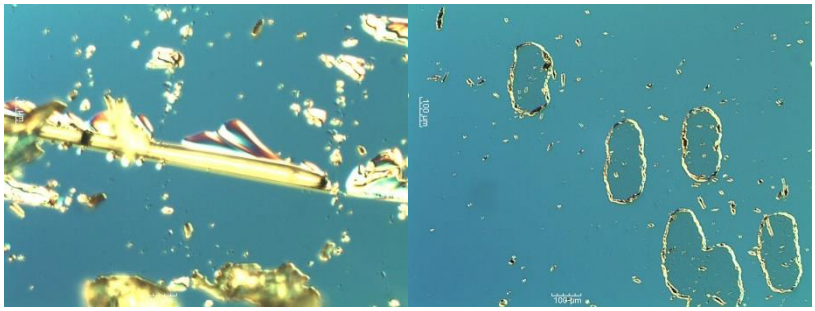

Figure 4.1. (a) XRD peak of InP (middle), InGaAs (left) and AlAsSb (right) in P2. (b) Cross-section bright filed high-resolution TEM images for the AlAsSb digital alloy with a clear AlAs/AlSb layer contrast. One period is 1.31 nm with rapidly alternating layers of AlAs (1.7Å) and AlSb (11.4Å). (c) SEM cross-section photo of the P1. (d) Normaski of P3 and P2 done at Sheffield.

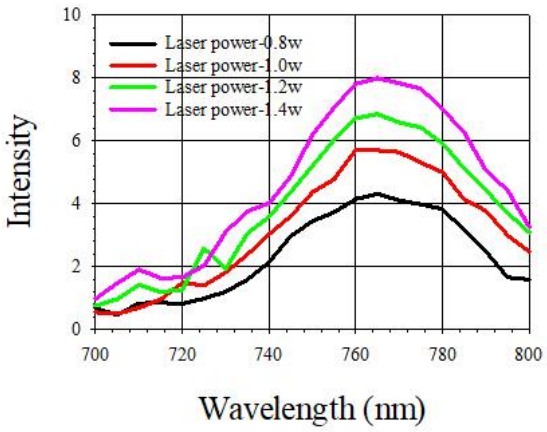

Figure 4.2. Measured PL under different laser power with 665 nm filter on P2.

As we know, AlAsSb is very easy to oxidise when exposed to air, which makes it prone to significantly high surface leakage current for APDs. The previous study showed that the challenges of fabrication are the existence of Antimony significantly increase in the oxidation depth in AlAsSb [13], and Aluminium rich materials combine with oxygen atoms easily [14]. Dr Xie J. Systematically investigated the etching recipe and reported this in her thesis [15], and we used the same etching recipe. The only difference here is that we used a new mask for the circular mesa diodes with diameters of 70, 120, 220 and 420 μm. These high quality wafers were fabricated into mesa diodes by standard optical lithography and wet etching where a 2 : 1 mixture of citric acid (1 g citric acid powder to 1 ml of de-ionised water (DIW)) and hydrogen peroxide (H_2O_2) is used for the removal of the InGaAs cap layer and a 1 : 2 : 10 mixture of hydrochloric acid, diluted H_2O_2 (with a ratio of 1 part peroxide to 9 parts DIW) and DIW to etch the AlAsSb layer. Ti-Au was used to form the top and bottom metal contacts. Figure 4.3 shows a schematic diagram and two fabricated circular mesa diodes with optical windows, respectively. Figure 4.4(a)-(b) shows devices had serious oxidation after annealing, even this was happen at the room temperature as shown in Figure 4.4(c). In this work, fabrication was down by Dr Xie S.Y. in Cardiff and Lim L.W. at Sheffield.

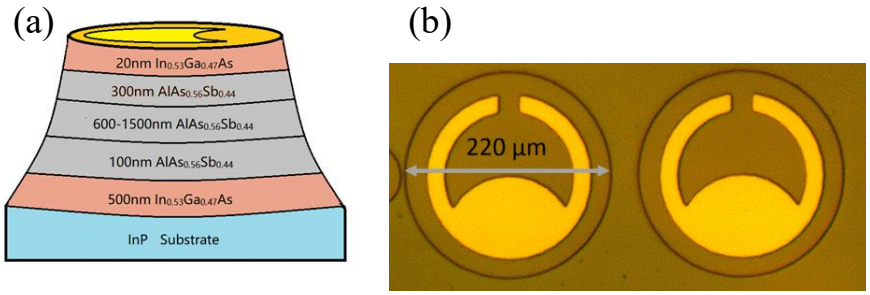

Figure. 4.3. (a) Schematic diagram of the mesa device (600 – 1500 nm AlAsSb thick intrinsic region). (b) Plan view of two 220 µm diameter devices showing the top contact.

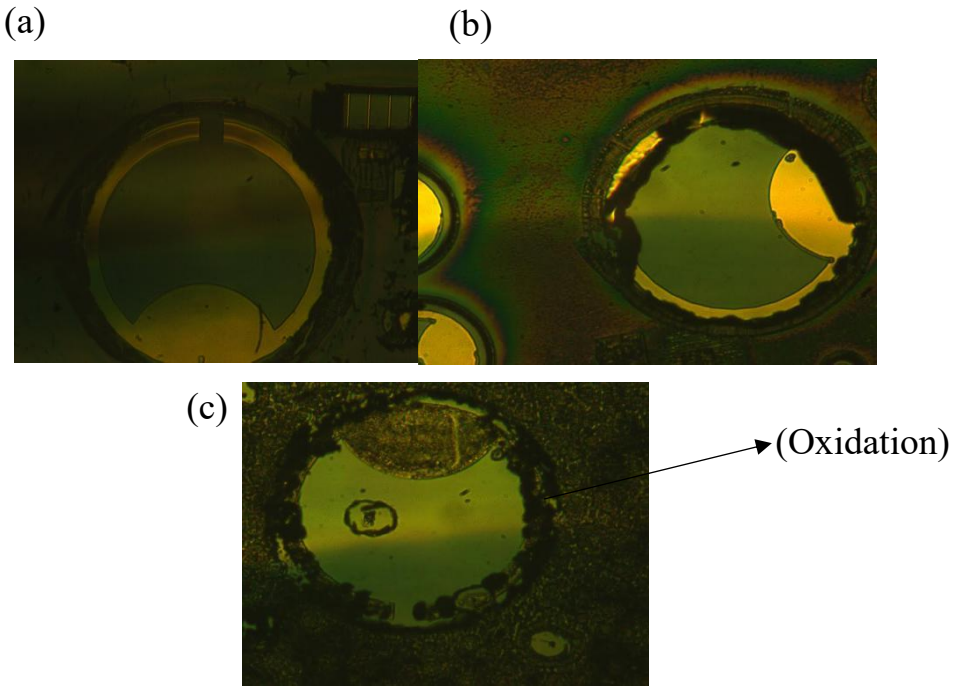

Figure 4.4. Photographs of P3 after the first run fabrication. (a) No annealing. (b) annealing under 340 degree. (c) annealing under 420 degree.

4.3 Electrical characterisation

4.3.1 CV measurement

The typical capacitance as a function of reverse bias measured on P1-P3 and N1-N2 with mesa diameters of 420 µm are shown in Figure 4.5. It was found that the CV profiles of the diodes on each layer scale with device area proving that the diodes are properly isolated. After an initial decrease in capacitance with bias, the capacitance is

approximately constant above 20 V for P1 and N1, 15 V for P3 and 6 V for P2 and N2. This means that the intrinsic region is fully depleted beyond these biases and there is negligible depletion in the heavily doped cladding regions. The cladding layer doping density (assuming $p^+ = n^+$), the i-region thickness and i-region doping density are summarized in Table 4.1, and the P4-P6 refer to thin avalanching layers investigated previously [15]. The doping profiles and i-region thickness were modelled by solving Poisson's equation. Figure 4.6(a) shows the calculated doping density against the depletion width. The i-region background doping density varies between $5 \times 10^{15} - 10 \times 10^{15}$ cm^{-3} resulting in a tapered electric-field profile in the intrinsic region and the avalanche thickness is close to the nominal growth values. Figure 4.6(b)-(d) shows simulations of the electric field of P1-P3. The built-in voltage was estimated to be around 1.5 V by plotting $1/C^2$ versus bias.

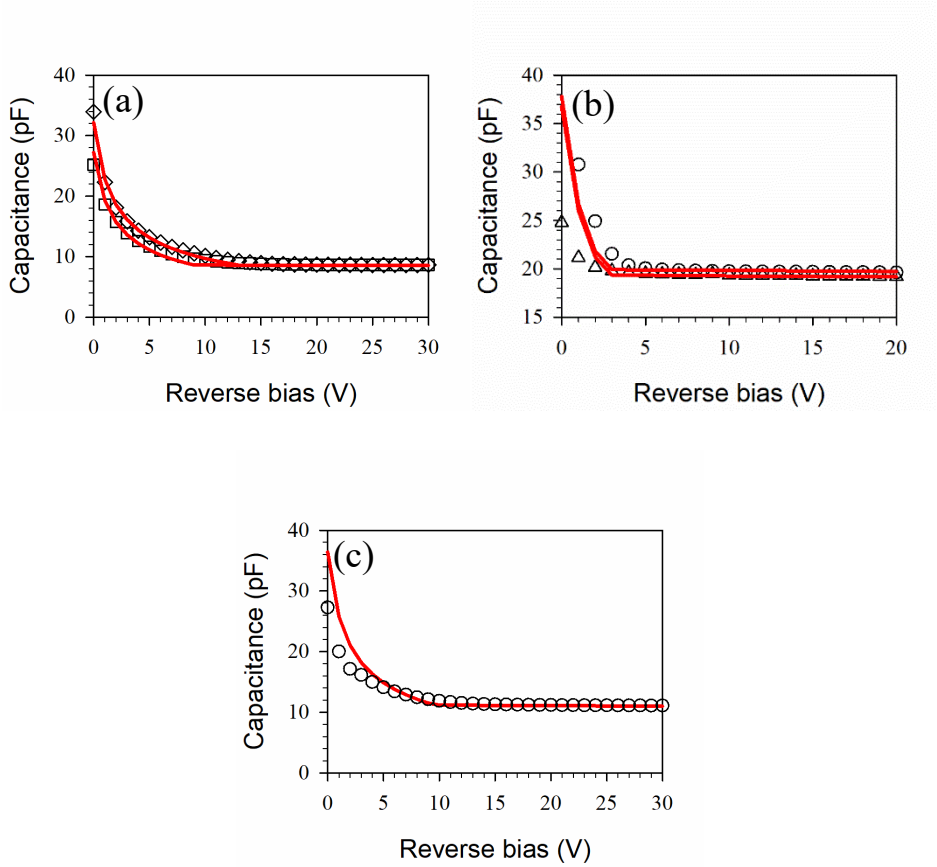

Figure 4.5. Typical room temperature C-V for 420 um diameter devices. (a) P1 (square) and N1 (diamond). (b) P2 (triangle) and N2 (circle). And (c) P3. Solid lines are modelled results by solving the Poisson's equation.

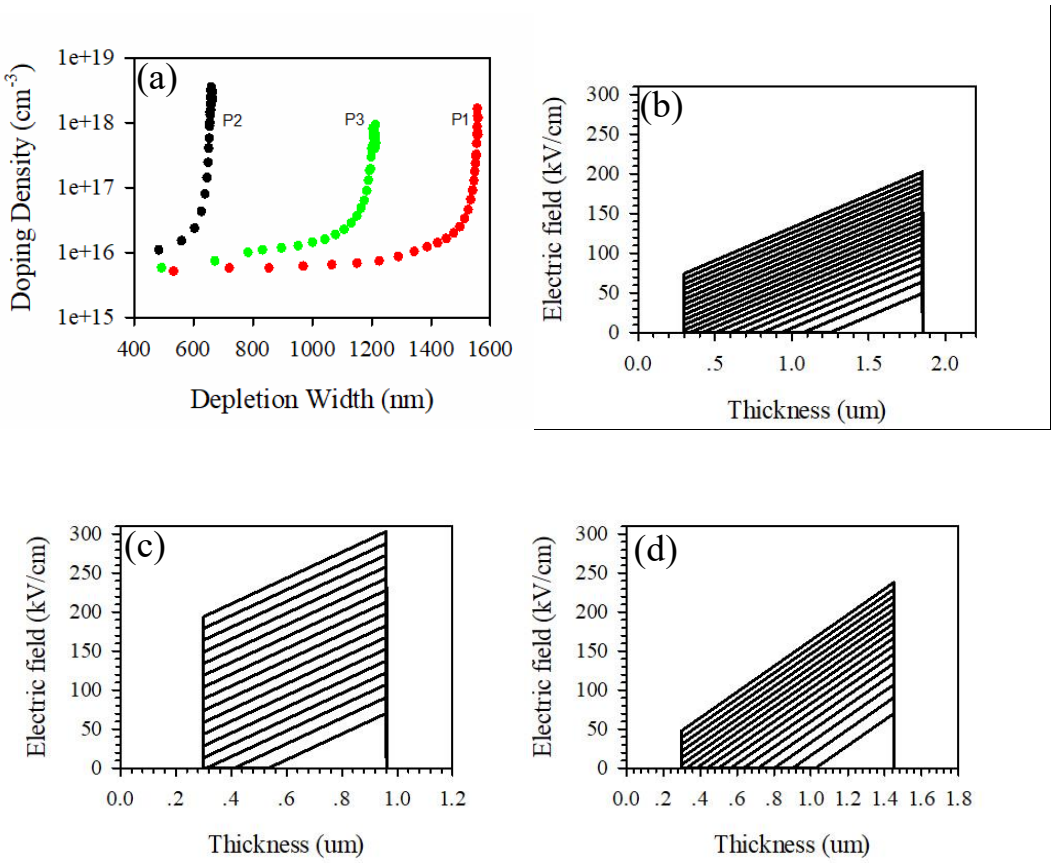

Figure 4.6. (a) Doping density against depletion width. It shows that the intrinsic region doping density for P2, P3 and P1 varies between $5 \times 10^{15} - 10 \times 10^{15}$ cm^{-3} as determined from the CV measurements. (b) Electric profile of P2. (c) Electric profile of P3. (d) Electric profile of P1. The reverse bias starts from 0 V in the step of 1 V.

Table 4.1. Device parameters of AlAsSb homjunction diodes.

Layer name	Diode type	Nominal i-thickness (μm)	Breakdown voltage V_{bd} (V)		CV Modelled results		Growth technique
			Measured	Modelled fit	i-region doping ($\times 10^{15}$ cm^{-3})	i-region thickness w (μm)	
P1	PIN	1.5	84.5	85.7	5	1.55	DA
N1	NIP	1.5	84.5	86.0	5	1.55	DA
P2	PIN	0.60	40.2	40.4	10	0.66	DA
N2	NIP	0.60	41.5	42.3	10	0.66	DA
P3	PIN	1.00	62.2	63.3	10	1.15	DA
P4	PIN	0.25	20.2	21.2	1	0.23	RA
P5	PIN	0.10	11.2	14.9	1	0.08	RA
P6	PIN	0.10					RA

4.3.2 Dark current measurement

Dark IV characteristics were measured from all layers. Figure 4.7(a) shows some examples of dark forward IV from P1. The surface dark current dominates between 0 and 0.7 V and after 0.7 V the bulk dark current dominates. The calculated current density is shown in Figure 4.7(b). At low forward bias, the dark currents scale with device perimeter suggesting the presence of large surface currents while at higher forward biases they scaled with area indicating its bulk current property. Fitting of the largest diameter diodes for the bulk current region shows the ideality factor of ~2 and low series resistance. A similar ideality factor and series resistance are extracted from the rest layers. The forward I-V measurements also show that the device has a low turn-on voltage

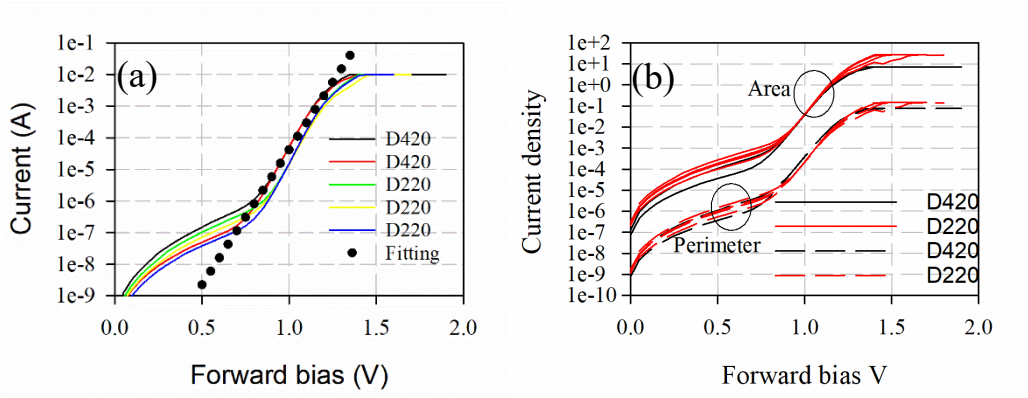

Figure 4.7. (a) Forward dark current on P1. (b) Calculated forward dark current per unit area and perimeter on P1. The units are A/cm^2 for Area and A/cm for perimeter.

The measurements for dark reverse IV are shown in Figure 4.8, with several different diameter diodes. From reverse dark IV measurements, breakdown in all layers was seen to be sharp and clearly defined. The high reverse dark currents seen here are not indicative of the bulk dark currents in this material system as they too appear to scale with perimeter instead of area. The comparison of forward and reverse dark currents of the five AlAsSb diodes as measured on 420 µm diameter mesa structure are shown in Figure 4.9 together with measured dark IV from P4 and P5 for 400 µm diameter devices. Compared with pure photomultiplication results (Figure 5.8 in Page 93), the multiplied dark current is not shown clearly in the measured dark current results. It suggests that the surface dark current is not multiplied and is dominant. For proving that the high dark current is mainly caused by surface leakage, we did IV measurement at low temperature, as shown in Figure 4.10. The reverse dark current is dramatically reduced as the temperature reduces, however, the surface dark current has no changes while reducing temperature (Equation 3.9). Our measured low temperature dark current is higher than the real low temperature bulk dark current. It suggests that the dark current could be further reduced by an optimized fabrication process and side passivation.

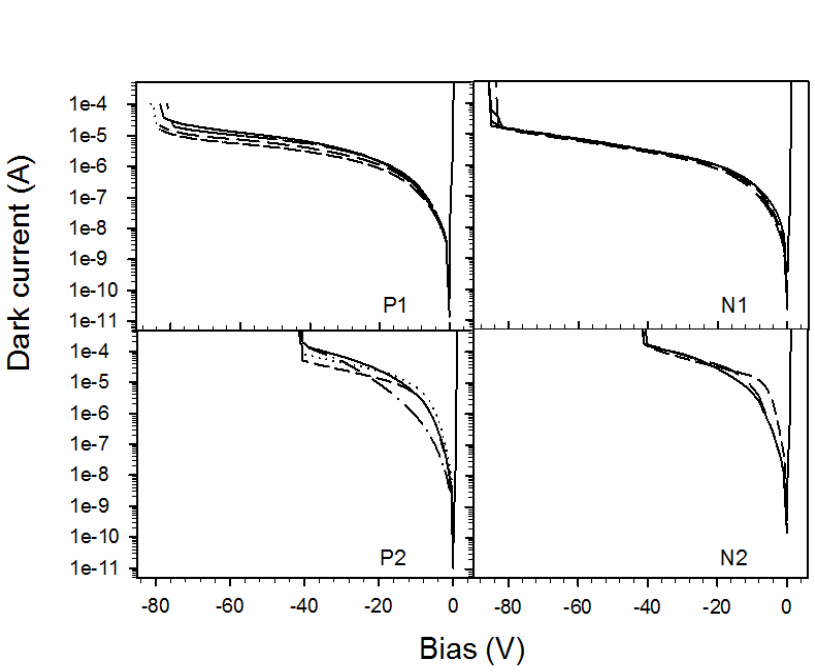

Figure 4.8. Dark current versus bias of P1, P2, N1 and N2. Different lines represent different diameter devices. It suggests devices have similar avalanche region.

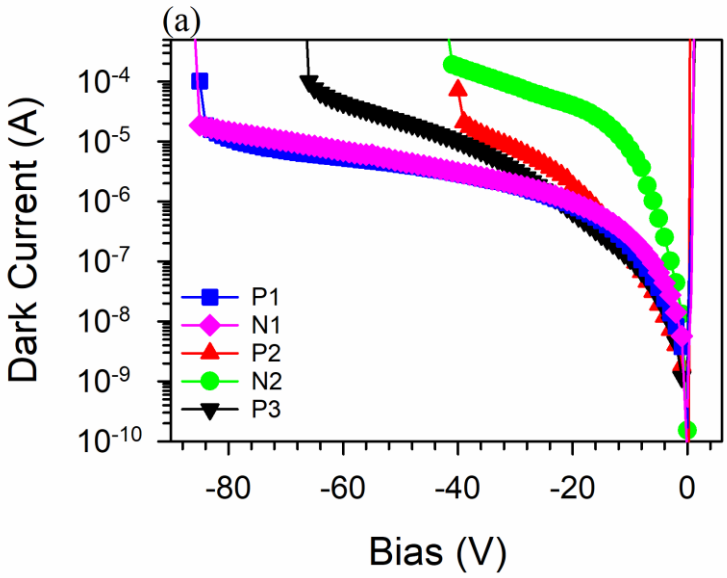

Figure 4.9. Typical room temperature I-V for 420 μm diameter devices. P1 (blue), P2 (red), P3 (black), N1 (pink) and N2 (green). Compared with room temperature IV for P4 (gray) and P5 (cyan) of 400 μm diameter.

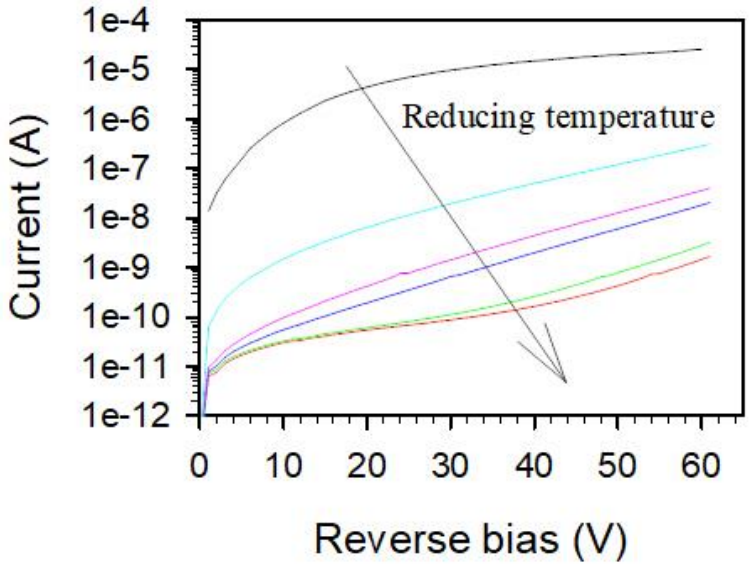

Figure 4.10. Dark IV of P3 at temperature 295-100 K with D = 420 μm.

The device dark current, I_d, is comprised of surface leakage current, I_s, and multiplied bulk dark current, I_b, which can be expressed by $I_d = I_s + M \times I_b$. The inset of Figure 4.11 shows an example of the measured I_d versus reverse bias at the light wavelength of 420 nm in P1. Table 4.2 lists the extracted I_{s1} and I_{b1} for the diodes with D = 220 μm from each wafer by looking at the dark current below 20 V. Because the total dark current can also be expressed as $I_d = A\pi D + B\pi D^2/4$, where A is the surface dark current per unit length, B is the bulk dark current per unit area, and D is the diameter of the APD, the I_{s2} and I_{b2} of the diodes with D = 30 μm (typical size for commercial high-speed detectors) from the three p-i-n wafers can be predicted by scaling the device area and perimeter respectively.

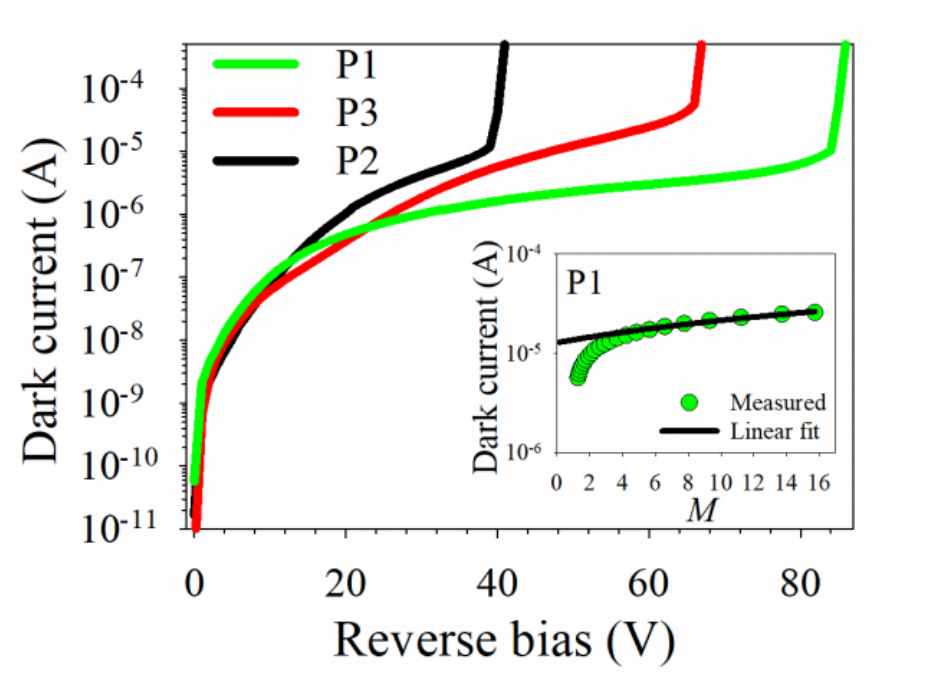

Figure 4.11. Dark current for devices with D = 220 µm for P1, P2 and P3 respectively. Inset shows the measured I_d versus M at 420 nm for P1 with D = 220 µm.

Table 4.2. Extracted I_s and I_b for P1 (600 µm p-i-n), P2 (1500 µm p-i-n) and P3 (1000 µm p-i-n).

	D = 220 µm		D = 30 µm	
	I_{b1} (A)	I_{s1} (A)	I_{b2} (A)	I_{s2} (A)
P2	1.2×10^{-8}	2.13×10^{-6}	2.23×10^{-10}	2.91×10^{-7}
P3	8.6×10^{-7}	1.28×10^{-5}	1.6×10^{-8}	1.75×10^{-6}
P1	1.27×10^{-7}	3.4×10^{-6}	2.4×10^{-9}	4.64×10^{-7}

4.4 Photo-response measurements in AlAsSb

4.4.1 Bias-dependent spectral response

A 100 W tungsten bulb and a grating monochromator was used to measure the photo spectral response of the 420 µm device by applying a low reverse bias until fully depleted for each layer. The measured spectral response (uncorrected for the system response) of P2 and N2 with increasing reverse bias from 0-8 V is presented in Figure 4.12. The very low photocurrent around the cut-off wavelength could still be measured by the phase sensitive technique, where the light signal was mechanically modulated

at ~185 Hz, and the photocurrent was measured by a LIA. The measurement technique was fully discussed in Chapter 3. Figure 4.13 shows the measured photocurrent versus reverse bias for P2 and N2 under different wavelength illumination. The photocurrent at shorter wavelengths (< 450 nm) in the p-i-n structure initially increases more rapidly between 0-8 V than in the case of the n-i-p, where the photocurrent appears to be constant over this range. Similar behaviour was observed in the other layers, depending on whether it is a p-i-n or n-i-p.

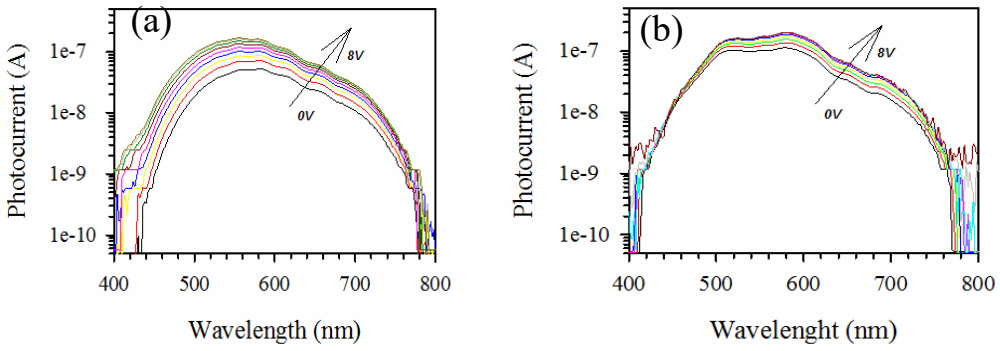

Figure 4.12. Bias-dependence spectral response of (a) P2 and (b) N2 from 0V to 8V at the step of 1V.

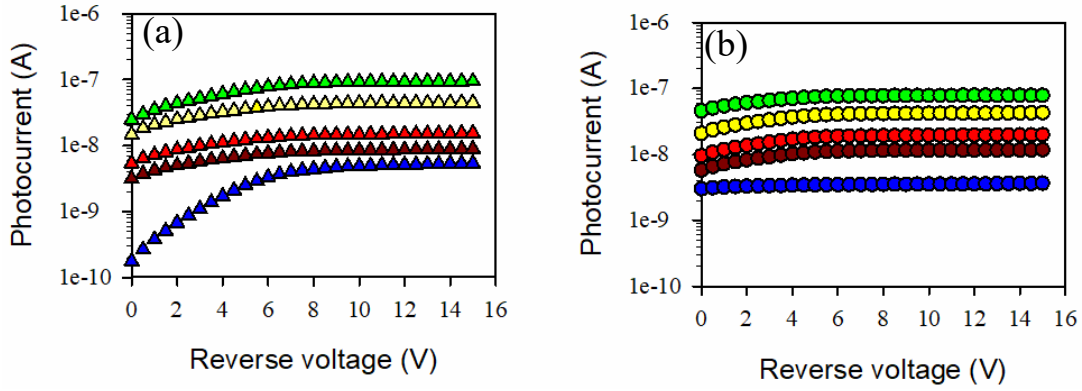

Figure 4.13. Photocurrent versus reverse voltage of (a) P2 and (b) N2 for the wavelength of 442 nm (blue), 542 nm (green), 633 nm (yellow), 700 nm (red) and 720 nm (dark red).

The reason for this is voltage-dependent responsivity at lower reverse bias. Initially, electrons are generated in the p+ layer under shorter wavelength illumination and diffuse from left to right. As the depletion edge moves closer to the surface, the carrier

collection efficiency increases qualitatively as shown in Figure 4.14 for a p-i-n structure. However, the carrier collection efficiency does not change when illuminated by longer wavelength light as carriers are generated uniformly in the i-region. From this, we can determine that the background doping in the i-region is p-type. CV measurements also confirmed the depletion width. After 8 V, the i-region is fully depleted as shown in Figure 4.5 for P2 and N2.

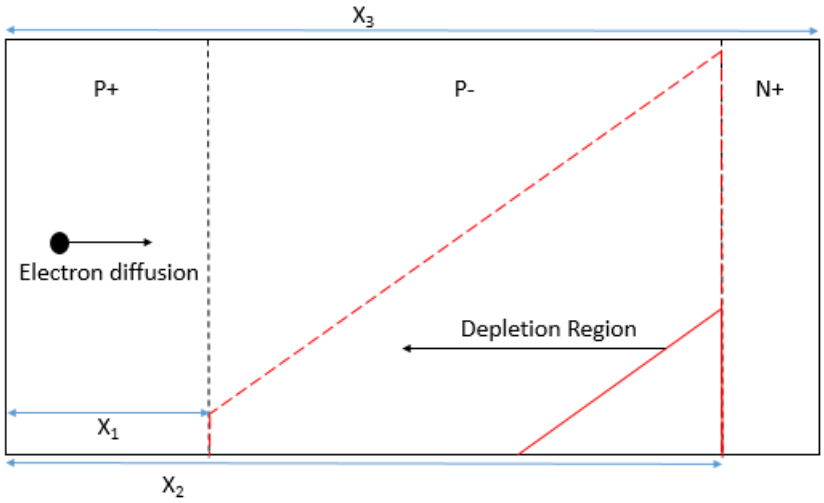

Figure 4.14. Illustration of the mechanizm for the initial photocurrent increase. Red lines are different electric profile at different reverse bias. The depletion edge is moving from the bottom to the top.

The change in quantum efficiency under illumination of 405 nm as a function of reverse bias before the onset of multiplication was used to calculate L_e and L_h. (equation 2.6 – 2.8) We linearly interpolate between the absorption coefficients of AlAs and AlSb to obtain values of 2.0×10^5 cm^{-1} at 405 nm for AlAsSb. More information can be found in Ref. [15]. It was found that approximately 99.99% of the light was absorbed in the top InGaAs and AlAsSb cladding layer under the illumination of 405 nm light. There is a large conduction band offset between InGaAs and AlAsSb which blocks carriers generated in the top InGaAs layer. Therefore the photocurrent contribution is only from carriers generated in the top AlAsSb cap layer. As discussed before, the increase in quantum efficiency with illumination of 405 nm light with applied reverse bias is due to the moving of the depletion edge, enabling us to estimate the L_e and L_h based on Equation (2.6) and (2.7).

4.4.2 Quantum efficient and absorption coefficient

The spectral quantum efficiencies, η, were then determined using a commercial silicon PIN photodiode (Hamamatsu PD S5973-02 [16]) to calibrate the optical system. This Si photodetector has a similar active area to the largest diameter AlAsSb devices, and has a near-unity responsivity from 400 to 600 nm. The surface reflectivity, R as a function of wavelength used InGaAs parameters [10]. Quantum efficiency was also corroborated at 633 nm using a focussed He-Ne laser spot. Figure 4.15 shows the measured quantum efficiency for five different structures when fully depleted. Compared with N1 (N2), P1 (P2) shows better efficiency at the shorter wavelengths (wavelengths shorter than the peak absorption wavelength). This suggests $L_e > L_h$ in this material as more contribution of electron minority carriers. While a similar avalanche region width gives us similar quantum efficiency, a thicker avalanche region gives us higher quantum efficiency at the longer wavelengths (wavelengths longer than the peak absorption wavelength). It is because that the avalanche layer of width w starts to dominate photon absorption and carrier generation and to contribute to drift current. The cut-off of all layers is found about ~ 780 nm (E_g ~ 1.57 eV).

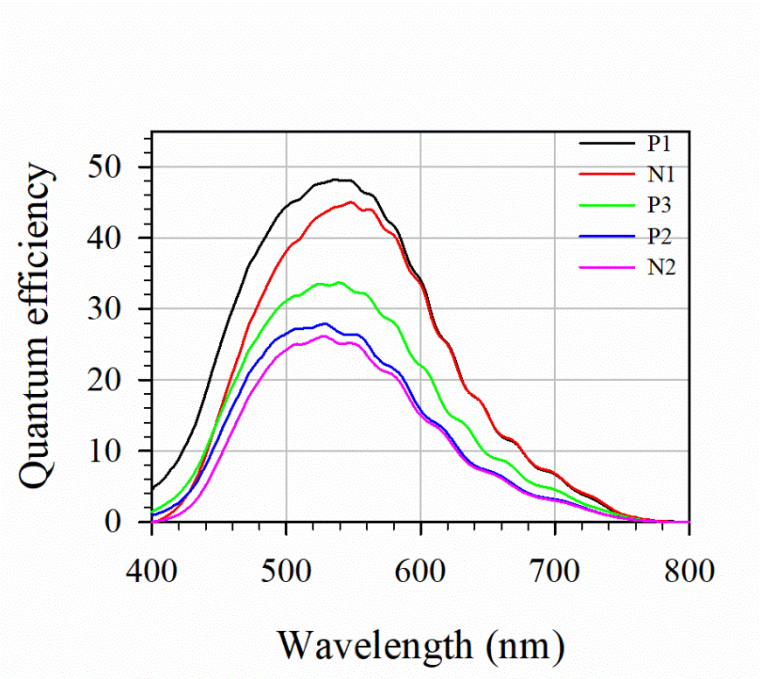

Figure 4.15. Measured quantum efficiency for five different layer structures at fully depleted bias. P1 and N1 are at 20 V, P2 and N2 are at 8 V, and P3 is at 18 V.

The absorption coefficient, γ, of AlAsSb as a function of wavelength were extracted from bias-dependent spectral response results of P1-P3 and N1-N2 by used Equation (2.6) - (2.10). Absorption coefficients are shown graphically in Figure 4.16. These coefficients are able to reproduce the measured bias-dependent quantum efficiency, as shown in Figure 4.17. The simulated results are in close agreement to measurements over three orders of magnitude. The parameters used in the simulation are L_e (L_h) of 0.07 μm (0.03 μm), μ_e (μ_h) of 160 cm/s (10 cm/s) and S_e (S_h) of 10^7 cm/s (10^7 cm/s). The predict absorption coefficients are independent of the doping type.

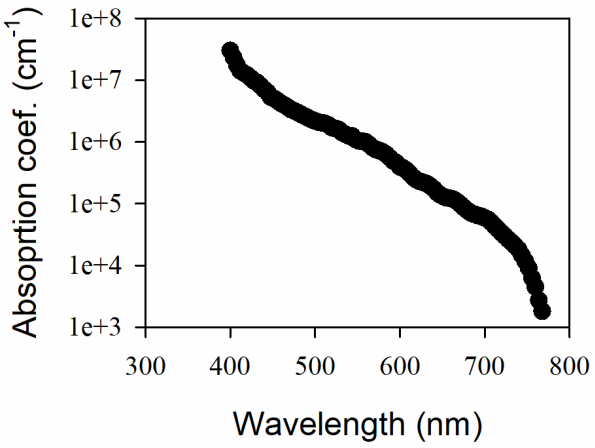

Figure 4.16. Absorption coefficient obtained from P1-P3 and N1-N2.

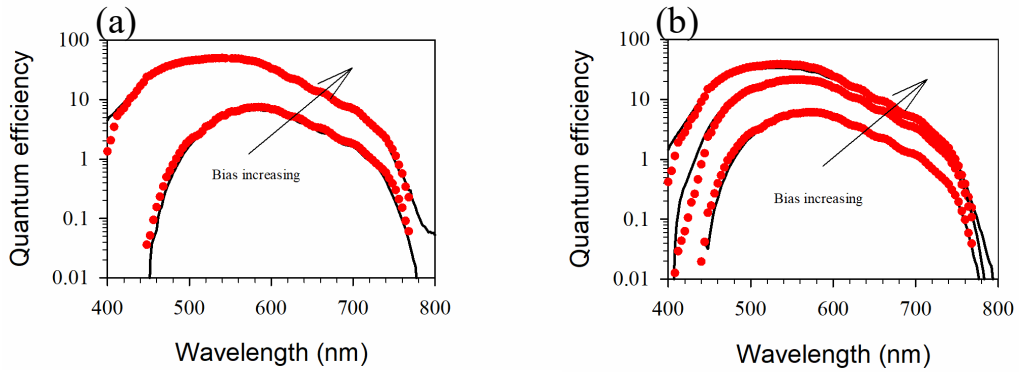

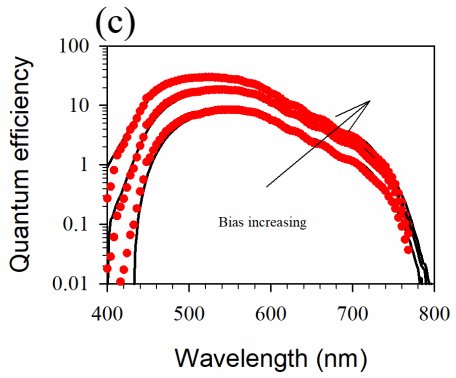

Figure 4.17. Measured bias-dependence η (lines) and simulated η (red symbols) from (a) P1 at 0 and 20 V, (b) P3 at 0, 10 and 18 V, and (c) P2 at 0, 3 and 8 V.

4.4.3 Bandgap estimation

To extract the band energy of AlAsSb, $\gamma^{0.5}$and γ^2 versus photon energy is plotted. A red straight line can go through the calculated $\gamma^{0.5}$and γ^2 respectively, band energy was determined by extrapolating the straight line to the horizontal intercepts (More background theory is discussed in the Chapter 2). AlAsSb grown lattice-matched to InP substrate is an indirect bandgap material. The value of E_g (band energy of the X-valley) is found to be ~1.57 eV corresponding to Figure 4.18(a) and the value of the direct gap is found to be ~2.2 eV as shown in Figure 4.18(b). The simplest band energy graph is shown in Figure 4.19. These values are comparable to those obtained from Ref. [17, 18].

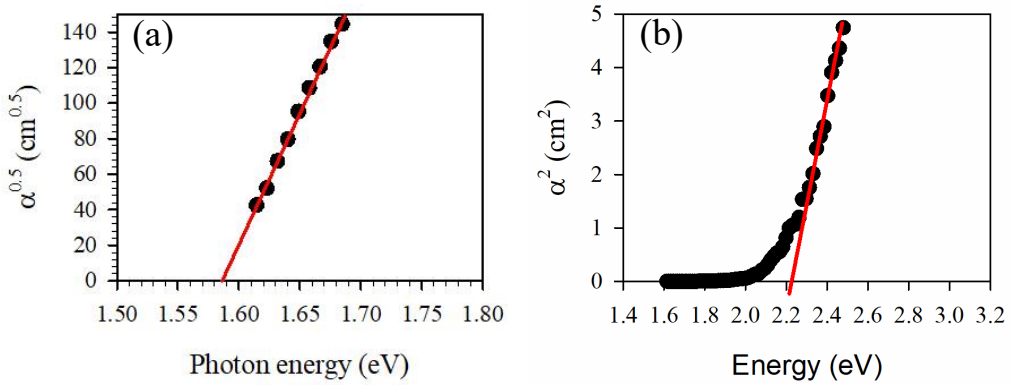

Figure 4.18. Extracting the direct and indirect bandgap.

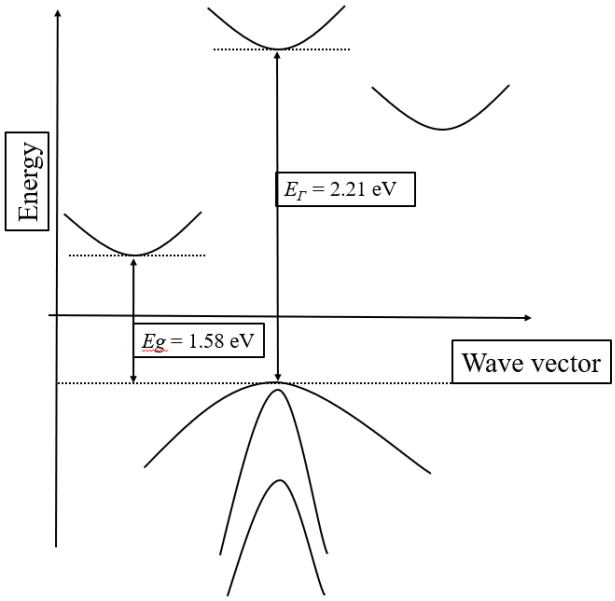

Figure 4.19. Band diagram of AlAsSb lattice match to InP.

4.4.4 Light intensity versus distance

Figure 4.20 shows the light intensity within the intrinsic region of 0.66 - 1.55 μm for the three different wavelengths used based on the absorption coefficients and Equation 2.2. The light enters the top of the cladding layer of AlAsSb at x = 0 nm and the light start to absorb in the avalanche layer from x = 300 nm. The three grey lines show the intensity at the end of the three avalanche regions considered. The 420 nm gets almost fully absorbed in the top doped cladding region giving rise to single carrier initiated multiplication. The longer wavelengths, however, create carriers within the intrinsic region resulting in both electrons and holes initiating the multiplication. This information is useful for determining the injection of carriers discussed in the next chapter.

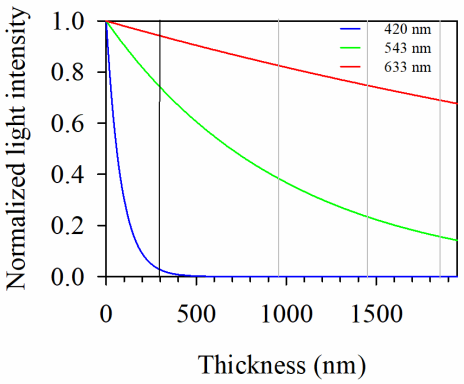

Figure 4.20. Modelled light intensity versus distance for 420 nm (1.2×10^5 cm^{-1}), 543 nm (1×10^4 cm^{-1}) and 633 nm (2×10^3 cm^{-1}).

4.4.5 Spectral response comparison of digital alloy and random alloy growth

The spectral response characteristics of digital alloy AlAsSb is compared with those of RA AlAsSb, as shown in Figure 4.21. It suggests that P4 and P5 show similar spectral response at shorter wavelengths and all AlAsSb layers give a comparable cut-off wavelength. The lower response of P6 at shorter wavelengths is explained by a thicker InGaAs cap of 100 nm. As expected, AlAsSb by DA technique can absorb at wavelengths beyond the cut-off by the RA technique while lattice-matched to InP substrate. This was observed in ref [19]. In Ref. [20], Juang B. et al. reported the optical characteristics of the AlAsSb grown lattice-matched to GaSb substrates using DA and RA growth technique by MBE, and suggested that DA could offer a more compositionally uniform III-(As, Sb) alloy with enhanced optical quality. We believe that wafers used in this work have a similar band structure, optical and electronic properties. Interestingly, the spectral response results in the DA samples with much thicker avalanche region show oscillations at longer wavelength due to Fabry Perot effect.

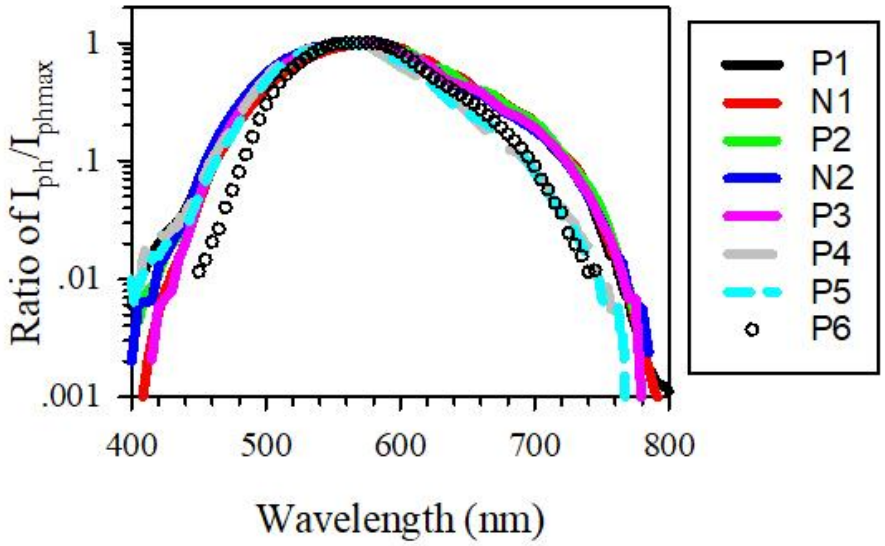

Figure 4.21. Spectral response of structure by digital alloy growth technique (solid lines), by random alloy growth technique (dashed lines and symbols). Dashed lines present P4 and P5 and symbols present P6.

4.5 Conclusions

A detail and systematic investigation of the photocurrent at low reverse bias was performed on 3 p-i-n and 2 n-i-p structures grown lattice-matched to InP substrates using the DA growth technique by MBE. The IV measurement provides fundamental information of PDs, and the CV measurement provides an accurate electric-field profile. The absorption coefficient in AlAsSb as a function of wavelength was extracted from the measured bias-dependent spectral response. The direct and indirect band energy in AlAsSb was determined used the calculated absorption coefficients. Finally, our digital alloy AlAsSb is comparable with random alloy material based on the spectral response.

4.6 References

[1] J. Feng, R. Akimoto, S. Gozu, T. Mozume, T. Hasama and H. Ishikawa, “Ultrafast all-optical switch with cross-phase modulation by area-selective ion implantation in InGaAs/AlAsSb couled double quantum wells,” Opt. Exp., Vol. 20, no. 26, pp. B279-B287, Nov. 2012.

[2] D.G. Revin, L.R. Wilson, E.A. Zibik, R.P. Green, J.W. Cockburn, M.J. Steer, R.J. Airey and M.Hopkinson, “InGaAs-AlAsSb quantum cascade lasers emitting at 4.4 um,” Appl. Phys. Lett., vol. 85, no. 18, pp. 3992-3994, Nov. 2004.

[3] D.O.T. Filho, I.F.L. Dias, J.L. Duarte, E. Laureto and J.C. Harmand, “Optical and electrical properties of Te Doped AlGaAsSb/AlAsSb bragg mirrors on InP,” Brazilian Journal of Physics, vol. 36, no. 4A, Dec. 2006.

[4] Y. Gu, J. Yan, M. Raj, Fow-Sen Choa, G. V. Jagannathan, Sudhir B. Trivedi, and J. Feng "High-efficiency InP-based multijunction solar cells", Proc. SPIE 5260, Applications of Photonic Technology 6, Dec. 2003.

[5] S.Y. Xie, X.X Zhou, S.Y. Zhang, D.J. Thomson, X. Chen, G.T. Reed, J.S. NG and C.H. Tan, “InGaAs/AlGaAsSb avalanche photodiode with high gain-bandwidth product” Opt. Exp., Vol. 24, No. 21, pp. 24242-24247, 2016.

[6] J. Xie, S. Xie, R. C. Tozer and C.H.Tan. "Excess Noise Characterization of AlAsSb Avalanche Photodiodes" IEEE Trans. Electron. Devices. Vol.59, no.6. May 2012.

[7] I.C. Sandall, S. Xie, J. Xie and C.H. Tan, “High temperature and wavelength dependence of avalanche gain of AlAsSb avalanche photodiodes,” Opt. Lett., Vol. 36, No. 21, pp. 4287-4289, Nov. 2011.

[8] G.B. Stringfellow, “Miscibility gaps in quaternary III/V alloys,” J. Cryst. Growth, vol. 58, pp. 194–202, 1982.

[9] C.A. Wang, “Progress and continuing challenges in GaSb-based III–V alloys and heterostructures grown by organometallic vapor-phase epitaxy,” J. Cryst. Growth, vol. 272, pp. 664–681, 2004.

[10] Ioffe Institue web, http://www.ioffe.ru/SVA/NSM/Semicond/GaInAs/optic.html

[10] Y.H. Zhang, “Accurate control of As and Sb incorporation ratio during solid-source molecular-beam epitaxy,” J. Cryst. Growth, vol. 150, pp. 838–843, 1995.

[11] Y. Yuan, J. Zhang, A. K. Rockwell, S.D.March, S.R. Bank and J.C. Campbell, “AlInAsSb Impact ionization coefficients,” IEEE Photo. Tech. Lett., vol. 31, no. 4, Feb. 2019.

[12] M. E. Woodson, M. Ren, S.J. Maddox, Y. Chen, S. Bank abd J.C. Campbell, “Low-noise AlInAsSb avalanche photodiode,” Appl. Phys. Lett., vol. 108, no. 081102, Feb. 2016.

[13] O. Blum, M. J. Hafich, J. F. Klem, K. Baucom and A. Allerman, Wet thermal oxidation of AlAsSb against As/Sb ratio. Electron Lett. Lett., vol. 33, no. 12: pp. 1097 1099. Jun. 1997.

[14] S. Y. Kim, J. D. Song, T. W. Kim, Effect of InAs Thickness on the Structural and the Elect rical Properties of InAs Layers Grown on GaAs Substrates with an AlAs 0.32 Sb 0.68 Buffer Layer J. Korean Phys. Soc ., vol. 58, no. 6: pp. 1347 1350 2011.

[15] J.J. Xie, “Characterisation of low noise InGaAs/AlAsSb avalanche photodidoes,”PhD Thesis, University of Sheffield, UK, 2013.

[16] "High speed photodiodes (S5973 series: 1 GHz)," Hamamatsu Photonics K. K.1 Sept 2015 2012.

[17] X. Zhou, J.P.R. David, J.S. Ng and C.H. Tan, “Avalanche breakdown characteristics of AlGaAsSb quaternary alloys,” IEEE Photo. Thech. Lett., vol. 28, no. 22, Nov. 2016.

[18] Y. Kawamura, H. Kumsu, K. Yshimatsu, A. Kamada, Y. Naito and N. Inoue, “InAlAs/ AlAsSb Type II Multiple Quantum Well Layers Lattice-Matched to InP Grown by Molecular Beam Epitaxy,” Jpn. J. Appl. Phys, vol. 36, no. 6B, pp. L757-L760, Jun. 1997.

[19] Bulman, G.E., Zipperian, T.E. & Dawson, L.R. The determination of impact ionizations in $In_{0.2}Ga_{0.8}As$/GaAs strained-layer superlattice mesa photodiodes. Journal of electronic materials. 15, 221-227 (1986).

[20] B. Juang, B. Liang, D. Ren, D.L. Prout, A.F. Chatziioannou and D.L. Huffaker, “Optical characterization of AlAsSb digital alloy and random alloy on GaSb,” Crystals, vol. 7, no. 313, Oct. 2017.

CHAPTER 5:
AVALANCHE MULTIPLICAITON AND IMPACT IONIZATION IN AlAsSb DIODES AT ROOM TEMPERATURE

5.1 Introduction

The multiplication material InP or AlInAs latticed-matched to InP substrates is used in most commercial telecommunication-wavelength APDs utilizing InGaAs as the absorption region. At present, such SAM-APDs have successfully demonstrated 5-10 dB better sensitivity compared to receivers used PDs. However, these multiplication materials cannot provide us with the ideal combination of low dark current at room temperature, a very disparate ionization coefficient ratio and low excess noise because of their fundamental physics property. AlAsSb can be grown lattice-matched to InP substrates with a relatively wide indirect band-gap of ~1.6 eV, and no observed tunnelling current at high electric fields. Xie J.J. et al. has reported very low excess noise results, k~0.05, in submicron p-i-n AlAsSb diodes and more recently very low excess noise results were also found in submicron p-i-n $Al_xGa_{1-x}AsSb$ (x = 0.95 – 0.85) [1-3]. However, such excess noise characteristics are strongly linked to the well-known "dead space" effect [4]. So far, the impact ionization process in bulk AlAsSb has not been investigated and this can usefully determine devices' breakdown voltage, avalanche multiplication and avalanche excess noise.

This chapter reports a systematic study of multiplication carried out on a series of AlAsSb p-i-n/n-i-p diodes at room temperature. The nominal intrinsic layer thickness ranges from 0.6 μm to 1.5 μm. The study can be achieved through photo-multiplication measurements, as discussed in Chapter 3. Based on measurements of multiplication initiated by electrons or holes, the ionization coefficients of AlAsSb were deduced using the local theory assumption taking into consideration any tapered electric-filed. The bulk electron and hole impact ionization coefficients have been determined over an electric-field range from 220-1250 kV/cm for α and from 360-1250 kV/cm for β for

the first time.

5.2 Preliminary photomultiplication characteristics

In the previous chapter, we showed a bias-dependent photo spectrum response under low reverse bias. In this section, we demonstrate the spectrum response under high reverse bias.

The photo-response measurement was performed on 420 μm diameter devices by applying a high reverse bias until impact ionization occurs for each structure. Figure 5.1 shows the measured spectral response on P2 and N2. The red symbols show the the ratio of photocurrent between -35 V and -8 V. The increase of photocurrent at a low bias (from 0 V to -8 V) demonstrates the moving depletion width as discussed in Chapter 4. The photocurrent at shorter wavelengths in the p-i-n structure increases more rapidly with bias compared to the longer wavelength. The opposite behaviour is seen in the n-i-p structure with the longer wavelengths showing a rapid increase in the photocurrent with bias compared to the shorter wavelengths. Similar behaviour was observed in the other layers, depending on whether it is a p-i-n or n-i-p. The comparison of photocurrent under illumination by different wavelengths shows in Figure 5.2. The photocurrent at -8 V was chosen as the unity gain point of these two devices due to be full depletion at this bias observed from CV results. We did not increase to very high gain (near breakdown voltage) due to protecting the device at this initial stage. It is seen that multiplication reduces with longer wavelength illumination in a p-i-n structure and the multiplication increases with longer wavelength illumination in n-i-p structure. This shows us that $\alpha > \beta$ in this material. Devices were also measured under LED illumination as shown in Figure 5.3, together with the results obtained from the spectral response. The result with 430 nm is surprisingly even lower than it with 442 nm, and the results using 680 nm is similar to those using 633 nm and 720 nm. It suggests that the holes hardly undergo ionization, and we have to use a shorter wavelength to achieve pure carrier injection condition in future work.

So far, the preliminary multiplication results were obtained by photo spectral measurements using a tungsten bulb or LEDs, with the uncertainty of a big spot of the light source, no power dependence of multiplication and no size dependence of multiplication. Here, we have only demonstrated $\alpha > \beta$ and wavelength sensitivity in AlAsSb diodes, therefore, a systematic multiplication investigation is required.

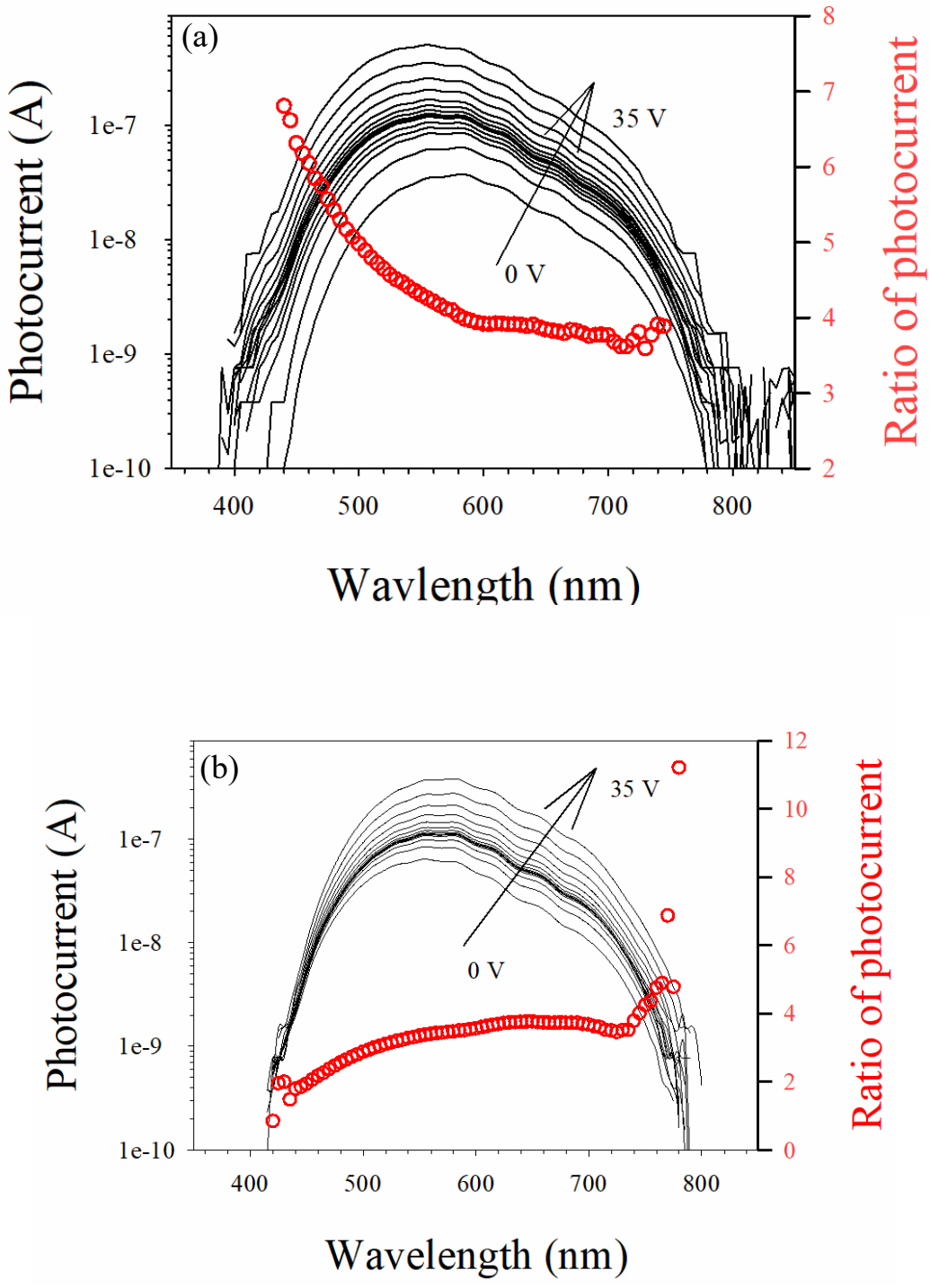

Figure 5.1. (a) Bias-dependence spectral response of P2. (b) Bias-dependence spectral response of N2. Red symbols are the ratio of photocurrent at 35 V and 8 V.

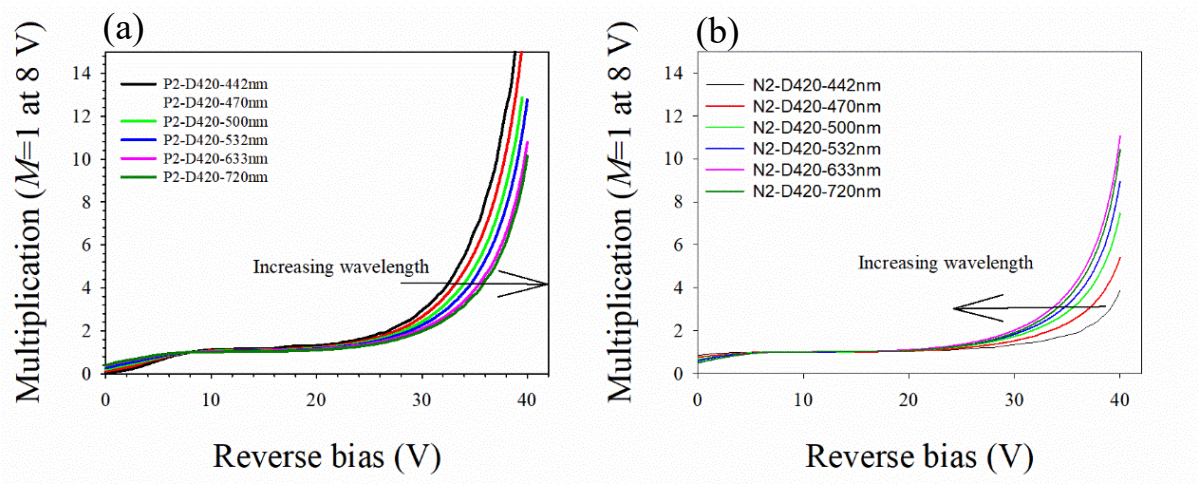

Figure 5.2. (a) Preliminary multiplication of P2. (b) Preliminary multiplication of N2

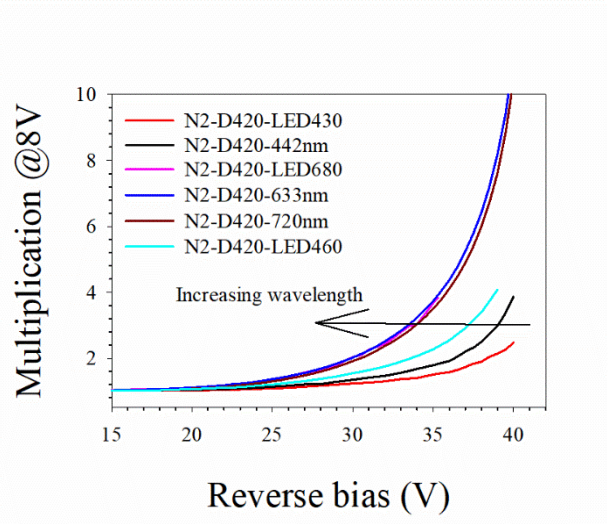

Figure 5.3. Preliminary multiplication of N2 using different LED sources.

5.3 Photomultiplication characteristics

The photomultiplication measurement technique was fully described in Chapter 3. The absorption profile was shown in Figure 4.20. Two different wavelength light sources (405-nm and 633-nm wavelength) were used on all layers in this chapter. A lock-in amplifier was used for all measurements of photocurrent due to the relatively high surface dark currents. Photocurrent measurements were undertaken on several devices with different diameter for each structure at different laser powers to ensure the repeatability of results. Figure 5.4 shows examples of measured photocurrent on different

layers under illuminations of 405-nm/633-nm wavelength light. The magnitude of photocurrent was mainly dependent on the power of laser source and the absorption coefficient of the wavelength. Comparing similar intrinsic thickness, the shape of photocurrent with 405 nm wavelength illumination is different, with the onset of multiplication earlier on the p-i-n structure, and this difference is more obvious in the P1-N1 pair due to the much thicker i-region. However, the shape is comparable in both structures when under 633-nm wavelength illumination.

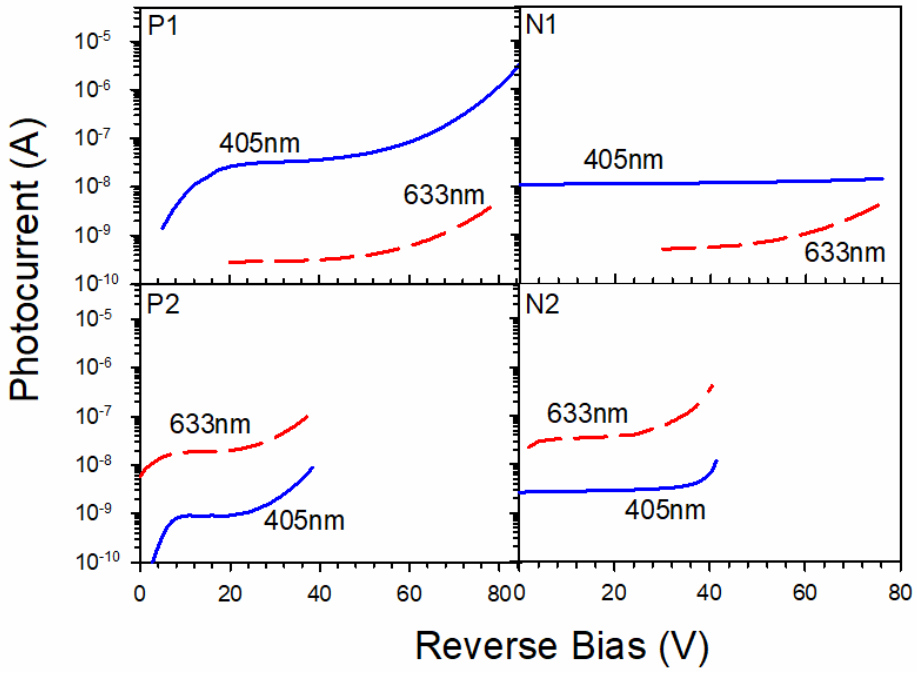

Figure 5.4. The photocurrent versus reverse bias using 405-nm and 633-nm laser illumination.

The multiplication in these structures was determined by looking at the increase in photocurrent once the intrinsic layer was fully depleted and correcting for any increase in the primary photocurrent due to small movement of the depletion edges in the heavily doped cladding regions [5]. The solid red line in Figure 5.5 demonstrates the baseline for this case, which we define as the primary current. Multiplication was obtained by calculating the ratio of the total photocurrent (open circle) to the primary current (red line).

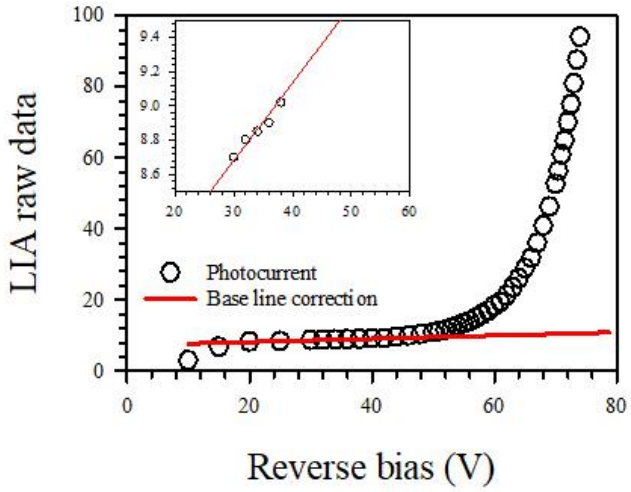

Figure 5.5. An example of baseline correction.

5.3.1 Avalanche multiplication in p-i-n diodes

Using p-i-n structure with suitable topside wavelength illumination, can give us pure or mixed multiplication characteristics. Figure 4.20 shows an absorption profile for wavelengths of 405 nm and 633 nm. Since the absorption coefficient of AlAsSb at 633 nm wavelength is low, this light is weakly absorbed and would generate photocarriers throughout the diode. Therefore, avalanche multiplication in the diodes illuminated by 633 nm light is initiated by a mixture of carriers comprising electrons diffusing from the p cladding layer, electron-hole pairs generated in the high electric-field and holes diffusing from the n cladding layer. As the illumination wavelength decreases, more light is absorbed closer to the surface. At a wavelength of 405 nm, more than 99.9% of the light intensity is absorbed in the top cladding layer. A comparison of measurements made on different radii device or with different laser powers show constant multiplication results, as shown in Figure 5.6. It suggests that photomultiplication values are independent of the intensity of light and diameter of the device. The maximum intensity of light used is usually 100 times higher than the minimum. Furthermore, we also confirmed multiplication uniformity by measured with the light illuminating different parts of the optical access window of a DUT.

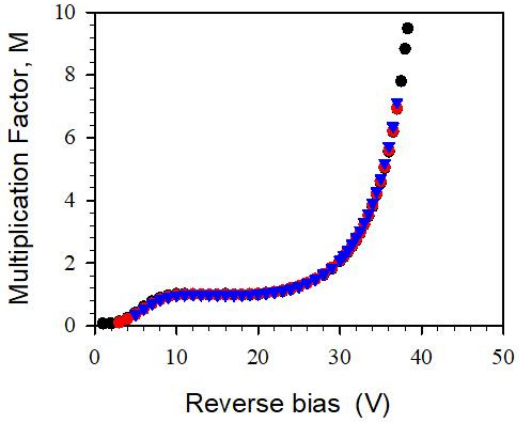

Figure 5.6. Photomultiplication measured on P2 diodes of different diameters and powers at a wavelength of 405 nm. The diameter of DUT is 220 μm with laser power of A (black circle), 420 μm with laser power A (red circle), 420 μm with laser power B (blue triangle). Power A is about ten times higher than power B.

It is found that the M_e achieved under 405-nm laser illumination is higher than M_{mix} under 633-nm laser illumination, as shown in Figure 5.7. The highest multiplication value of P2 was limited by high dark current and edge breakdown. Other p-i-n structures demonstrated the same wavelength dependence, but the difference between pure and mixed injection reduces on P4 and P5. This is because the α/β ratio is similar at the high electric-field.

The typical multiplication characteristics under pure injection condition of P1-P3 are summarized in Figure 5.8, plotted on a log scale, and compared together with the simulation of single carrier multiplication ($\beta = 0$) under similar avalanche structure as shown by the dashed line. The shape of the curves suggest that the onset of multiplication occurs well before the breakdown voltage is expected when $\alpha >> \beta$.

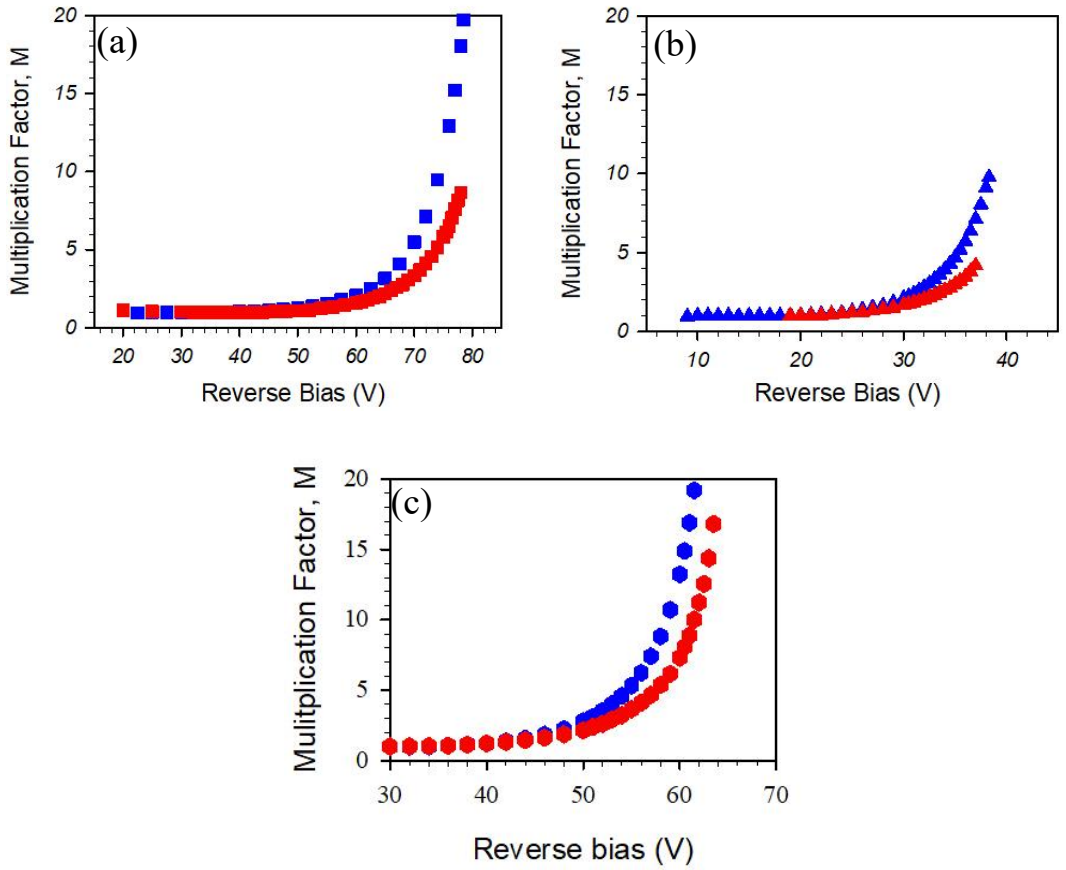

Figure 5.7. Photomultiplicaiton measured on (a) P1, (b) P2 and (c) P3. The colour blue presents the illumination of the 405-nm wavelength (M_e), and the colour red shows the illumination of the 633-nm wavelength (M_{mix}).

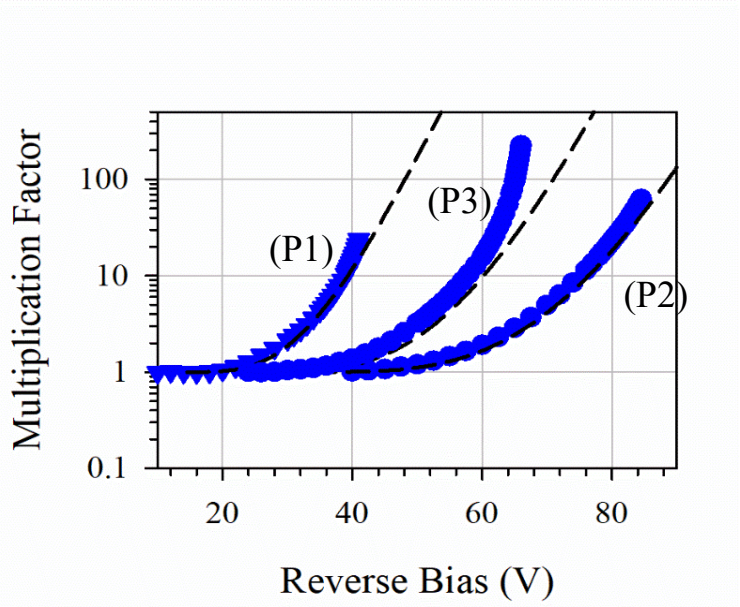

Figure 5.8. A comparison of M_e measured on P1-P3 with the simulation of similar p-i-n structure with β of 0. Symbols are measured M_e and dashed lines are the theoretical values β of 0.

5.3.2 Avalanche multiplication in n-i-p diodes

Photomultiplication measurements were also performed on two n-i-p diodes using the same wavelength (405 nm and 633 nm), powers and device diameters to assess the accuracy and constancy of the results. It suggests that the multiplication by mixed injection is higher than those of the pure hole injection, as shown in Figure 5.9. This agrees with the conclusion above that $\alpha > \beta$ in this material because $M_{mix} > M_h$ in the n-i-p structures. Note that the thickest layer (N1) is hardly ionizing even near the breakdown voltage under pure hole injection condition. It strongly supports the view that impact ionization coefficients of hole are extremely low at low electric-field and $\alpha >> \beta$ in this material. Appreciable differences between the multiplications characteristic resulting from two wavelengths in n-i-p and in p-i-n configuration were observed.

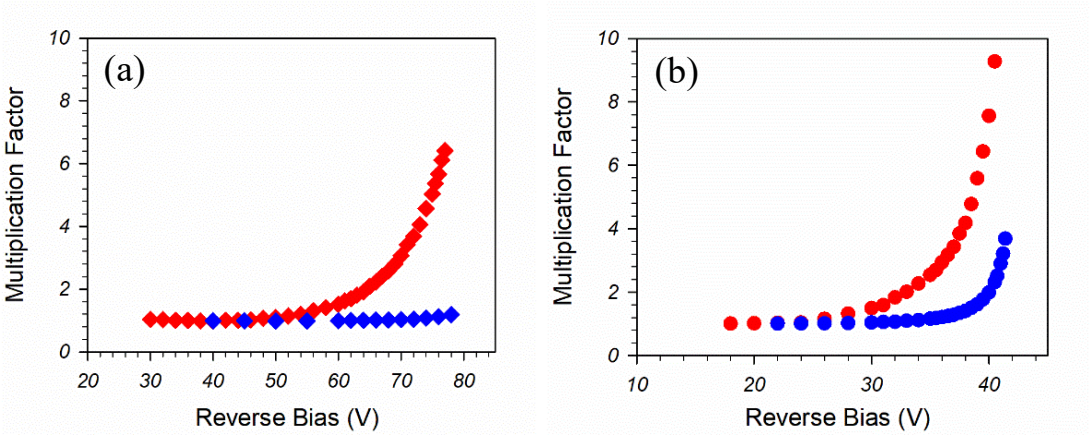

Figure 5.9. Photomultiplication measured on (a) N1 and (b) N2. Colour Blue presents the illumination of 405 nm (M_h) and colour red shows the illumination of 633 nm (M_{mix}).

5.3.3 Multiplication on P4 and P5

To cover a wide electric field range, two thin structures were also investigated. Researchers at Sheffield published the photo spectral response, the wavelength dependence of multiplication and the wavelength dependence of excess noise [1] on two layers before, named P4 and P5 in this thesis. These measurements were repeated, and Figure 5.10 shows a comparison of the wavelength dependence of multiplication. It suggests that our multiplication results under the 405 nm wavelength are slightly higher than their results due to the fact that the light is more strongly absorbed in the top cladding layer, and our multiplication results using 633 nm light are similar to their results.

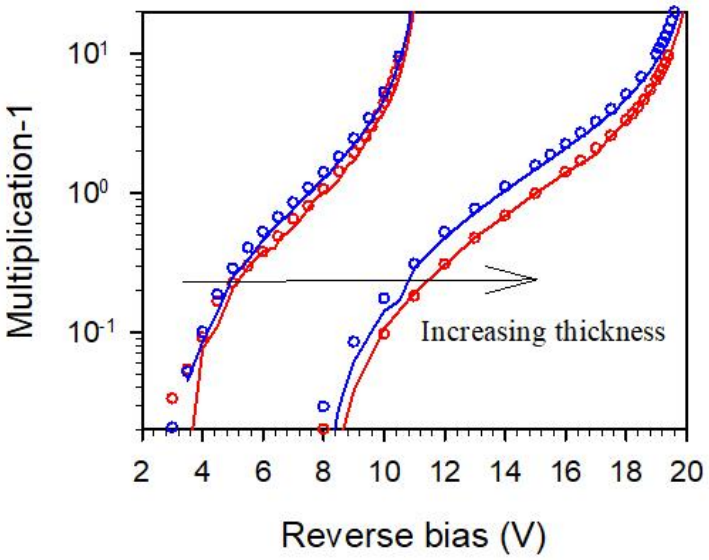

Figure 5.10. Multiplication of P4 and P5 used 405/442 nm and 633 nm light. Symbols present the repeated results while the lines are published results by Xie J.J. et al. I used 405 nm and 633 nm wavelength light, and in Ref. [1] they used 442 nm and 633 nm wavelength light.

5.3.4 Challenges of photomultiplication measurement

Previous work on P4 and P5 done by Xie J.J et al. [1]. concluded that multiplication results showed a weak dependence of the carrier generation profile, suggesting that the α/β ratio in AlAsSb is only slightly higher than unity within the field range measured (>340 kV/cm). However, the measured wavelength dependence of multiplication on thicker structures demonstrated a strong dependence of the carrier generation profile, making this is the first observation of an InP based avalanche material which has a large α/β ratio property. It is necessary to make the measurements as accurately as possible. The challenges are

1. High surface dark current and bad metal contact due to unmodified etching process.
2. Side injection effects in p-i-n and especially in n-i-p configuration. Laser light may fall beyond the top of the mesa, causing absorption on the sidewall or around the mesa base due to lack of metal passivation.
3. Near unity magnitude multiplication in n-i-p diodes is extremely challenging (the measurement of M_h). Impact ionization by electrons dominates the avalanche process at the low electric fields. The difficulty of measurement increases under the illumination of the 405-nm wavelength light on the top of N1.

Figure 5.11 demonstrates edge injection on N1. Compared with edge injection, the onset of multiplication starts at higher reverse bias when illuminating at the centre, but did not find this effect when applying longer wavelength light. We believe that the photogeneration process is occurring in the i-region, which is similar to the edge injection process. Therefore, we need to be very careful to avoid any edge injection during pure carrier injection tests.

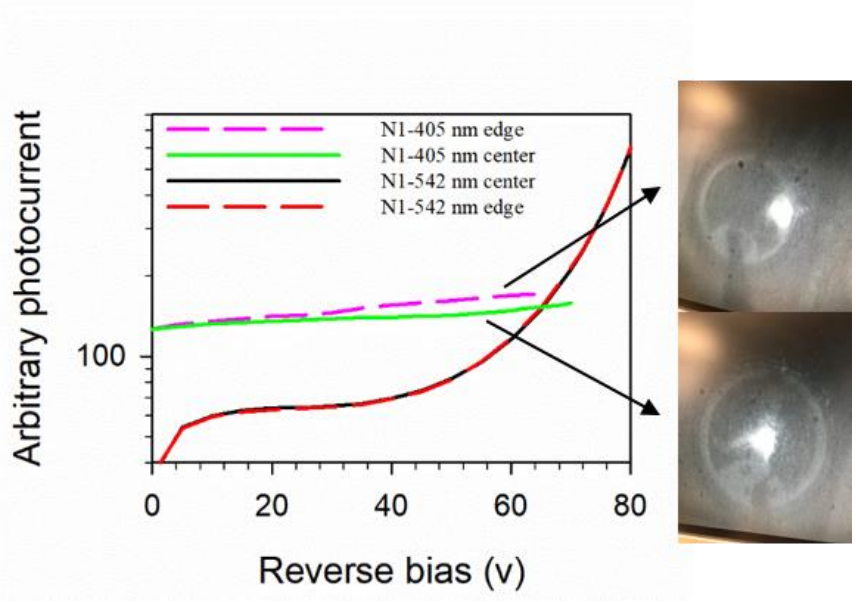

Figure 5.11. A comparison of multiplication under centre and edge injection profile used 405 nm and 542 nm wavelength.

5.4 Discussion

5.4.1 Simulation of avalanche multiplication with tapered electric-field

As discussed in Chapter 4, these AlAsSb digital alloy grown layers have a tapered electric-field profile in the avalanche region. Figure 5.12 shows the theoretical values when the avalanche region has a different doping density. Here, the p-i-n structure used a thickness of 1 μm and doping of 0, 1e15, 5e15 and 1e16 cm^{-3}, respectively. It suggests that the breakdown voltage reduces when the doping density increases, and this might be more serious with a thicker avalanche region due to a more significant difference in the peak electric-field. Therefore, the ionization coefficient analysis in this study has to include the effect of the tapered electric-field profile.

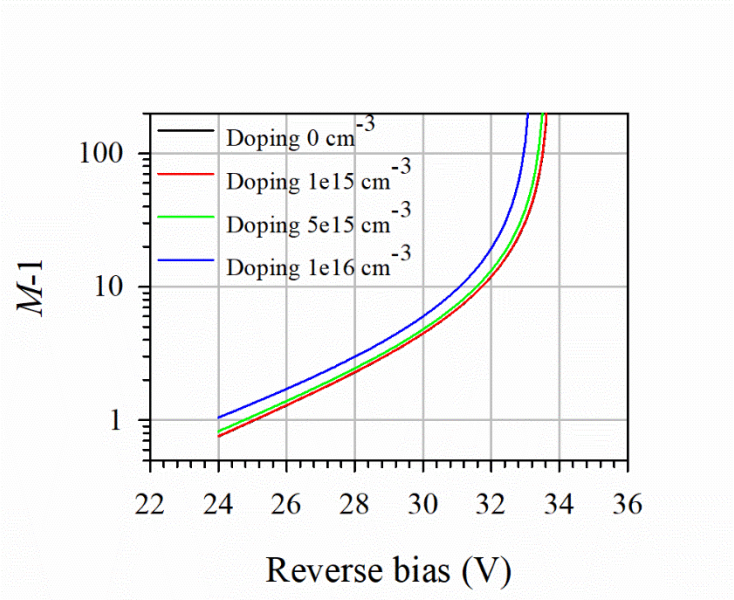

Figure 5.12. Theoretical values of *M*-1 with different background doping.

5.4.2 Impact ionization coefficients

The ionization coefficients as a function of electric-field were extracted from the multiplication results of P1-5 and N1-2 taking into consideration any tapered electric-field profile but ignoring any dead-space effects [6] by using a trial and error fitting technique which minimised the difference between the experimental and modeled data. The non-uniform electric field parameters were calculated and summarized in Table 4.1. The parameterized ionization coefficients cover a wide electric field range from 220-1250 kV/cm for α and from 360-1250 kV/cm for β and are given by;

$$\alpha(E) = 5.5\times10^{5}\exp(-(\frac{12.1\times10^{5}}{E})^{1.43}) \quad \text{cm}^{-1} \qquad (5.1)$$

for 220 kV/cm ≤ E ≤ 500 kV/cm and

$$\alpha(E) = 4.0\times10^{5}\exp(-(\frac{12.5\times10^{5}}{E})^{1.25}) \quad \text{cm}^{-1} \qquad (5.2)$$

for 500 kV/cm < E ≤ 1250 kV/cm,

$$\beta(E) = 3.2\times10^{5}\exp(-(\frac{17\times10^{5}}{E})^{1.6}) \quad \text{cm}^{-1} \qquad (5.3)$$

for 360 kV/cm ≤ E ≤ 1250 kV/cm.

These ionization coefficients are shown graphically in Figure 5.13(a), as is the α/β ratio as a function of inverse electric-field which shows that an α/β ratio of >100 can be achieved at electric fields below 460 kV/cm and this ratio can exceed 1000 at electric fields below 360 kV/cm. These coefficients are capable of reproducing the measured M_e and M_h for the different avalanche layer structures accurately as shown by the plot of (M-1) on a logarithmic scale in Figure 5.13(b). Excellent agreement was achieved even at very low gain values of $M \sim 1.01$. The onset of measurable M_e occurs well below the breakdown voltage in P1-P3, in contrast to the M_h in N1 and N2, as shown in Figure 5.13(b). This is because in our samples, we can accurately measure multiplication values down to 1.01 and at the electric-field where M_e gives us 1.01, the value of β is too low to give any measurable M_h. Although the M_h could only be experimentally obtained over a limited range in N1, the excellent agreement with the model down to values of $M_h = 1.01$ suggests that the low electric-field data for β is correct.

These coefficients can also replicate the M_e in P4 reasonably well if we use the parameters given in Table 4.1, but the fit to M_e in P5 is slightly worse at higher values of multiplication, even when allowing for the depletion into the p+ and n+ cladding regions. The reason for this is likely to be due to the fact that at very high electric fields in very thin structures, the ionization coefficients are not simple functions of electric-field [7] and more sophisticated modelling techniques are required to fit the experimental data. The rapidly increasing α/β ratio as the electric field decreases also explains the unusual result observed by Xie J.J. et al. [1], whereby the excess noise decreased significantly as the avalanche thickness increased from 80 nm to 230 nm, contrary to results observed in InAlAs and Si.

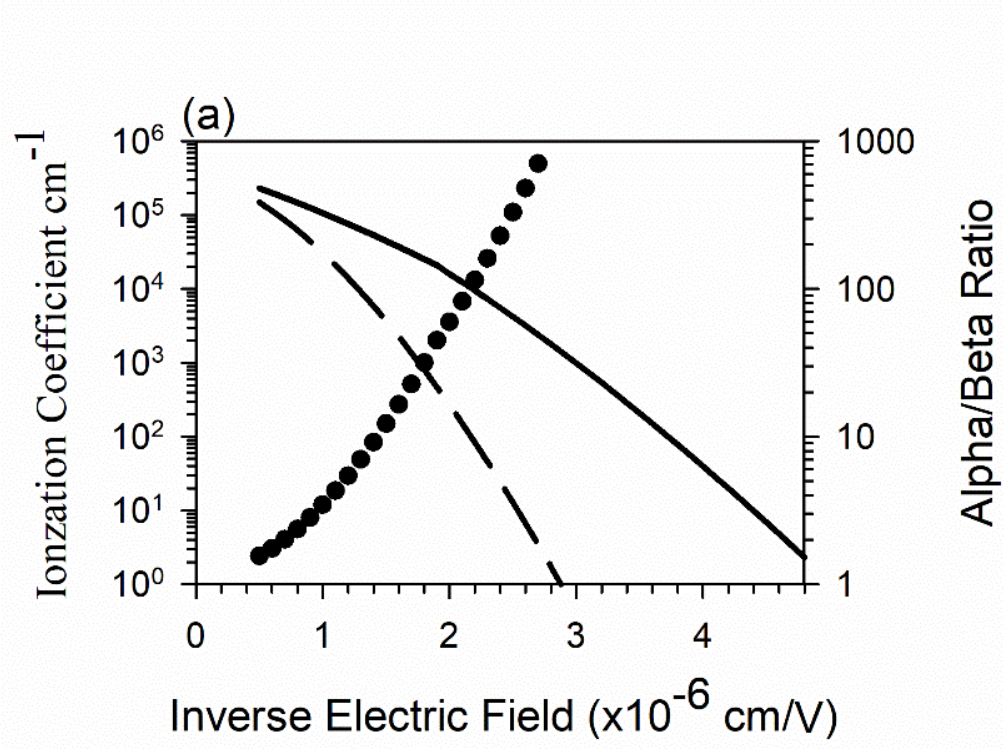

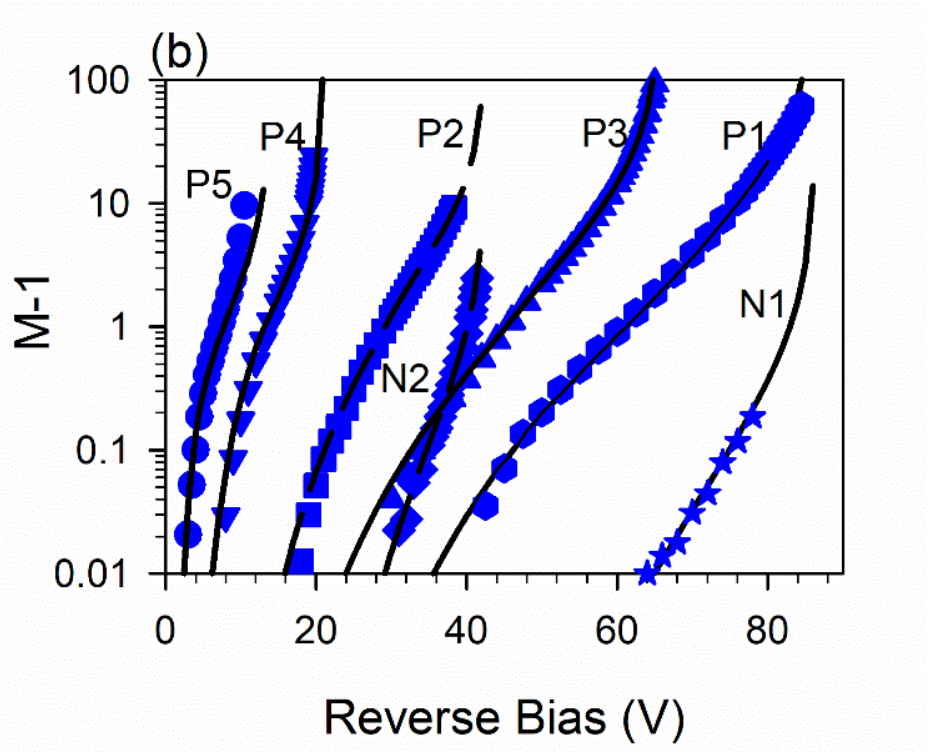

Figure 5.13. (a) Ionization coefficients α (Solid line) and β (Dashed line) and α/β ratio (Symbols) of AlAsSb. (b) Experimentally obtained M_e-1 (Symbols) at a wavelength of 405 nm and modelled (Lines) for P5, P4, P2, N2, P3, P1 and N1, going from left to right.

When the measured multiplication results are reasonable and trustable, the uncertainty of the simulation of impact ionization coefficients still exist. For example, the depletion thickness calculation depended on the assumption of a linear relationship between AlAs and AlSb for relative permittivity.

5.4.3 Breakdown voltage (V_{bd})

APDs have to be operated over a wide range of ambient temperatures. For telecommunication applications, APDs are required to operate with a constant gain. As the impact ionization process is strongly dependent on the temperature as shown in Equation (2.12), the variation in temperatures such as ambient temperature and junction temperature would affect the gain for a given reverse bias and the breakdown voltage of an APD. This is significant for the overall system's sensitivity. Miller's empirical expression, which is used to predict the breakdown voltage, is expressed below as

$$M = \frac{1}{1-(\frac{V}{V_{bd}})^c} \qquad (5.4)$$

Where V is the reverse bias voltage, V_{bd} is the breakdown voltage, and c is an adjustable parameter and determines the shape of the multiplication curve. By assuming $c = 1$, the equation can be rewritten as

$$M = \frac{1}{1-(\frac{1}{M})} \qquad (5.5)$$

Furthermore, the breakdown voltage is found as the intercept of the plot of V versus $1/M$. The temperature coefficient of breakdown voltage, C_{bd}, is equal to $\Delta V_{bd} / \Delta T$, where ΔV_{bd} and ΔT are the breakdown voltage and temperature differences. This is a good indicator of how sensitive the gain versus reverse bias is to temperature.

The breakdown voltage (V_{bd}) of five AlAsSb diodes were experimentally extracted by determining $1/M$ versus V characteristics (Miller's empirical expression) as shown in Figure 5.14. The highest measurable multiplication limits the values of $1/M$ due to high surface dark current and edge breakdown. The theoretical V_{bd} is summarized in Table 4.1 in Chapter 4 using the local model and the fitted impact ionization coefficients of AlAsSb. Compared with the measured breakdown voltages, the theoretical values are

always bigger. This is because of the uncertainties in the bending of the $1/M$ curve, as shown in the inner of Figure 5.14(a). For normal III-V materials, there is no observation of bending after the value of $1/M$ of ~0.1. This might be caused by high series resistance however we did not find high series resistance in our layers. To understand this uncertainty in predicting V_{bd} by $1/M$ for a large α/β ratio material, the following part is a breakdown voltage analysis of an artificial semiconductor.

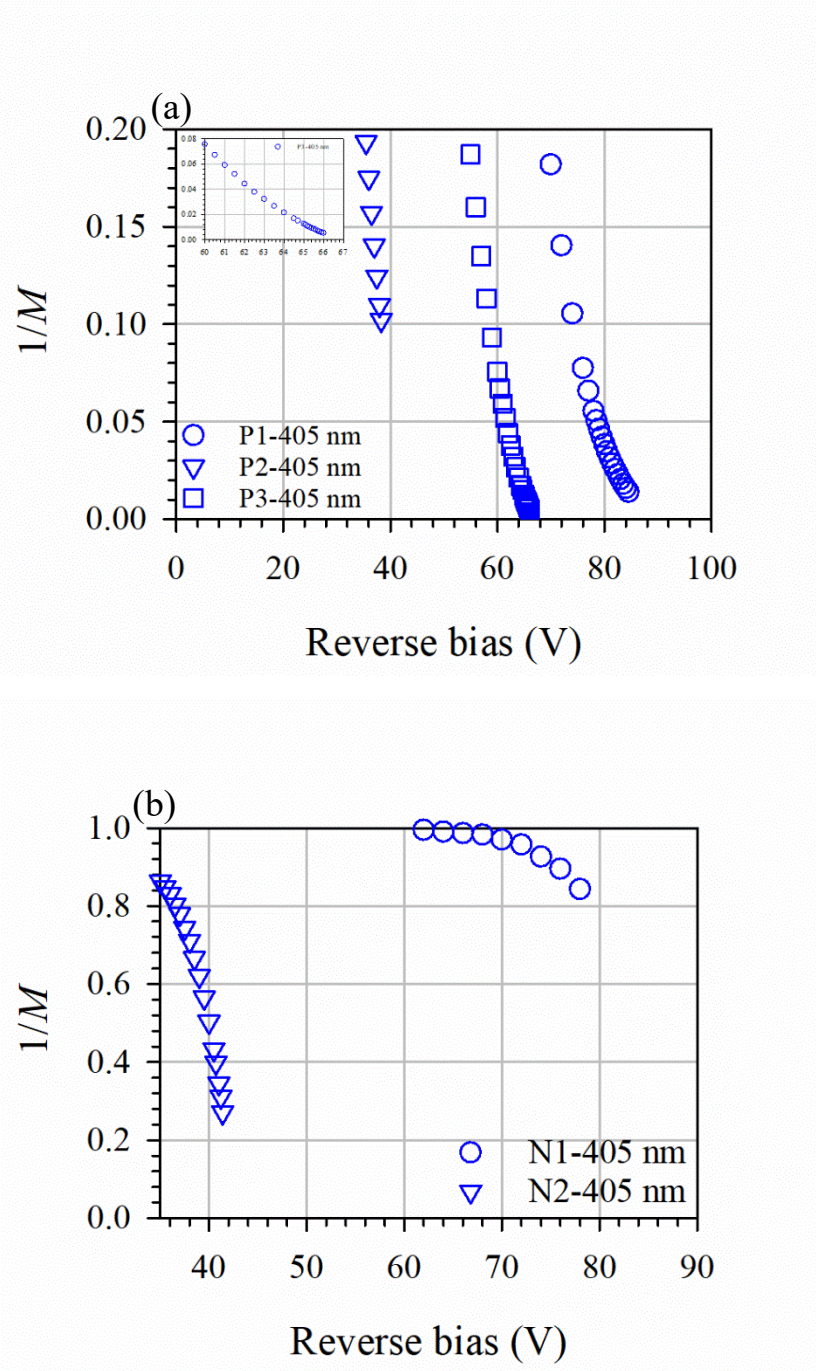

Figure 5.14. (a) The measured $1/M_e$ for P1, P3 and P2 from right to left. (b) The measured $1/M_h$ for N1 and N2 from right to left

The impact ionization coefficient in this artificial semiconductor for electrons, α is expressed as

$$\alpha = 7.03\times10^{5}\times\exp(-(\frac{12.3\times10^{5}}{E})^{1}) \qquad (5.6)$$

The impact ionization coefficient for holes, β is reduced by a ratio of 2, 5, 10, 20, 50, 100, 1000 and an extreme case of β of 0. Figure 5.15(a) shows the coefficients for all these cases. Assuming a 1 μm perfect p-i-n structure (constant electric field in the avalanche layer), the local model can be rewritten as Equation (2.18). The calculated M_e is shown in Figure 5.15(b). As the ratio of α/β increases, the breakdown voltage increases and the dark brown solid line presents the extreme case of β of 0. The calculated $1/M_e$ is in Figure 5.15(c). It is clearly hard to predict V_{bd} from just M_e. As the ratio of α/β increases, it is harder to draw a straight line through $1/M_e$ to predict V_{bd} unless you can go to very high values of multiplication. The large α/β ratio generally happens in very thick structure so we ignore "dead-space" effects. If we did the analysis using $1/M_h$, however, we found that we may predict the V_{bd} quite accurately. In reality, the measurement of M_h is extremely hard for a material of large ionization ratio, for example, measurement of M_h on N1. Figure 5.15(d) presents the reverse bias at different value of multiplication. It suggests that the V_{bd} is very similar to the reverse bias at M of 20 for a case of k of 2. However, when k of 1000 the reverse bias at M of 20 is 39 V and the V_{bd} is 53 V therefore the difference is huge. Even at M of 200, the reverse bias is 47 V, still ~10% away compared to V_{bd}.

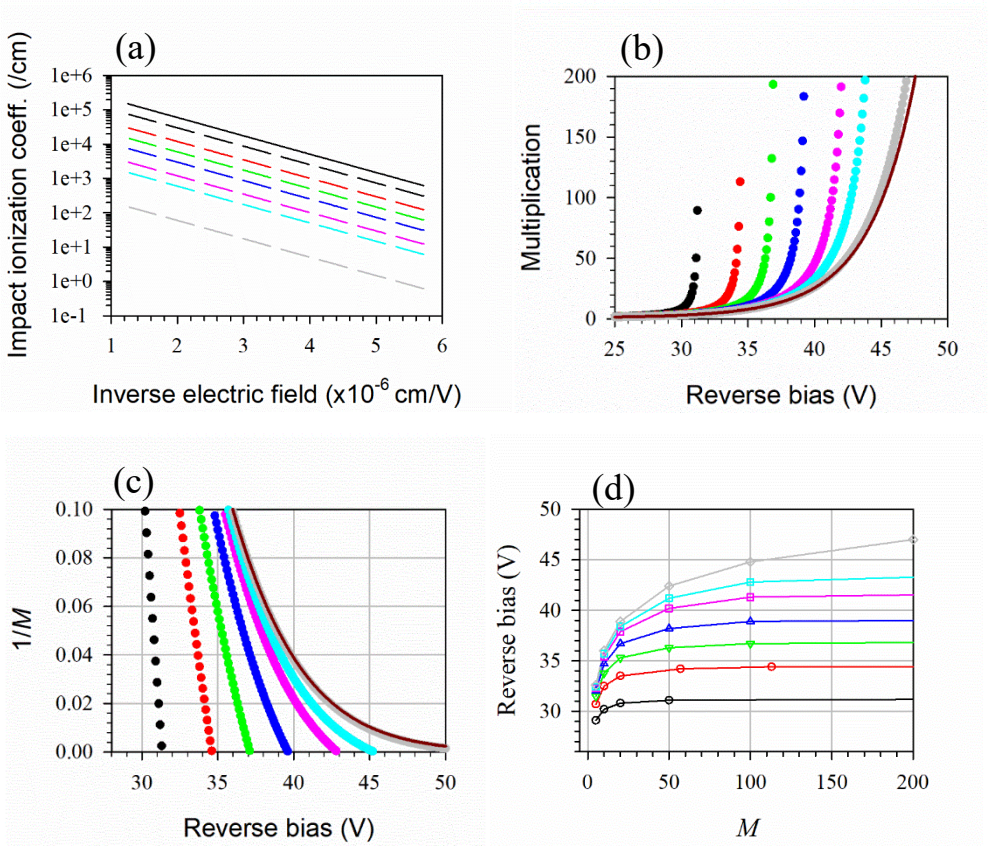

Figure 5.15. (a) Impact ionization coefficient of an artificial semiconductor. The solid line is α and the dashed line is β. The ratio is 2, 5, 10, 20, 50, 100 and 1000 from top to bottom. (b) Simulated M_e the solid line presents the extreme case of β of 0. (c) Calculated $1/M_e$ for a different ratio. (d) Reverse bias against multiplication.

In 1997, Allam J. [8] showed that the breakdown voltage in wide bandgap semiconductors linearly depend on a Brillouin-zone-average energy gap, $\langle E_{ind} \rangle$. In his hypothesis, a quasi-particle band structure was used to determine values of $\langle E_{ind} \rangle$, given by

$$\langle E_{ind} \rangle = \frac{1}{8} \times (E_\Gamma + 3E_X + 4E_L) \qquad (5.7)$$

Where E_Γ, E_X and E_L are the energy of the conduction band at the Γ, X and L extrema in eV. The equation could be simplified since the Γ minimum has little effect on the high-filed transport for silicon as

$$\langle E_{ind} \rangle_m = \frac{1}{7} \times (3E_X + 4E_L) \qquad (5.8)$$

Furthermore, the relation of V_{bd} and $\langle E_{ind} \rangle$ is described by

$$V_{bd} = 45.8\left(\langle Eind \rangle - 1.01\right) \qquad (5.9)$$

This relation was demonstrated to predict the V_{bd} accurately in several wide-bandgap semiconductors, as shown in Figure 5.16.

To test equation (5.7)-(5.9) for AlAsSb, the V_{bd} of 1 μm perfect structure was calculated used the local model and the fitted ionization coefficients, rather than using the measured V_{bd}, to minimise errors of bending of $1/M$ curve and the scattering environment (such as avalanche thickness and doping density), and plotted in Figure 5.16 used a red star symbol. It shows that Allam's relation agrees well with the theoretical breakdown voltage only if the band energy at L valley is about 2.88 eV. This result took the assumption of the conduction band energy at Γ and X are 2.21 eV and 1.58 eV, respectively, and V_{bd} of 1 μm AlAsSb is 59.6 V. However, to our best knowledge, the conduction energy band at L for most III-V materials is between energy band at Γ and X valley. It suggests that Allen's relation is no longer viable for this material.

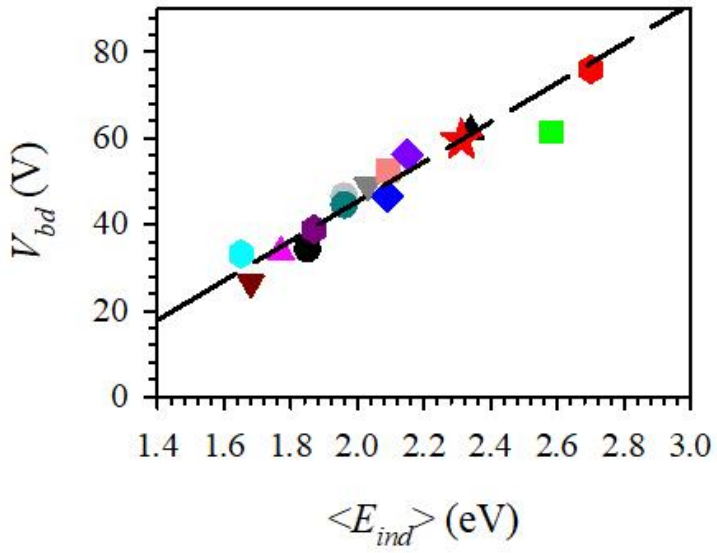

Figure 5.16. Measured 1 μm V_{bd} plotted as a function of <E_{ind}> of different materials. The red star shows AlAsSb assumed energy of L valley is about 2.88 eV and dashed line shows Equation (5.7). The rest colour symbols are different materials such as Si, Ge, InP, GaAs, $Al_xGa_{1-x}As$, GaP et al. More detail can be found in Ref. [4].

5.4.4 Comparison with other avalanche materials

To further emphasise how much larger the α/β ratio is in AlAsSb, it is compared to traditional III-V materials grown on InP substrate and Si, Figure 5.17 presents the ionization coefficients of AlAsSb, together with those of InP, InAlAs and Si as a function of the inverse electric field. The α in all three III-V avalanche materials appear to be

almost identical, despite different conduction band structures but the most interesting observation is that the β is significantly lower in AlAsSb, giving rise to the large α/β ratio. So this should give rise to APDs with a better excess noise characteristics.

A theoretical comparison of M_e and M_h in an ideal 1 μm structure is shown in Figure 5.18. We observed a sharp breakdown for each structure as the electric field increases, and the breakdown voltage of AlAsSb is approximately 1.2 and 1.8 times larger than those of InAlAs and Si respectively owing to the combination of a relatively large bandgap and larger α/β ratios. The difference between M_e and M_h of AlAsSb is clearly shown here to emphasis its unique behaviour. It also suggests that an ideal 1 μm p-i-n structure operating at a gain of 10, would undergo multiplication dominated by electron ionization due to α/β ratio of >40.

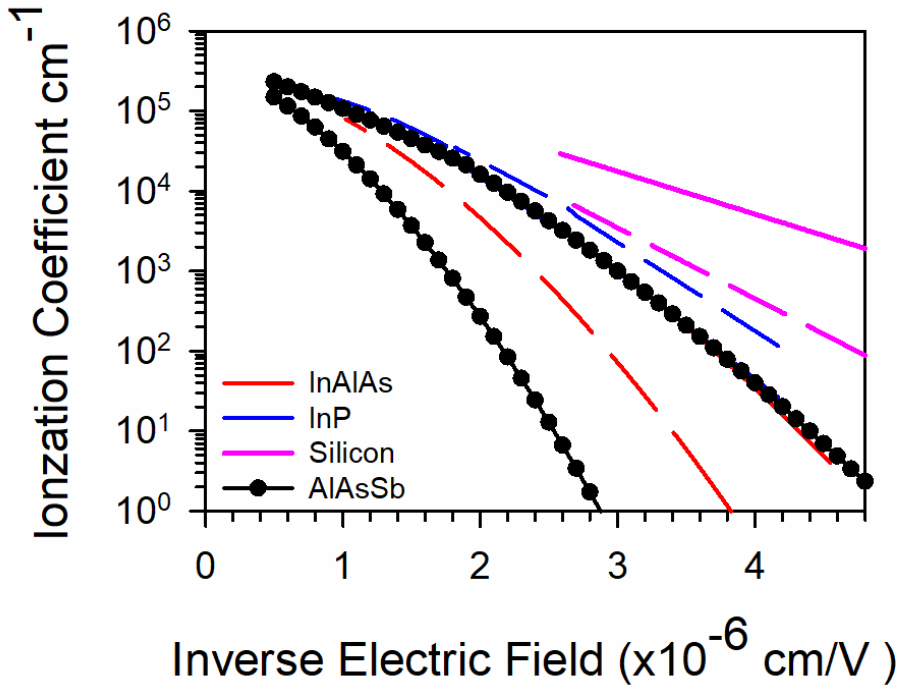

Figure 5.17. Ionization coefficients α (Solid line) and β (Dashed line) of AlAsSb compared to InAlAs, InP and silicon. α of InAlAs and InP are almost identical to that of AlAsSb and are difficult to separate in the figure.

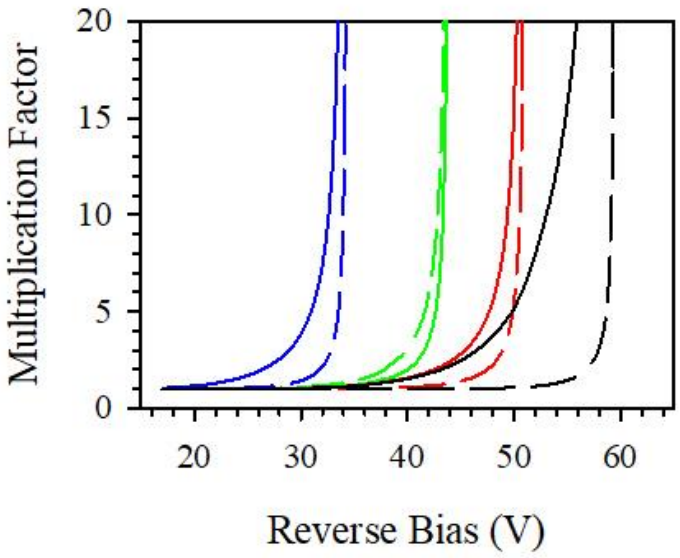

Figure 5.18. Simulated multiplication factor of 1 μm perfect avalanche structure of InP (green), InAlAs (Red), Silicon (blue) and AlAsSb (Black). Solid line is M_e and dashed line is M_h

AlAsSb is the best avalanche material grown lattice-matched on a InP substrate and is even potentially better than silicon. It is interesting to compare it with the electron avalanche photodiode (eAPD), where it has been demonstrated that only one carrier type undergoes appreciable impact ionization. So far, the most reported eAPD are InAs and HgCdTe. Both materials demonstrate that avalanche multiplication is dominated by electron impact ionization and there is no observation of breakdown, and give extremely low excess noise performance, < k~0 [9, 10]. Our measured M_e of P1-P3 shows a clear avalanche breakdown, and the measured M_h of N1-N2 indicates that holes do ionize as the reverse bias increases. By extrapolating β from Figure 5.17, it can be seen that it reduces significantly in comparison to other materials, so that in the case of very thick avalanching structures we can have effectively single carrier multiplication. Figure 5.19 shows the M_e-1 and M_h-1 of a 6 μm and 10 μm avalanching region AlAsSb APD and the red solid lines are for the beta is zero and truly single carrier multiplication. It suggests that holes hardly ionize before the value of M_e achieves a gain of 30 and 80 for 6 μm and 10 μm avalanching structures, respectively. Beyond M_e greater than 100 the M_e increases rapidly to breakdown. Such an example of near single carrier multiplication is only at very low electric-fields and this requires a much thicker avalanche region, which has to suffer the penalty of speed.

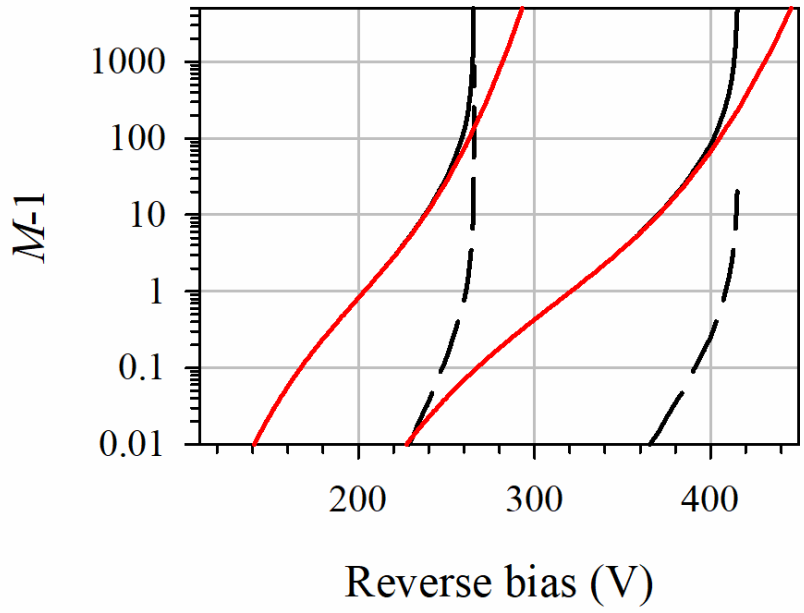

Figure 5.19. Theoretical prediction of multiplication in 6 and 10 μm. Black is AlAsSb and red is single carrier multiplication.

5.4.5 Comparison with Sb-based materials

Figure 5.20 shows a comparison of electron and hole impact ionization coefficients for recent published Sb-based APDs. $Al_xIn_{1-x}As_ySb_{1-y}$ (x = 0.3-0.7) latticed-matched to GaSb substrates has also demonstrated large α/β ratios and low excess noise characterisation [11-14]. More literature reviews can be found in Chapter 1. Here, we compare the reported electron and hole impact ionization coefficients of $Al_{0.7}In_{0.3}As_{0.3}Sb_{0.7}$. Yuan Y. et al. [15] measured multiplication and excess noise with the wavelengths of 543, 633 and 850 nm on a 1 μm homojuntion p-i-n diode. The highest multiplication values was found by 543 nm wavelength illumination, while the lowest excess noise, k of 0.03, was found with 543 nm wavelength. The fitted impact ionization coefficient by Yuan Y. et al. is well agreed with the fitted results used a 1 μm homojunction p-i-n diodes with different digital alloys [16]. It suggests that the α/β ratio of $Al_{0.7}In_{0.3}As_{0.3}Sb_{0.7}$ is smaller than that of AlAsSb and the breakdown voltage of $Al_{0.7}In_{0.3}As_{0.3}Sb_{0.7}$ at similar thickness is also smaller than that of AlAsSb due to a lower bandgap. Recently Bank S.R. et al. [17] demonstrated a lower excess noise in $Al_{0.5}In_{0.5}As_{0.5}Sb_{0.5}$ compared with the measured excess noise in $Al_{0.7}In_{0.3}As_{0.3}Sb_{0.7}$ on 890 nm p-i-n diode. Therefore, a better α/β ratios are possibly observed in $Al_xIn_{1-x}As_ySb_{1-y}$ with In-rich. Collins X. et al. [18] recently reported that $Al_{0.9}Ga_{0.1}As_{0.08}Sb_{0.92}$

lattice-matched to GaSb substrates shown $\beta>\alpha$ based on multiplication measurements using p-i-n and n-i-p didoes of various thin avalanche thickness (i-region = 135 and 300 nm). Previously, Grzesik M. [19] also shown $\beta>\alpha$ in $Al_xGa_{1-x}As_ySb_{1-y}$ (x = 0.4, 0.55, 0.65) lattice-matched to GaSb substrate. His investigation covered three alloy compositions and low electric-fields. Compared with AlAsSb and $Al_xIn_{1-x}As_ySb_{1-y}$ the highest magnitude of the impact ionization coefficients was observed at similar electric-fields. The interesting point is β is higher than α in $Al_xGa_{1-x}As_ySb_{1-y}$ on GaSb even the β/α is smaller than other two materials.

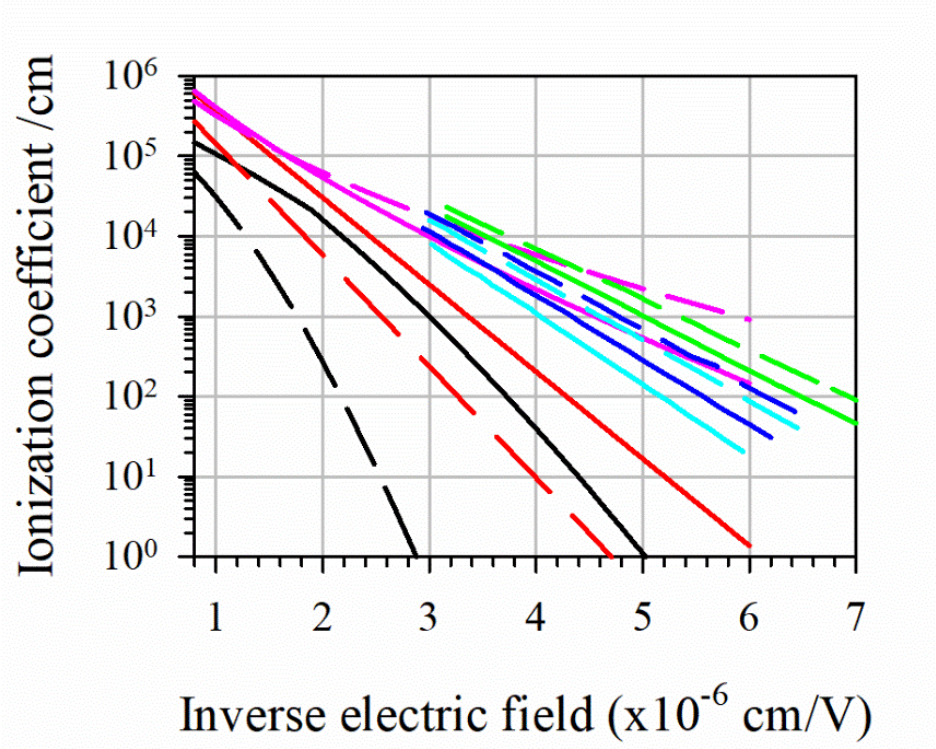

Figure 5.20. Parameterized α and β of AlAsSb/InP (black) are compared with those of $Al_{0.7}In_{0.3}As_{0.3}Sb_{0.7}$/GaSb by Yuan Y. (Red), of $Al_{0.9}Ga_{0.1}As_{0.08}Sb_{0.92}$/GaSb by Collins X. (Pink) and $Al_xGa_{1-x}As_ySb_{1-y}$/GaSb Grzesik M. (Green: $Al_{0.4}Ga_{0.6}As_ySb_{1-y}$ Blue: $Al_{0.55}Ga_{0.45}As_ySb_{1-y}$ Cyan: $Al_{0.65}Ga_{0.35}As_ySb_{1-y}$). Only AlAsSb was grown on InP substrates. Solid lines are α and dashed lines are β. All references are given in main text.

5.4.6 Explanation for large α/β ratio in AlAsSb

Campbell's group [20] claimed that the low excess noise of $Al_xIn_{1-x}As_ySb_{1-y}$ benefitted from digital alloy growth technology. They theoretical predicted the band structure using an environment-dependent tight-binding method. Compared with the random alloy

band structure, there is a mini-gap between the second and third conduction and valance bands. The optical phonon energy of the InAlAs and AlInAsSb is less than most of the mini-gaps. Therefore, the holes are hardly scattering to higher-order bands due to without any equivalent paths to absorb energies. However, despite observations of mini-gaps in the conduction band electrons can absorb energy through in-plane scattering, making electrons scatter to higher energy band.

Previously large ratio has been observed for detectors constructed from HgCdTe, InAs and InSb. Those semiconductors own very low electron masses, large hole masses, and large separation between band minimum of Γ valley and the X and L satellite valleys, which possibly contribute to low optical phonon scattering rates for electrons, high optical phonon scattering rates and high threshold energy for holes. Grein C.H. et al. [21] reported that the α/β ratio of Ga-rich $Al_xGa_{1-x}Sb$ exhibits an enhancement at low electric-field due to "resonant" band structure caused by the spin-orbit splitting.

For this study, our layers were also grown by digital alloy growth technology, but the difference is that we used a very short period (13 A) superlattice of AlAs (1.7A) and AlAs (11.4 A) compared to the 10-20 ML period used by Campbell's group [11, 12]. The bandgap properties of P4 and P5 grown as a random alloy have broadly similar bandgap as P1-P3 and N1-N2, as shown in Figure 4.21. Our fitted ionization coefficients are able to reproduce all measured results including layers by random alloy growth technique. Therefore, we do not believe that the DA superlattice is responsible for the large α/β ratio. However, an interesting hypothesis is that adding antimony modifies the valance band and there is little influence on the conduction band. The more significant spin-orbit energy in AlAsSb introduces high optical phonon scattering rates and high threshold energy for holes and a flat heavy hole band resulting ionization of hole significantly reduces compared with InAlAs and InP [22, 23].

5.5 Conclusion

Impact ionization and avalanche multiplication in AlAsSb/InP APDs have been characterised at room temperature. This is for the first time demonstration of avalanche multiplication in bulk AlAsSb. The multiplication measurements were performed as

accurate as possible in a series of didoes with avalanche region width from 1.55 μm down to 80 nm. From these, the ionization coefficients as a function of inverse electric-field have been extracted used the Local model with the tapered electric-field profile. As the field increase the α/β ratio is found to converge slowly.

The multiplication characteristics predicted using the fitted coefficients and the local model are presented a good agreement with measured multiplication results down to M~0.01, and these coefficients demonstrated availability on structures not only grown by digital alloy but also random alloy technique. The α/β ratio is found to vary from 1000 to 2 over an electric-field range from 220-1250 kV/cm, making it the first report of a wide band-gap III-V semiconductor with ionization coefficient ratios much larger than any other wide bandgap III-V semiconductor material, much more significantly, similar to or larger than that observed in silicon. The basic purpose of this work is that the combination of InGaAs as an absorber and AlAsSb as multiplication material generates a new brand of high speed and high sensitivity SAM-APDs. This work suggests AlAsSb ideal for the multiplication region in InP based telecommunication SAM-APDs

A further finding is that the extremely low hole ionization coefficients may cause near single carrier multiplication process, potentially leads to high-speed APDs. However, this near single carrier multiplication only happens at the low electric field (a thick structure), it suggests there will be a trade-off between speed and sensitivity.

5.6 References

[1] J. Xie, S. Xie, R. C. Tozer and C.H.Tan. "Excess Noise Characterization of AlAsSb Avalanche Photodiodes" IEEE Trans. Electron. Devices. Vol.59, no.6. May 2012.

[2] X. Zhou, L. L. G. Pinel, S. J. Dimler, S. Zhang, J. S. Ng, and C. H. Tan, "Thin Al1-xGaxAs0.56Sb0.44 Diodes With Low Excess Noise," IEEE J. Sel. Top. Quantum Electron. 24(2), 3800105 (2018).

[3] L. L. G. Pinel, S. J. Dimler, X. Zhou, S. Abdullah, S. Zhang, C. H. Tan and J. S. Ng, "Effects of carrier injection profile on low noise thin Al0.85Ga0.15As0.56Sb0.44 avalanche photodiodes," Opt. Exp. Vol. 26, No. 3, pp. 3568-3576, Feb. 2018.

[4] M. M. Hayat, B. E. A. Saleh, and M. C. Teich, "Effect of dead space on gain and noise of double-carrier-multiplication avalanche photodiodes," IEEE Trans. Electron Devices, vol. 39, no. 3, pp. 546–552, Mar. 1992.

[5] M. H. Woods, W. C. Johnson & M. A. Lambert, "Use of a Schottky barrier to measure impact ionization coefficients in semiconductors," Solid State Electron, Vol. 16, pp. 381–394, 1973.

[6] W.N. Grant, "Electron and hole ionization rates in epitaxial silicon at high electric fields," Solid-state Electronics. Vol. 16, pp. 1189–1203, 1973.

[7] S. A. Plimmer, J.P.R. David and D.S. Ong, "The merits and limitations of local impact ionization theory," IEEE Trans. Elec. Devices, vol. 47, pp. 1080–1088, 2000.

[8] J. Allam, "Universal dependence of avalanche breakdown on bandstructure: choosing materials for high-power devices", Jpn. J. Appl. Phys., vol. 36, no. 1(3B), pp. 1529-1542, Mar. 1997.

[9] A.R.J. Marshall, C.H. Tan, M. J. Steer, and J.P.R. David, "Extremely low excess noise in InAs electron avalanche photodiodes," IEEE Photon. Tech. Lett., vol. 21, no. 13, July 2009.

[10] J. Beck, C. Wan, M. Kinch, J. Robinson, P. Mitra, R. Scritchfield, F. Ma and J. Campbell, "The HgCdTe electron avalanche photodiode," J. Electron. Mater., Vol. 35, No. 6, 2006.

[11] M.E. Woodson, M. Ren, S.J. Maddox, Y. Chen, S. Bank and J. Campbell, "Low-noise AlInAsSb avalanche photodiode" App. Phy. Let., Vol. 108, Feb. 2016.

[12] Min Ren, Scott J. Maddox, Madison E. Woodson, Yaojia Chen, Seth R. Bank, and Joe C. Campbell, "Characteristics of AlxIn1-xAsySb1-y (x:0.3-0.7) avalanche photodiodes," Lightwave Tech., vol. 35, no. 12, pp. 2380-2384, 15 June 2017.

[13] Seth R. Bank et al., "Avalanche photodiodes based on the AlInAsSb materials system," IEEE J. Sel. Top. Quantum Electron., vol. 24, no. 2, Mar./Apr. 2018, Art. no. 3800407.

[14] Min Ren, S. J. Maddox, Yaojia Chen, S. R. Bank, and J. C. Campbell, "AlInAsSb separate absorption, charge, and multiplication avalanche photodiodes," Appl. Phys. Lett., vol. 108, no. 19, 191108, May 9, 2016.

[15] Y. Yuan, J. Zheng, A.K. Rockwell, S.D. March, S.R. Bank and J.C. Campbell, “AlInAsSb impact ionization coefficients”, IEEE Photon. Tech. Let., vol. 31, no. 4, pp. 315-318, Feb. 2019.
[16] Y. Yuan et al., “Comparison of different period digital alloy AlInAsSb avalanche photodiodes”, Jou. of Light. Tech., vol. 37, no. 14, pp. 3647-3654, Jul. 2019.
[17] Seth R. Bank et al., “Avalanche photodiodes based on the AlInAsSb materials system,” IEEE J. Sel. Top. Quantum Electron., vol. 24, no. 2, Mar./Apr. 2018, Art. no. 3800407.
[18] X. Collins, A.P. Craig, T. Roblin and A.R.J. Marshall, “Impact ionization in Al0.9Ga0.1As0.08Sb0.92 for Sb-based avalanche photodiodes,” Appl. Phys. Lett., vol. 112, no. 021103, Jan. 2018.
[19] M. Grzesik, “Impact ionization in AlGaSb avalanche photodidoes,”PhD Thesis, University of Massachusetts lowell, USA, 2008.
[20] J. Zhang et al., “Digital alloy InAlAs avalanche photodiode,” J. of Lightwave Techno., vol. 36, no. 17, pp. 3580-3585, Sep 2018.
[21] C.H. Grein and H. Ehrenreich, “Impact ionization enhancements in AlGaSb avalanche photodiodes,” Appl. Phys. Lett., vol. 77, no. 19, pp. 3048-3050, Nov. 2000.
[22] Y. L. Goh, A. R. J. Marshall, D. J. Massey, J. S. Ng, C. H. Tan, M. Hopkinson, J. P. R. David, S.K. Jones, C. C. Button, S. M. Pinches, Excess Avalanche Noise in $In_{0.52}Al_{0.48}$ As IEEE J. Quantum Electron . vol. 43, no. 6: pp. 503-507, 2007.
[23] L. J. J. Tan, J. S. Ng, C. H. Tan and J. P. R. David, “Avalanche noise characteristics in sub-micron InP diodes”, IEEE J. of Quantum Electronics, vol. 44, no. 4, pp. 378 – 382, Apr. 2008.

CHAPTER 6:

EXCESS NOISE OF AlAsSb DIODES AND SENSITIVITY ANALYSIS

6.1 Introduction

The advantages of using InP based APDs at traditional telecommunication wavelengths of 1.31 μm and 1.55 μm as a way of increasing sensitivity and speed of communication networks is well documented and discussed in more detail in Chapter 1 [1-3]. The best results at 25 Gb/s to 50 Gb/s currently utilise ≤100 nm thick InAlAs multiplication regions, and these provide a sensitivity of between -22.6 dBm to -10 dBm respectively at a BER of 1×10^{-12} [4-6]. There have been many attempts at improving the performance of APDs for telecommunications, for example utilising Ge/Si [7-9], nanopillars [10], AlInAsSb [11-13] or InAs [14], however these face problems such as limited wavelength operation, often requiring complicated growth procedures, sophisticated fabrication technologies or the use of more expensive substrates. In the previous chapter, a small β/α ratio has been demonstrated in AlAsSb diodes used photo-multiplication measurements. According to McIntyre's theory [15], k has to be very low to obtain low excess noise at high M. AlAsSb may have extremely low excess noise at room temperature, even at high gains, exceeding the performance of all materials lattice-matched to InP and even silicon.

To date, only characterisation of excess noise on very thin $Al_xGa_{1-x}AsSb$ (x = 0.85-1) diodes has been reported. However, this includes the well-known "dead space" effect. In this chapter excess noise measurements were experimentally performed on the same set of device structures (P1-P3 and N1-N2) as described in Chapter 4 using blue light (420-nm wavelength) initially. The results will further provide significant information regarding the avalanche multiplication noise characteristics and confirm if electrons ionize more easily in this material. This chapter also shows a systematic study on the excess noise characteristics using a green and red light source (542-nm and 633-nm wavelength). Under mixed carrier injection condition, carriers are generated in both

cladding layers and in the high field layers of a diode. The excess noise value was determined from the measured noise power and photocurrent which was thoroughly discussed in Chapter 3. Here, we analyse for the first time the excess results using a new mix injection model. We then analyse the potential benefits of adopting AlAsSb in high-speed APDs by undertaking a full bandwidth and sensitivity analysis.

6.2 Excess noise characteristics of AlAsSb

Excess noise was measured on P1-P5 and N1-N2. The first interesting wavelength is at 420 nm (using a Thorlabs LED M420F2 [16]. In this section, 420 nm LED was used to measure the excess noise due to high noise from the 405 nm laser, but the absorption profile is very similar compared to it by 405 nm laser). The absorption coefficient for 420 nm illumination is 1.2×10^5 cm^{-1} resulting in either only minority electrons or minority holes being injected into the high field multiplication regions of the p-i-n and n-i-p structures respectively. The excess noise when electrons initiate the multiplication is conventionally characterised by the k factor, defined by McIntyre [15] as the materials β/α ratio when $\alpha>\beta$ as $F_e = kM + (1 - k)[2 - 1/M]$. Measurements were also performed using 542 and 633-nm light (two He-Ne lasers). The much lower absorption coefficient of 2×10^3 cm^{-1} for 633 nm illumination results in significant carrier generation within the multiplication region. More details of the absorption profile are discussed in Chapter 4. The He-Ne laser could be focused into a tight spot with a diameter ~10 μm while the spot of the LED usually is larger than the device diameter ~220 μm. The power of the light source is also significant for noise measurements, and the primary current was about 2 μA to ensure that the circuit can measure the noise power. The measurements were repeated on at least 5 different devices with different optical powers to ensure consistency. Owing to the high dark current introducing extra noise in the biggest devices, we only look at devices of diameter ~220 μm.

Figure 6.1 shows the (M-1) data obtained using different wavelength illumination on these avalanching structures as a function of reverse bias. By plotting (M-1) on a log scale, we can see how the onset of the avalanche process changes with wavelength more clearly. The results here are similar to those measured in the previous chapter on

the multiplication setup. It suggests that comparing the measured multiplication at a wavelength of 405 nm is similar to the multiplication using a wavelength of 420 nm on the noise measurement setup. As expected, the multiplication results from the 542 nm illumination as shown in Figure 6.1, with an absorption coefficient of 1.2×10^4 cm^{-1}, fall between the 420-nm and 633-nm wavelength results. The largest multiplication values in the p-i-n structures for a given voltage is obtained with 420 nm illumination, and this decreases as the wavelength increases. The opposite trend was observed on the two n-i-p structures with hardly any measurable multiplication from 420 nm illumination even at high reverse biases on N1 and N2. The similar thickness pairs show comparable multiplication under illumination of 633 nm wavelength. These repeatable multiplication results from the excess noise setup give us confidence to proceed to the next stage of noise measurements.

A comparison of excess noise measurements made on different devices or different light power with three different wavelengths on P3 as shown in Figure 6.2 suggests that the noise characteristics is independent of the power of the light source and location of device but that the excess noise has a significant change under different wavelength illumination. As the wavelength of illumination increases, so does the excess noise, in qualitative agreement seem in the other p-i-n structures. We repeated similar measurements on all other layers.

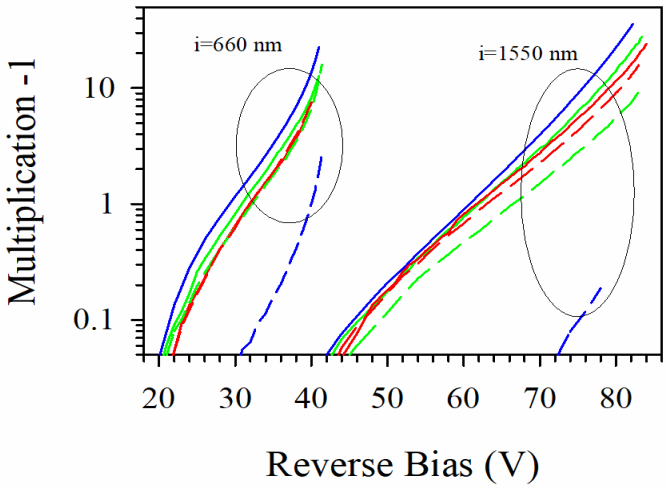

Figure 6.1. Measured multiplication at different wavelengths versus applied reverse bias for P1-P2 (solid lines) and N1-N2 (dashed lines). Blue for 420 nm, green for 542 nm and red for 633 nm.

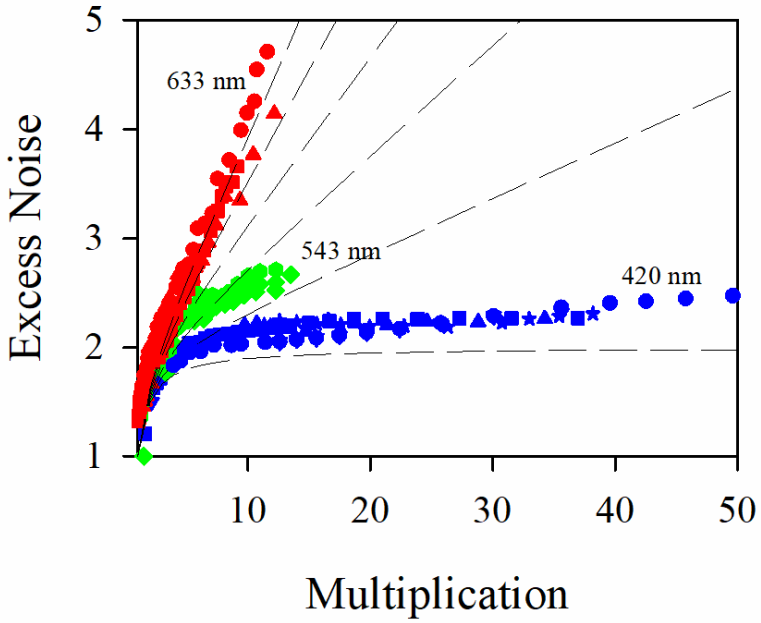

Figure 6.2. Measured excess noise versus multiplication for P3. *k* increase from 0 to 0.25 in steps of 0.05.

The excess noise (*F*) of the photocurrent when undergoing avalanche multiplication is shown in Figure 6.2-6.5. No excess noise data could be obtained on the two n-i-p structures with 420 nm illumination as there was only a small pure hole initiated multiplication. Different *k* values defined by McIntyre are also shown in Figure 6.2-6.5 as dashed lines. When pure electrons initiate the avalanche process, P1 and P3 show very low excess noise (F_e) corresponding to effective *k* values of 0.005 and 0.012, respectively (blue symbols). P2 demonstrates a larger effective *k* of 0.04 due to the higher electric field encountered and hence larger β/α, as shown in Figure 5.17, a trend further exacerbated in P4 and P5 even with the advantage of dead space effects. The F_e in the two thinnest structures behaves differently, starting low but increasing more rapidly with increasing multiplication. In these structures, the very high electric-fields means that β/α is close to unity, but that dead-space effects are suppressing the excess noise.

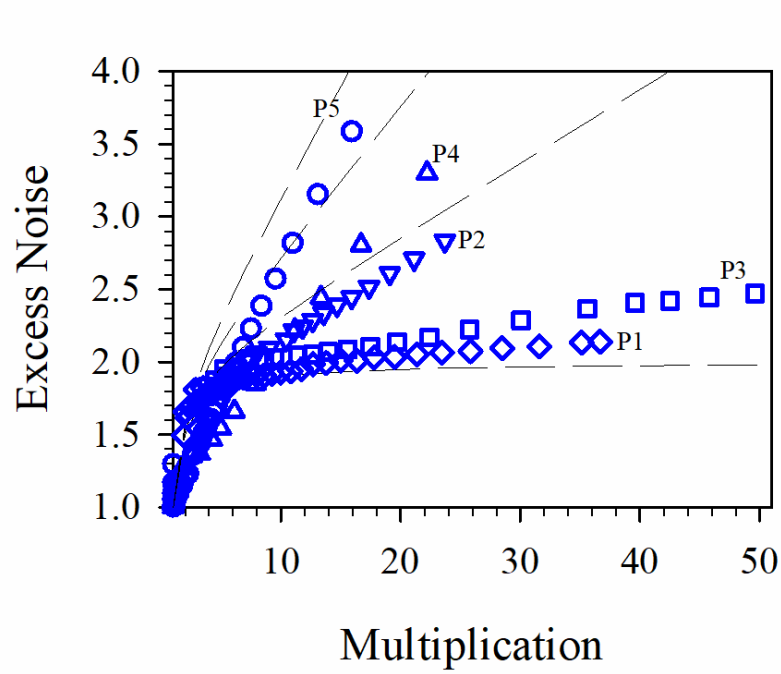

Figure 6.3. Measured excess noise versus multiplication with 420 nm illumination in all p-i-n structure. *k* increase from 0 in steps of 0.05.

Due to the significant asymmetry in α and β, Figure 6.2, 6.4 and 6.5 show that the measured excess noise increases as the wavelength of illumination increases on the p-i-n structures with the opposite trend seen in the n-i-p structure as one might expect qualitatively. Under mixed carrier injection conditions, the *F* does not follow the theoretical McIntyre expression given earlier. In that analysis, McIntyre assumes the injection of either an electron or a hole at the boundary of the APD's avalanche region. The excess noise results at wavelengths of 633 nm and 542 nm on N1 and N2 are significantly higher than those of electron initiated multiplication especially at high multiplication value, in agreement with $\alpha >> \beta$ deduced from the multiplication measurements. The difference of excess noise between P1-633 (542) and N1-633 (542) is more significant than those of P2-633 (542) and N2-633 (542). They are also more significant than the noise reported in $Al_xGa_{1-x}AsSb$ with thin avalanche region. This also indicates that the bulk AlAsSb has very small β/α ratio at the low electric field.

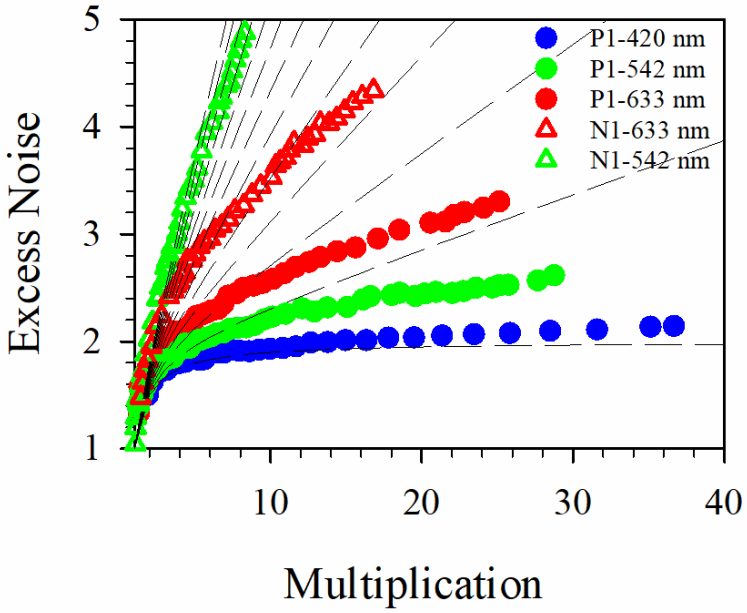

Figure 6.4. Measured excess noise versus multiplication at different wavelengths for the P1 and N1

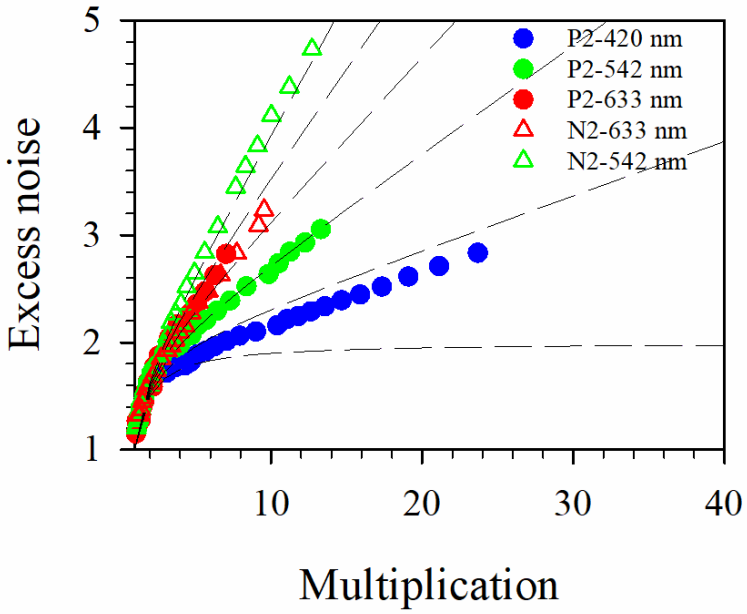

Figure 6.5. Measured excess noise versus multiplication at different wavelengths for the P2 and N2.

6.3 Discussion

6.3.1 Excess noise simulation

Figure 6.6(a) shows that the measured F_e results at $M \approx 10$ are in agreement with AlAsSb ionization coefficients and McIntyre's model for P1–P3 structures, suggesting that the excess noise behaviour is dominated by β/α in AlAsSb avalanche regions >660 nm, but is reduced by dead-space effects for the two thinnest structures. The black dash line shows the simulated excess noise by RPL. In Chapter 5, we simulated multiplication for a 6 μm thick structure and found that holes hardly ionize at the low electric fields. We undertook a Local Model analysis for the same structure for excess noise, as shown in Figure 6.6(b). It suggests that the excess noise of 6 μm demonstrates an extremely low effective k value of 0 due to the very small β/α ratio. and it is also not comparable with measured excess noise from InAs that is truly single-carrier multiplication material. This may be due to without "dead-space" effect. Furthermore, the thickness of 6 μm introduces an operating voltage of ~200 V.

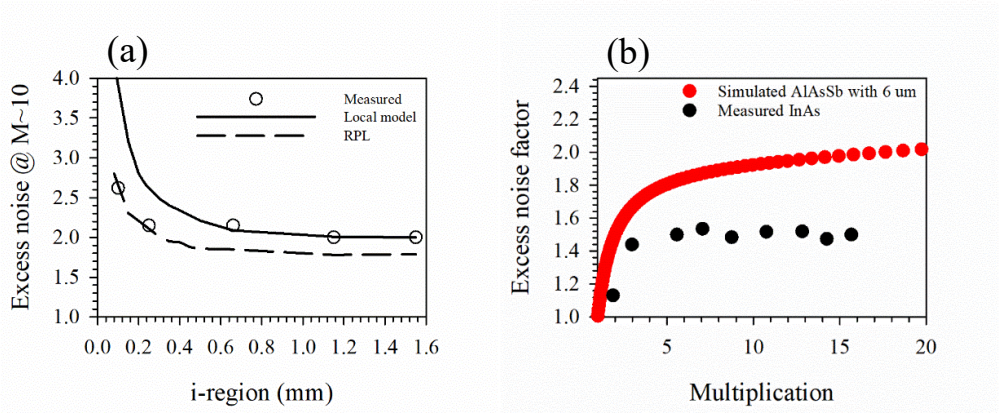

Figure 6.6. (a) Measured and simulated excess noise (at $M \approx 10$) versus avalanche width for AlAsSb p-i-n with pure illumination. (b) Excess noise versus avalanche multiplication for AlAsSb and InAs [17].

6.3.2 Mixed excess noise simulation

The lowest measured excess noise is observed in P1 under illumination of 420 nm light, because of the small value of k and primary electrons diffusing to the appropriate edge of the multiplication region, resulting in a chain of impact ionization events. This was predicted by McIntyre [15]. In reality, even if we use short wavelength light source and

a small size light spot as in this work, some primary carriers are generated in the multiplication layer and even in the bottom cladding layer due to photons being absorbed in these regions. Side injection is another example of mixed carrier injection, especially in materials with a small value of *k* as experimentally shown in InAs previously [17].

Recently, Hayat M.M. reported an easy-to-use exact analytical formal for mixed carrier injection, taking into account the photon absorption profile. More details can be found in Ref. [18]. Here, we firstly look at the case of delta injection. The analytical expression of multiplication as a function of position, $M(x)$, is expressed as

$$M(x) = \frac{(1-k)e^{-(1-k)(\alpha w)(\frac{x}{w})}}{e^{-(1-k)(\alpha w)} - k} \qquad (6.1)$$

Where w is the avalanche thickness, k is β/α ratio when $\beta<\alpha$, and x is position within the multiplication region where a primary pair of electron-hole is generated. Equation (6.1) can be rewritten for electron injection ($x = 0$) and hole injection ($x = w$) as;

$$M(0) = \frac{r}{r + \alpha - \alpha e^{rw}} \qquad (6.2.a)$$

$$M(w) = \frac{re^{rw}}{r + \alpha - \alpha e^{rw}} \qquad (6.2.b)$$

Then, the mixed-injection excess-noise factor F is

$$F(x) = kM(x)e^{2(1-k)(\alpha w)(\frac{x}{w})} + 2(1 - ke^{(1-k)(\alpha w)(\frac{x}{w})}) - \frac{1}{M(x)}(1-k) \qquad (6.3)$$

We define the general case of excess noise when carriers are created in p^+, i and n^+ region as [19]

$$F_t = \frac{N_{total}}{N_{shot}} = \frac{A_p M(0)^2 F(0) + A_n M(w)^2 F(w) + \int_0^w M(x)^2 F(x) A_0 \gamma \exp(-\gamma X_p) \exp(-\gamma x) dx}{M_t^2 A_{gen}} \qquad (6.4)$$

Where $r = (\beta-\alpha)$, A_p, A_0 and A_n are the rate of electrons and holes generation per unit volume in the p^+ region, i-region and n^+ region, A_{gen} is the total primary carrier generation, M_t is the total mean multiplication, and γ is the absorption coefficient. Figure 6.7 shows an example of excess noise under delta injection assuming k of 0.0001 and w of 1 μm. In Figure 6.7 black symbols show the F against M when one electron-hole pair is generated at 0%w (F_e), 50%w and 100%w (F_h). Numerically, we then looked at when we had 2 electron-hole pairs created simultaneously at 0%w and 100%w shown as black solid line, at when we had 3 electron-hole pairs created simultaneously at 0, 50%w and 100%w shown as black solid line, at when we had 5 electron-hole pairs created simultaneously at 0%w, 25%w, 50%w, 75%w and 100%w shown as red solid line, at when we had 21 electron-hole pairs created at 0, 5%w, 10%w, ……, 90%w, 95%w and 100%w shown as solid blue line. It is interesting to see the F when we had 21 pairs is similar as with 5 pairs at low gain. We repeat this analysis in AlAsSb using previously determined ionization coefficients and w of 1.5 μm. To simplify the calculation, we used a constant k value of 0.0001, and the results are showing in Figure 6.8, together with measured results. It suggests that excess noise using uniformly distributed 21 points delta injection profile (dotted black line) is higher than those measured (symbols). It is because more carriers are generated in the first half of the structure, and excess noise is closer to the case of electron injection. As we adjust the ratio of F_e and F, the dashed blue lines are possibly agreed well with measured results.

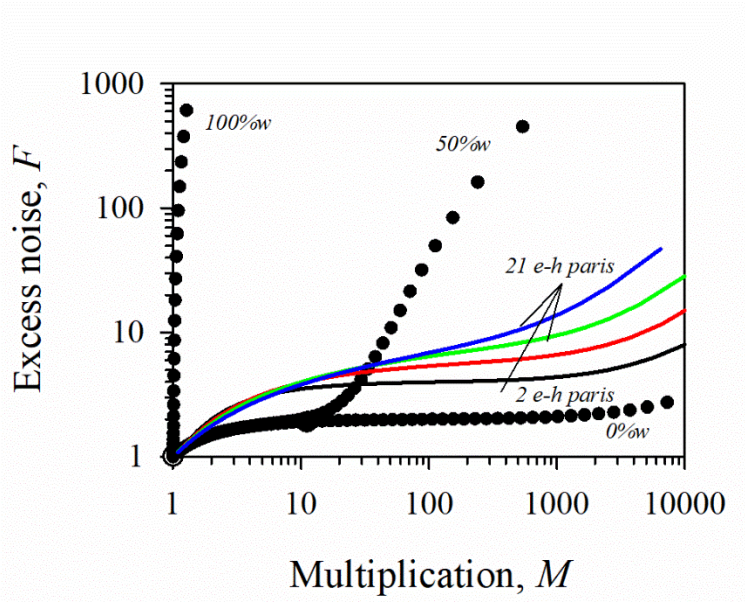

Figure 6.7. Pure and mixed-injection *M* versus *F* for the cases where the k is 0.0001. Symbols are delta injection at position w = 0%*w*, 50%*w*, 100%*w* and lines are distribution injection.

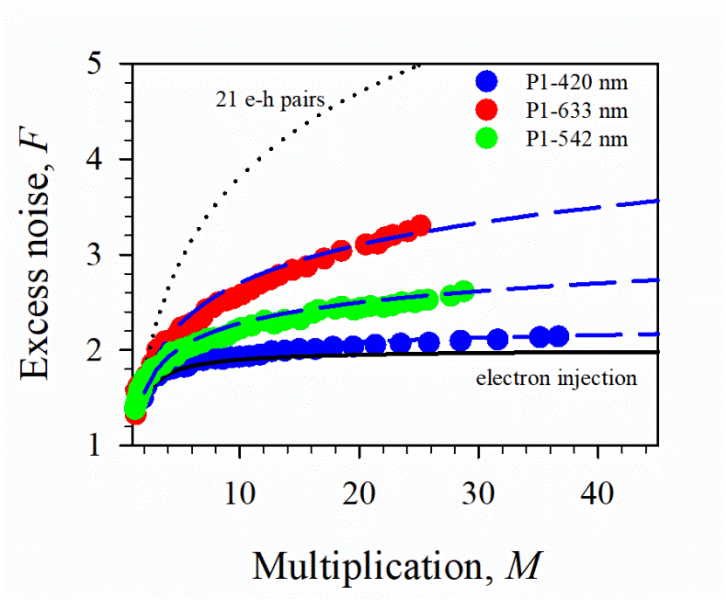

Figure 6.8. Excess noise fitting of P1. Symbols are measured excess noise on P1, and dashed blue lines are distribution injection after adjusting the ratios.

Excess noise for mixed-injection using delta injection profile shows a comparable fitting, but it has a finite uncontinuous number of carrier injection points. In reality, photogenerated carriers can be everywhere in the avalanche region. In the following section, we look at mixed-injection *M* and *F* with an exponential decay function. Considering

an incident photon that is absorbed in the multiplication region ($0 \le x \le w$) with probability P_m. The probability that an incident photon is absorbed in the depletion region is calculated by

$$C\int_0^w e^{-Ax}dx = P_m = 1 \qquad (6.5)$$

Where C is a constant chosen and is evaluated as

$$C = \frac{-A}{e^{-Aw}-1} \qquad (6.6)$$

Figure 6.9 shows the probability distribution function of absorption location as a function of absorption depth (x) using different values of absorption. A normalized absorption coefficient representing relative mixed injection parameter with the values of 0.01, 1, 5, 10, and 5000, respectively and described in more detail in Ref [18]. This shows the exponential absorption profiles from steep to flat. We can quantitatively do a comparison with the measured results under different wavelength illumination.

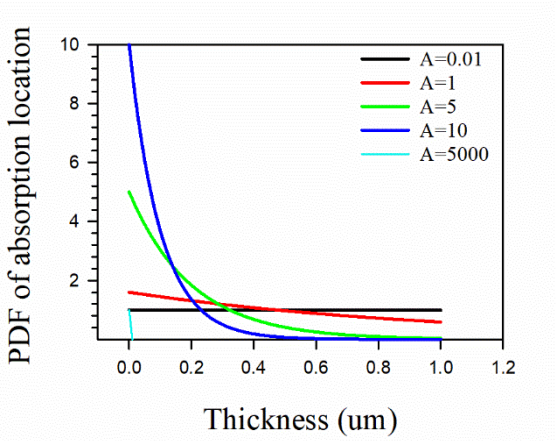

Figure 6.9. The probability density function of the photon absorption location as a function of the absorption location for different absorption coefficient from flat to narrow with an exponential decay function.

According to Ref. [18], the multiplication and excess noise can be express as

$$M(x) = \frac{-(1-k)(\gamma w)(e^{-(1-k)(\alpha w)-(\gamma w)}-1)}{(e^{-(1-k)(\alpha w)}-k)(e^{-(\gamma w)}-1)(-(1-k)(\alpha w)-(\gamma w))} \qquad (6.7)$$

and

$$F(x) = \frac{\left(\frac{-(\gamma w)}{e^{-\emptyset w}-1}\right)\times\left[\left\{\frac{2(e^{(-2(1-k)(\alpha w)-(\gamma w))}-1)}{(-2(1-k)(\alpha w)-(\gamma w))}\right\}-\left\{\frac{e^{-2(1-k)(\alpha w)}-k}{e^{-(1-k)(\alpha w)}-k}\right\}\left\{\frac{(e^{(-(1-k)(\alpha w)-(\gamma w))}-1)}{(-(1-k)(\alpha w)-(\gamma w))}\right\}\right]}{\left\{\left(\frac{-(\gamma w)}{e^{-\gamma w}-1}\right)\times\frac{(e^{(-(1-k)(\alpha w)-(\gamma w))}-1)}{(-(1-k)(\alpha w)-(\gamma w))}\right\}^2} \quad (6.8)$$

The simulated $F(x)$ as a function of $M(x)$ is shown in Figure 6.10. Here, six cases of k and five cases of relative mixed-injection parameter are simulated. We considered 1 μm p-i-n and n-i-p structures with k values of, 0.1, 0.01, 0.001, 0.0001, 0.02 and 0.05, and with A values of 0.01, 1, 5, 10, and 5000. It suggests that the excess noise shows absorption dependence, and as expected, the lowest excess noise is for a material with a small value of k and with edge electron-injection (solid cyan lines), while the dashed cyan lines present excess noise under edge hole-injection. And the excess noise is comparable between p-i-n and n-i-p structures under a nearly flat carrier generation profile of A = 0.01 (black colour). We also observe that the excess noise shows a dramatic increase under mixed injection with reducing k values. It turns out that mixed injection plays a significant role in the performance of $F(x)$ as a function of $M(x)$ as well as the injection location and k values. Furthermore, for any k value, the shape of the mixed-injection F versus the multiplication is very different from what the McIntyre formula predicts for pure injection. Based on AlAsSb ionization coefficient analysis in the previous chapter, we determined an effective k value of 0.02-0.05 for a 1 μm p-i-n structure. The predicted excess noise under pure injection profile (A = 5000) is similar to those of measurement but the predicted excess noise under mixed injection profile (A = 10, 5, 1 and 0.01) does not agreed with those of measurements, as shown in Figure 6.10 using k of 0.02 and 0.05. This may be explained by even smaller β/α ratio, "dead-space" effects or a different electric field profile.

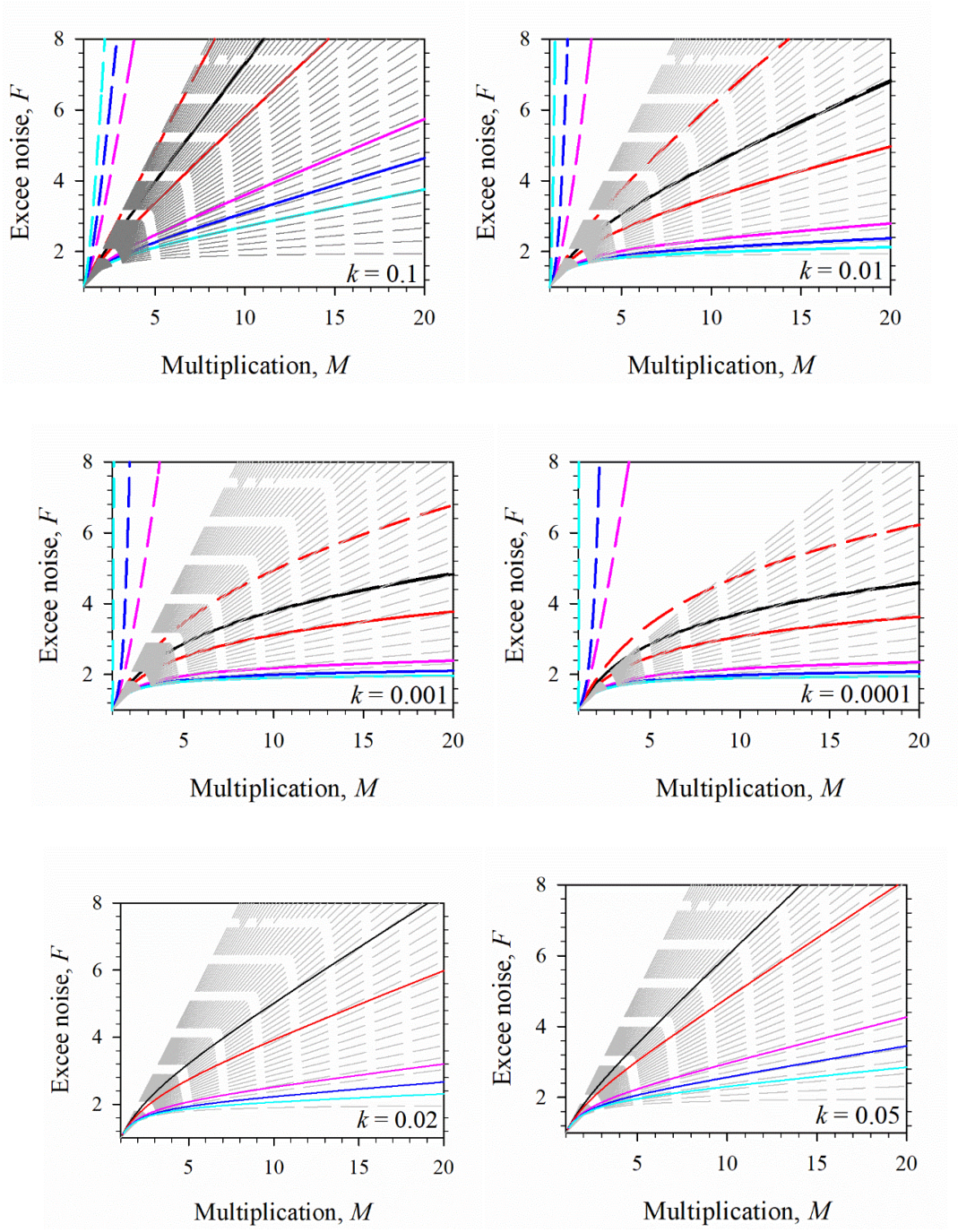

Figure 6.10. Mixed-injection excess noise versus multiplication for different absorption profiles and *k* values. Gray dashed lines are MCT predict excess noise from 0 in step of 0.02.

Figure 6.11 presents the simulated excess noise results on P1 assuming light is absorbed with different exponential decay function (shown by solid lines). The blue, green and red circles show the measured excess noise from P1 using different wavelengths, and is also show the delta function injection at x = 0%w and distributed 21 points delta

injection by black open square. Two different assumptions predict similar excess noise characterise. Interestingly, the predicted excess noise utilizing A = 10 and A = 5 shows comparable results as measured results, however, it is hard to find a value of absorption to fit results under illumination of 633 nm. This maybe due to more light being absorbed in the front half of the structure.

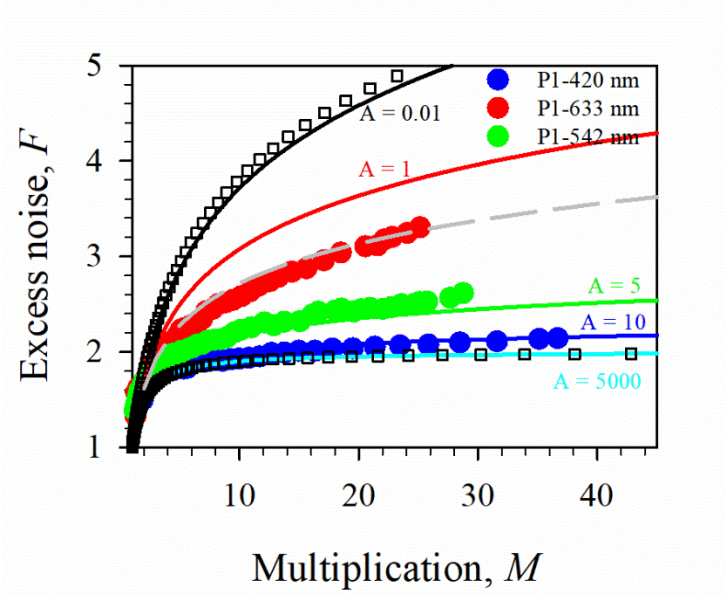

Figure 6.11. Mixed-injection excess noise versus multiplication of P1 for different absorption profiles. Black symbols show mixed-injection excess noise used delta injection profile of one pair generate at 0%w and 21 pairs. Solid color lines show the simulated excess noise results with different exponential decay function.

6.3.3 Comparison with other avalanche materials

The excess noise results are in good agreement with the ionization coefficient analysis discussed in Chapter 5. The small β/α ratios introduce an extremely low excess noise as expected. To further emphasise how much smaller the measured F_e in AlAsSb is compared to traditional III-V materials and silicon, Figure 6.12 presents the F_e of AlAsSb, together with those of some other III-V materials and silicon as a function of multiplication. The F_e measured in 100 nm thick and 2500 nm thick InAlAs [20], currently the best lattice-matched avalanche material for InP based telecommunication APDs, correspond to k~0.2. Compared with AlAsSb, the excess noise factor of InAlAs is high and keep increasing with increasing multiplication. It suggests that AlAsSb is definitely better than InAlAs as a multiplication material grown lattice-matched to InP substrates. It can replace it for next-generation high-speed and high-sensitivity SAM-

APDs used in telecommunication applications. Commercially available silicon APDs have been reported with similar excess noise characteristics, but this requires very thick structures with high operating voltages [21]. Interestingly, bulk $In_{1-x}Al_xAs_{1-y}Sb_y$ on GaSb shows similar extremely low excess noise. The best reported excess noise was *k* of 0.01 in $Al_{0.5}In_{0.5}As_ySb_{1-y}$ with nominal i-region of 890 nm which is comparable with AlAsSb with 1.15 μm. Compared with other materials, AlAsSb can work at a higher gain, *M* of 40-50, with extremely low excess noise.

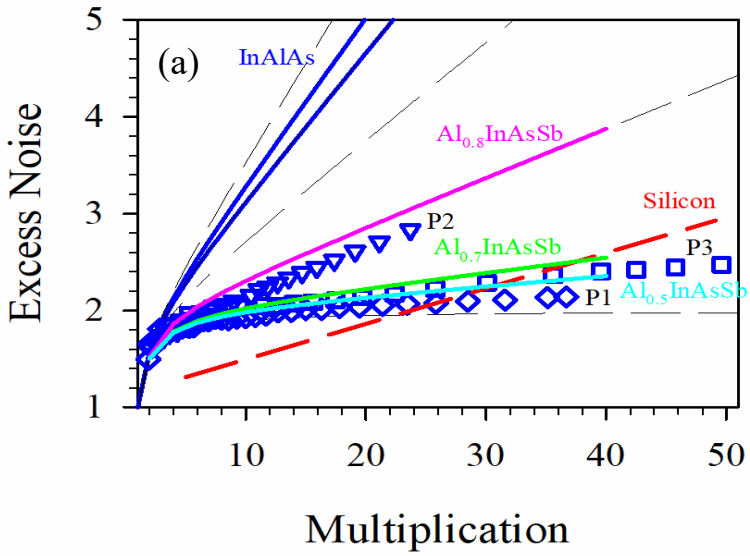

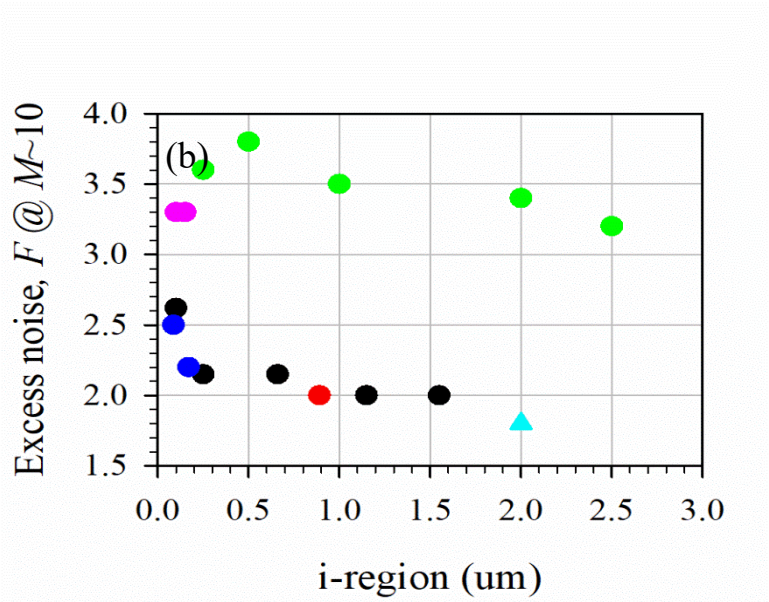

Figure 6.12. (a) A comparison of measured excess noise. (b) Measured excess noise at the multiplication of 10. Black-AlAsSb, blue-AlGaAsSb, red-AlInAsSb, cyan-InAs, pink-Si, and green-InAlAs.

6.3.4 A signal-to-noise ratio analysis

So far, we have provided convincing experimental evidence of very small *k* value in thick AlAsSb diodes, and an analysis of the potential benefits of adopting it in high-speed APDs is given below. The simplest way to estimate the benefits of this new multiplier region is by undertaking a signal-to-noise ratio (SNR) analysis as described in Chapter 2. From Equation (2.34), there are some factors such as dark current, photo-responsivity, trans-impedance amplifier (TIA) noise and bandwidth. The assumption is summarized in Table 6.1. In here, we look at two different operating speeds, 2.5 Gb/s used for LiDAR applications and 25 Gb/s used for high-speed optical communication applications. Figure 6.13 and 6.14 show the SNR of AlAsSb achievable with a 1.55 μm thick avalanche region, together compared with InAlAs APDs. The model suggests that compared with InAlAs APDs the measured high surface dark current gives a lower SNR performance at 2.5 Gb/s, however, SNR results at 25 Gb/s shows better performance even with a high surface dark current. This is due to the benefit of low excess noise. As expect, AlAsSb APDs under ideal dark current condition shows much better SNR performance than those of InAlAs APDs.

Table 6.1. Parameters used in SNR analysis.

		Is (μA)	*Ib* (nA)		TIA	Bandwidth	*k*
AlAsSb APD	Ideal	0	1	2.5 Gb/s	6.6 pA/Hz^2	1.75 GHz	0.005
	Real	1.75	16	25 Gb/s	35 pA/Hz^2	18 GHz	
InAlAs APD	Ideal	0	1	2.5 Gb/s	6.6 pA/Hz^2	1.75 GHz	0.2
	Real	0.02	1.6	25 Gb/s	35 pA/Hz^2	18 GHz	

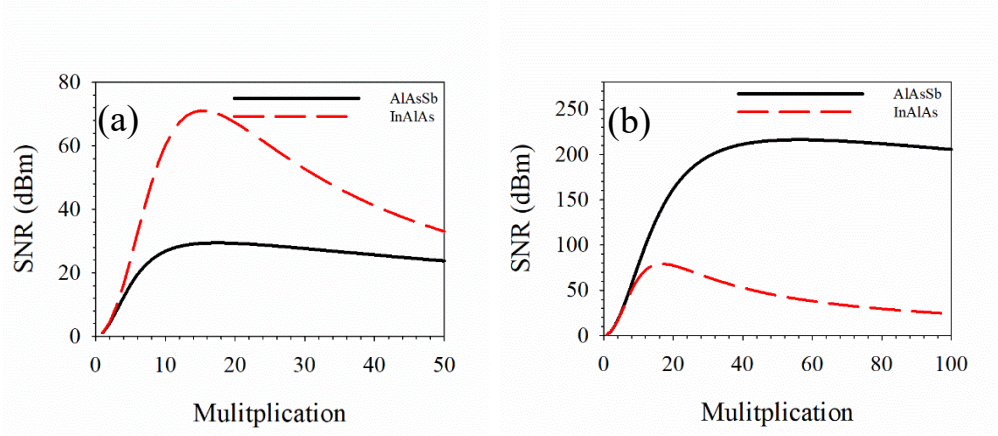

Figure 6.13. Prediction of SNR for AlAsSb and InAlAs at 2.5 Gb/s. (a) Used real dark current parameter. (b) Used ideal dark current parameter.

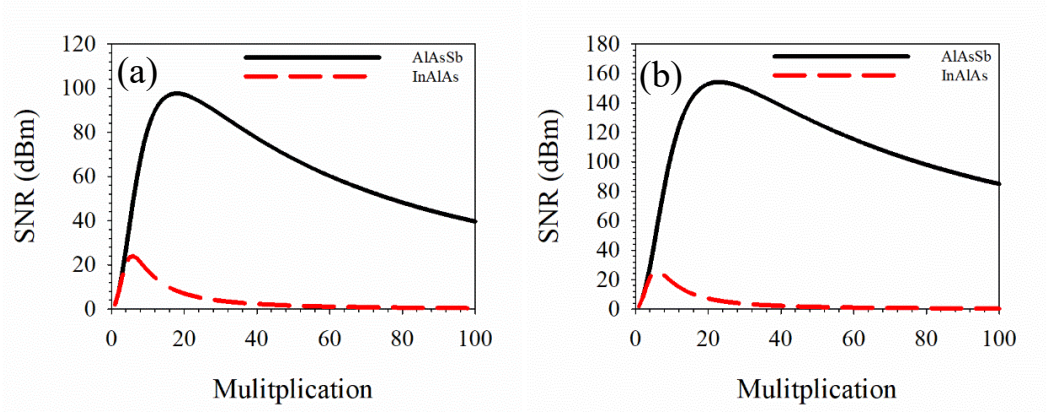

Figure 6.14. Prediction of SNR for AlAsSb and InAsAs at 25 Gb/s. (a) Used real dark current parameter. (b) Used ideal dark current parameter.

6.3.5 A full bandwidth and sensitivity analysis

In this section, we theoretically estimate the potential benefits of adopting AlAsSb in a typical high-speed SAM-APD by undertaking a full bandwidth and sensitivity analysis on a number of design structures. Such a model is sensitive to the exact parameters used, so we have been relatively conservative in the assumptions of carrier velocity, dark current and the following trans-impedance amplifier (TIA) noise, the values of which are given in the Appendix I. These structures have different thicknesses of AlAsSb multiplication regions, w_m, and the combined thicknesses of undoped InGaAs absorber, field control and grading layers, w_1. A Maximised-induced current (MIC) Ref. [6] absorber design (described in Appendix I) can provide a responsivity of 0.92 A/W at 1550 nm and a responsivity of 0.69 A/W at 1310 nm while minimising the InGaAs absorber thickness. Carriers are created in the InGaAs layer according to the Beer-Lambert law after which they drift to the avalanche multiplication region. A RPL model was used to simulate the impact ionisation process within the multiplication region using ionisation path length probability distribution functions determined by experimental electron and hole ionisation coefficients. With 50000 trials, we can obtain statistically accurate $M = \langle M_{trial} \rangle$ and $F = \langle M_{trial}^2 \rangle / \langle M_{trial} \rangle^2$ as a function of reverse bias. Assuming values of 1×10^5 m/s and 6.65×10^4 m/s for the electron and hole drift velocity respectively and using Ramo's theorem [22] we can also obtain the mean current impulse response (see Figure 6.15(a)). Fourier Transforming this mean current impulse response allows us to obtain the bandwidth (f_{3dB}) from the -3 dB point in the frequency response (see Figure (b)). Figure 6.15(c) shows the theoretically predicted GBP for AlAsSb APDs and measurement on an InGaAs/$Al_{0.85}Ga_{0.15}$AsSb structure. We undertook a similar GBP calculation for InAlAs APDs utilising the ionisation coefficients of InAlAs [20] and compared that to experimentally measured results from the literature [2, 23-25]. The significantly larger GBP for AlAsSb APDs can be clearly seen, and no significant improvement occurs for multiplication regions below 600 nm as the k value starts to increase. The sensitivity at a BER of 10^{-12} and an extinction ratio of 10 dB was calculated as described by Agrawal [26] and Ong et al. [27]. The receiver signal was determined by the average input optical power, P, and the diode responsivity, R. The total system noise was determined by the sum of noise power from the APD and the commercial TIA noise as described in the Appendix I. Figure 6.15 shows the sensitivity achievable with different w_1 at a wavelength of 1.55 μm or 1.31 μm and w_m of

1.5 μm, 1 μm and 0.6 μm for a BER of 1×10^{-12}. Figure 6.15(d) shows the best sensitivity and speeds based on Si/Ge and InGaAs/InAlAs APDs that have been reported in the literature compared to the simulations in Figure 6.15(d). The modelled results in Figure 6.15(d) suggest that even with 0.6 μm of w_m, we can operate the device at 1550 nm at 25 Gb/s with a sensitivity of -25.7 dBm as we can utilise a multiplication of ~9. By operating at 1.31 μm with a thinner absorption layer, we can potentially operate in normal incidence with 0.6 μm of wm at 40 Gb/s with a -20 dBm sensitivity and even at 50 Gb/s with a -15 dBm sensitivity. The predicted performance for the 2.5 and 10 Gb/s devices here are limited by the device surface dark currents and the TIA noise assumed, rather than factors such as the avalanche build-up time or the avalanche excess noise. In all cases, the significantly smaller *k* of AlAsSb compared to InAlAs enables a larger multiplication to be achieved before the speed is limited thereby improving the sensitivity.

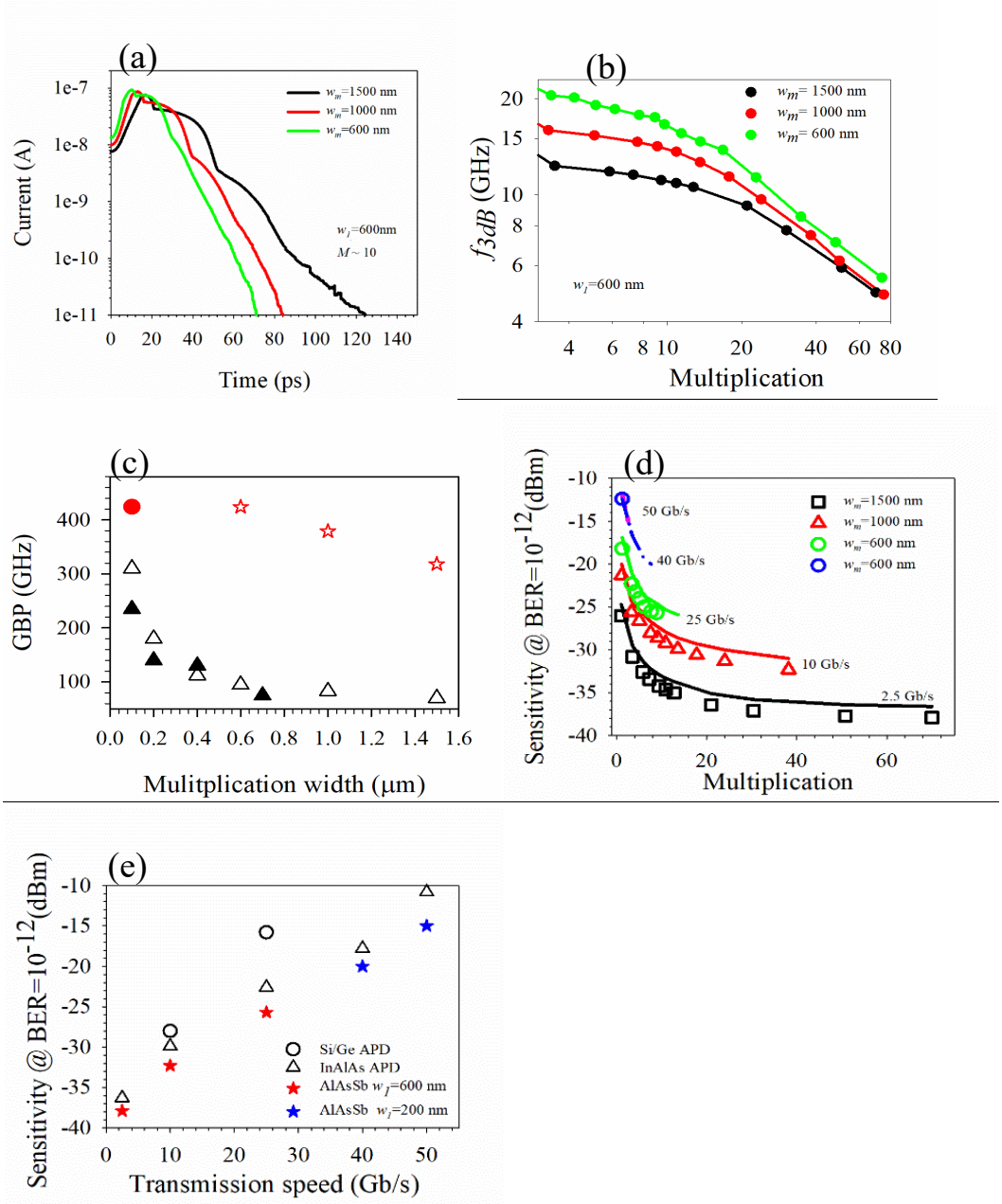

Figure 6.15. Optical sensitivity modelling. (a) The calculated mean current impulse response at M = ~10. (b) The predicted f_{3dB} versus M for AlAsSb/InGaAs APD characteristics as a function of w_m. (c) The predicted GBP for AlAsSb APD (red star), and InAlAs APD (open triangle). The measured GBPs for InAlAs APD are also included for comparison (closed triangle) as is the measured GBP for $Al_{0.85}Ga_{0.15}As_{0.56}Sb_{0.44}$ (closed circle). (d) InGaAs/AlAsSb APD sensitivity with w_1 = 200 nm (lines) and 600 nm (symbols) for different w_m were simulated at 1550 nm (2.5, 10 and 25 Gb/s) and 1310 nm (40 and 50 Gb/s). (e) The sensitivity potentially achievable in InGaAs/$AlAs_{0.56}Sb_{0.44}$ based APDs with w_1 = 0.2 μm and 0.6 μm compared with Si/Ge and InGaAs/InAlAs APDs. The reported InGaAs/InAlAs APDs at 25 and 50 Gb/s operated at 1.31 μm. The 40 Gb/s InGaAs/InAlAs APD result is for a waveguide structure while others are normal incidence structures.

6.4 Conclusion

The avalanche excess noise characteristics of thick AlAsSb APDs with w from 0.6 – 1.5 μm were symmetrically investigated using 420, 542 and 633 nm light at room temperature. The multiplication and excess noise results show a strong wavelength dependence. The multiplication characteristics obtained using shorter wavelength light from the p-i-n structure are always higher than those of longer wavelengths. And the excess noise results measured using shorter wavelength light from the p-i-n structure are always lower than those obtained using longer wavelengths. Very high excess noise results were measured on the n-i-p structures. The lowest measured excess noise corresponding to k as low as 0.005 is close to the theoretical minimum, exceeding the performance of all materials lattice-matched to InP and even silicon. These results suggest unambiguously that α is much larger than β deduced from the previous chapter.

The mixed-injection excess noise characteristics were simulated using an analytic formula, taking into account distribution of carrier injection profile. A small difference between the measured and modelled excess noise suggests that the absorption profile may be different. There is close an agreement between measured and modelled excess noise results at least qualitatively and the difference can be attributed uncertainty absorption profiles and minority carry diffusion length.

A full bandwidth and sensitivity model suggests that vertically illuminated AlAsSb APDs with a sensitivity of -25.7 dBm at a bit-error-rate (BER) of 1×10^{-12} at 25 Gb/s at 1.55 μm can be realised. The devices are limited by dark current and TIA noise, rather than factors such as the avalanche build-up time or the avalanche excess noise. This extremely low excess noise changes the paradigm whereby high-speed APDs always use very thin avalanching structures to one where both high speed and sensitivity can be achieved with thicker avalanching structures. The findings could yield a new breed of high-performance receivers for applications in networking and sensing. The advantage of adopting AlAsSb in a high-speed and high-sensitive APD must be balanced by the technical challenges in the growth using DA technology; The material system is prone to oxidizing very easily when exposed to air, consequently passivation of the

devices is necessary; band discontinuity between InGaAs and AlAsSb and surface issues.

6.5 References

[1] Campbell J. C. et al, “Recent advances in avalanche photodiodes,” IEEE J. Sel. Top. Quantum Electron. Vol. 10, pp. 777–787, 2004.

[2] M. Nada, Y. Muramoto, Y., H. Yokoyama, T. Ishibashi & S. Kodama, “InAlAs APD with high multiplied responsivity-bandwidth product (MR-bandwidth product) of 168 A/W GHz for 25 Gbit/s high-speed operations,” Electron. Lett. Vol. 48, pp. 397–399 2012.

[3] M. Nada, , T. Yoshimatsu, , Y. Muramoto, , H. Yokoyama, & H. Matsuzaki, “Design and performance of high-speed avalanche photodiodes for 100-Gb/s systems and beyond,” J. Lightwave Technol. Vol. 33, pp. 984–990, 2015.

[4] T. Yoshimatsu, et al. “Compact and high-sensitivity 100-Gb/s (4 × 25 Gb/s) APD-ROSA with a LAN-WDM PLC demultiplexer,” Opt. Express. Vol. 20, pp. B393–B398, 2012.

[5] S. Shimizu, , K. Shiba, , T. Nakata, , K. Kasahara, & K. Makita “40 Gbit/s waveguide avalanche photodiode with p-type absorption layer and thin InAlAs multiplication layer,” Electron. Lett. Vol. 43, pp. 476–477, 2007.

[6] M. Nada, et al. “50-Gbit/s vertical illumination avalanche photodiode for 400-Gbit/s ethernet systems,” Opt. Express, Vol. 22, pp. 14681–14687, 2014.

[7] Y. Kang, et al. “Monolithic germanium/silicon avalanche photodiodes with 340 GHz gain–bandwidth product,” Nat. Photon. Vol. 3, pp. 59–63, 2009.

[8] J. Michel, , J. Liu, & C. Kimerling, “High-performance Ge-on-Si photometers,” Nat. Photon. Vol. 4, pp. 527–534, 2010.

[9] Z. Huang, et al. “25 Gbps low-voltage waveguide Si–Ge avalanche photodiode,” Optica Vol. 8, pp. 793–798, 2016.

[10] A. C. Farrell, et al. “Plasmonic field confinement for separate absorption–multiplication in InGaAs nanopillar avalanche photodiodes,” Sci. Rep. Vol. 5, pp. 17580, 2015.

[11] S. R. Bank, et al. “Avalanche photodiodes based on the AlInAsSb materials system,” IEEE J. Sel. Top. Quantum Electron. Vol. 24, pp. 3800407, 2018.

[12] M. E. Woodson, et al.” Low noise AlInAsSb avalanche photodiode,” Appl. Phys. Lett. Vol. 108, pp. 081102, 2016.

[13] A. Rockwell, et al. “Al0.8In0.2As0.23Sb0.77 avalanche photodiodes,” IEEE Photon. Technol. Lett. Vol. 30, pp. 1048–1051, 2018.

[14] A. R. J. Marshall, , P. J. Ker, , A. Krysa, , J. P. R. David, & C. H. Tan, “High speed InAs electron avalanche photodiodes overcome the conventional gain–bandwidth product limit,” Opt. Express. Vol. 23, pp. 23341–23349, 2011.

[15] R. J. McIntyre, “Multiplication noise in avalanche photodiodes,” IEEE Trans. Electron Devices, Vol. 13, no. 1, pp. 164–168, Jan. 1966.

[16] Thorlabs, Fiber-Coupled LED, M420F2. (2017) [Online].

[17] A.R.J. Marshall, C.H. Tan, M. J. Steer, and J.P.R. David, “Extremely low excess noise in InAs electron avalanche photodiodes,” IEEE Photon. Tech. Lett., Vol. 21, no. 13, July 2009.

[18] M. M. Hossain, J.P.R. David, and M.M. Hayat, “Exact Analytical Formula for the Excess Noise Factor for Mixed Carrier Injection Avalanche Photodiodes,” J. of Lightwave Tech., Vol. 37, no. 13, pp. 3315-3323, 2019.

[19] A.R.Pauchard, P.Besse and R.S.Popovic, “Dead space effect on the wavelength dependence of gain and noise in avalanche photodiodes,” IEEE Transactions on Electron Devices, Vol. 47, No.9, p.1685-1693, 2000.

[20] Y. L. Goh, et al. “Excess avalanche noise in In0.52Al0.48As,” IEEE J. Quantum Electron. Vol. 43, pp. 503–507, 2007.

[21] Produce Datasheet: Si APD (S10341 series) https://www.hamamatsu.com/ resources/pdf/ssd/s10341_series_kapd1030e.pdf (Hamamatsu).

[22] S. Ramo, “Currents induced by electron motion,” Proc. IRE. Vol. 27, pp. 584–585 1939.

[23] A. Rouvie., et al. “High gain × bandwidth product over 140 GHz planar junction AlInAs avalanche photodiodes,” IEEE Photon. Technol. Lett. Vol. 20, pp. 455–457, 2008.

[24] Li, N. et al. InGaAs/InAlAs avalanche photodiode with undepleted absorber. Appl. Phys. Lett. 82, 2175–2177 (2003).

[25] M. Hayashi, et al. “Microlens-integrated large-area InAlGaAs–InAlAs superlattice APDs for eye-safety 1.5 μm wavelength optical measurement use,” IEEE Photon. Technol. Lett. Vol. 10, pp. 576–578, 1998.

[26] G. P. Agrawal, “Fiber-Optic Communication Systems,” 3rd edn, Ch. 4 (Wiley, 2002).

[27] D.S.G. Ong et al. “Optimisation of InP APDs for high-speed lightwave systems,” J. Lightwave Technol. Vol. 27, pp. 3294–3302, 2009.

CHAPTER 7:

CONCLUSIONS AND FUTURE PLANS

7.1 Conclusions

The photoresponse of AlAsSb under low reverse bias has been studied symmetrically using a series of p-i-n and n-i-p diodes. The peak response is about 570 nm in these new wafers by DA technology used MBE. By measuring bias-dependence in photocurrent as a function of wavelength, the minority carrier diffusion lengths have been extracted. The absorption coefficients of AlAsSb has been extracted by a 1D photocurrent model based on the measurements of bias-dependence of the photoresponse. The simulated quantum efficiency is fitted well with the experiment data covering 4 orders of magnitude. The band energy in Γ and X valleys were extracted from the absorption coefficients and are similar to the values from the literature.

The avalanche multiplication in AlAsSb has been invested in detail using a series of p-i-n and n-i-p diodes with nominal i-region widths of 0.1 – 1.5 μm. From these, the local values of α and β were extracted from the pure carrier multiplication results and parametrized over an electric-field range from 220-1250 kV/cm for α and from 360-1250 kV/cm for β. These parameterized ionization coefficients are capable of reproducing the measured multiplication results down to M~0.01, taking into consideration its real electric-field profile using a local model and ignoring any dead-space effects. Like most other materials, the α/β ratio of AlAsSb are found to differ at low electric-field but converge at high electric-field, and more excitingly is found to much larger than any other wide band-gap III-V semiconductor material with values of >100 for electric fields below 460 kV/cm. This makes AlAsSb ideal for the multiplication region in InP based telecommunication SAM-APDs. Furthermore, we have studied the avalanche breakdown of AlAsSb in detail. We for the first time prove that the traditional method of extrapolating $1/M$, used to estimate breakdown voltage is no longer reliable in large α/β ratio material.

The excess noise measured by electron initial avalanche process in thick AlAsSb diodes are a reasonable agreement with McIntyre's local model and the excess noise measured

by mixed carrier initial avalanche process are in qualitative agreement with Hayat's analytical equation. As a result of the large α/β ratio at low electric fields, the thickest p-i-n structure shows extremely low excess noise with k value of 0.005, which is the lowest excess noise InP based III-V APD reported to date, and even comparable to silicon. The potential benefits of adopting AlAsSb in high-speed APDs was analysed by undertaking a signal-to-noise ratio analysis and a full bandwidth and sensitivity analysis. The significant sensitivity improvement is attributed to the low excess noise.

7.2 Other ongoing work

Further work relevant to this thesis has also been undertaken. Since it is not yet fully completed and published, it is not shown in the main body of the thesis but is summarised briefly below.

APDs have to be operated over a wide range of ambient temperatures. As impact ionization process is strongly dependent on junction temperature, this affects the gain for a fixed reverse bias and the breakdown voltage of the APD. Temperature coefficient of the breakdown voltage, $C_{bd} = \Delta V_{bd} / \Delta T$, is a significant parameter for an APD for indicating how sensitive the multiplication gain to the temperature. Earlier works on $Al_xGa_{1-x}AsSb$ have shown that the temperature dependence of breakdown voltage is extremely small. Here we expanded the work to thick structures using the diodes introduced in Chapter 4 covering 200 K – 373 K. From the temperature-dependence of the photoresponse, we extracted the bandgap at different temperatures. Photomultiplication measurements were performed as a function of reverse bias using different wavelength light. From these measurements, we extracted the impact ionization coefficients using the Local Model from 200 to 373 K, suggesting that electrons are the largerionizing carrier type compared to holes in this material. The temperature coefficient of breakdown voltage with an i-region of 1 μm is ~8 mV/K, much lower than the value reported in silicon [1], which suggest that even thicker AlAsSb avalanche multiplication can be used for temperature-insensitive InP-based APDs.

7.3 Suggestions for further work

1) To complete the impact ionization study on AlGaAsSb lattice-matched on InP substrates alloy system, several new layers have to be grown and measured. Several reports showed that $Al_{0.85}Ga_{0.15}AsSb$ homojunction structures demonstrated similar low excess nose behaviours to those of AlAsSb and better dark current performance. However, thin i-region may still dominate low excess noise performance. It would be interesting to investigate multiplication and excess noise performance in $Al_xGa_{1-x}AsSb$ ($0< x <1$) with thicker i-region (~1.5 μm). The lower Al content quaternary alloy also improve long-term device stability.

2) It would be interesting to demonstrate the first planer AlAsSb-based APD. Recently, InGaAs-InP [2] and InGaAs-InAlAs [3] have developed planar configuration and proved that the planar-structure APDs have higher reliability than the mesa-structure APDs

3) The final objective of characterisation of AlGaAsSb is to design a comprehensive SAM-APD with high gain-bandwidth, high detection efficiency and low noise operated at 1.31 and/or 1.55 μm. The absorption, grading and avalanche layers for optimisation of thickness, composition and doping will be determined. A possible device structure incorporating a SAM structure is shown in Figure 7.1.

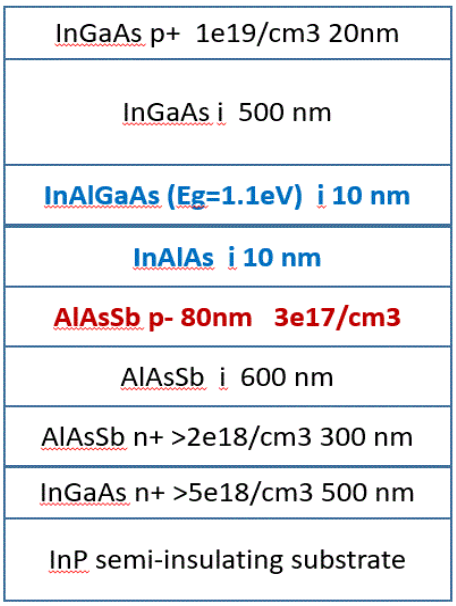

Figure 7.1. AlAsSb-based SAM-APD structure.

7.4 References

[1] D.J. Massey, J.P.R. David and G.J. Rees, “Temperature dependence of impact ionization in submicrometer silicon devices,” IEEE Trans. Electron Devices, vol. 53, no. 9, Sep. 2006.

[2] M.A. Itzler, C.S. Wang, S. McCoy, N. Codd, and N. Komba, “Planar bulk InP avalanche photodiode design for 2.5 and 10 Gb/s applications,” in Proc. 24th ECOC, Madrid, Spain, Sep. 20–24, 1998, vol. 1, pp. 59–60, Paper MoB03.

[3] B.F. Levine, R.N. Sacks, J. Ko, M. jazwiecki, J.A. Valdmanis, D. Gunther and J.H. Meier, “A new planar InGaAs-InAlAs avalanche photodiodes,” IEEE Photon. Tech. Lett., vol. 18, no. 18, Swp. 2006

Appendix I

Bandwidth analysis

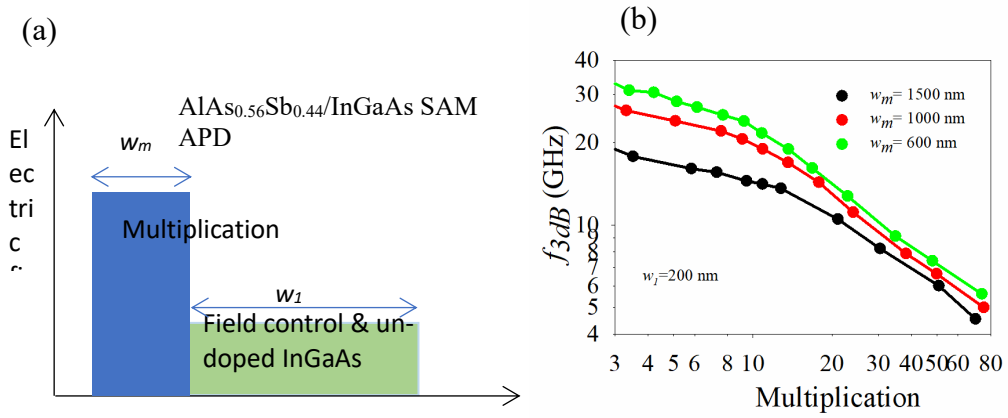

Figure 1. (a) Schematic representation of the APD structures and electric fields used in the model. (b) The predicted f_{3db} versus M for $AlAs_{0.56}Sb_{0.44}$/InGaAs APD as a function of w_m with w_1=200 nm.

A Random Path Length (RPL) model [1] was used to simulate the transit time limited bandwidths of APD structure in Fig. S6.1a. A MIC [2] absorber design was assumed with a 500 nm p-InGaAs and a 500 nm undoped InGaAs for a responsivity of 0.92 A/W at 1550 nm while the undoped InGaAs was reduced to 100 nm to provide a responsivity of 0.69 A/W at 1310 nm. In both designs, a 100nm thickness of grading layer and charge sheet was assumed between the InGaAs and AlAsSb regions [3]. In the RPL model, the position of photogenerated electron-hole pairs in the InGaAs absorber are determined using the Beer-Lambert law and electrons subsequently drift into the avalanche region. The carrier ionization path length probability distribution functions (PDFs) determined by electron and hole ionisation coefficients are used to compute the impact ionization probability in the $AlAs_{0.56}Sb_{0.44}$. With 50000 trails, we can obtain statically accurate $M = \langle M_{trial} \rangle$ and $F = \langle M_{trial}^2 \rangle / \langle M_{trial} \rangle^2$. The impulse current response for each trial is obtained using Ramo's theorem [4], with the avalanche current given by $i = qv/(w_m + w_1)$, where v is carrier drift saturation velocity with the value of $1x10^5$ m/s and $6.65x10^4$ m/s for electrons and holes respectively, and q is the electronic charge. These values are broadly in agreement with the values used to fit the GBP results of AlInAs and $Al_{0.85}Ga_{0.15}AsSb$ [5]. The frequency response was obtained from

the Fourier Transform of the mean current impulse response. The -3 dB point in the frequency response is the bandwidth, f_{3dB}. Fig. S6.1b shows the predicted f_{3db} versus M for $AlAs_{0.56}Sb_{0.44}$/InGaAs APD as a function of w_m with w_1=200 nm.

Table 1. Parameters used in the receiver sensitivity model.

Parameter	Values used
Bit error rate (sec^{-1})	$1x10^{-12}$
Extinction ratio (dB)	10
MIC design: Undoped InGaAs absorber, control and grading layers, w_1, (nm) + p- InGaAs absorber thickness (nm)	200 (w_1) + 500 (p- InGaAs) for 40 and 50 Gb/s at 1310 nm 600 (w_1) + 500 (p- InGaAs) for 2.5, 10 and 25 Gb/s at 1550 nm
Responsivity (A W^{-1})	0.69 (for 40 and 50 Gb/s at 1310 nm) 0.92 (for 2.5, 10, 25 Gb/s at 1550 nm)
$AlAs_{0.56}Sb_{0.44}$ multiplication width, w_m, (nm)	600, 1000 and 1500
APD carrier saturated drift velocity (m s^{-1})	$1x10^5$ for electron $6.65x10^4$ for hole
APD dark current (at D=30 μm) (A)	Surface leakage current I_s : 1.75×10^{-6} Bulk dark current I_b : 1.6×10^{-8}
Minimum APD bandwidth (GHz)	1.75 @2.5 Gb/s system 7 @10 Gb/s system 18 @25 Gb/s system 28 @40 Gb/s system 35 @50 Gb/s system
Input referenced amplifier noise (pA $Hz^{-1/2}$)	6.6 @2.5 Gb/s system [6] 11 @10Gb/s system [7] 15.3 @25 Gb/s system [8] 35 @40 Gb/s system [9] 35 @50 Gb/s system [9]

Appendix II

Table 2. Device parameters of AlAsSb homjunction diodes used in this thesis.

Layer name	Diode type	Nominal i-thickness (μm)	Breakdown voltage V_{bd} (V)		CV Modelled results		Growth technique
			Measured	Modelled fit	i-region doping ($\times 10^{15}$ cm^{-3})	i-region thickness w (μm)	
P1	PIN	1.5	84.5	85.7	5	1.55	DA
N1	NIP	1.5	84.5	86.0	5	1.55	DA
P2	PIN	0.60	40.2	40.4	10	0.66	DA
N2	NIP	0.60	41.5	42.3	10	0.66	DA
P3	PIN	1.00	62.2	63.3	10	1.15	DA
P4	PIN	0.25	20.2	21.2	1	0.23	RA
P5	PIN	0.10	11.2	14.9	1	0.08	RA
P6	PIN	0.10					RA

References

[1] D. S. Ong, et al. “A simple model to determine multiplication and noise in avalanche photodiodes,” Journal of Applied Physics. Vol. 83, pp. 3426, 1998.

[2] M. Nada, et al. “50-Gbit/s vertical illumination avalanche photodiode for 400-Gbit/s ethernet systems ,” Optics Express. Vol. **22**, pp. 14681-14687, 2014.

[3] C. H. Tan, S. Xie, & J. Xie “Low noise avalanche photodiodes incorporating a 40 nm AlAsSb avalanche region,” IEEE Journal of Quantum Electronics. Vol. **48**, pp. 36-41, 2012.

[4] S. Ramo, “Currents induced by electron motion,” Proc. I.R. E. pp. 584-585, 1939.

[5] S. Xie, et al. “InGaAs/AlGaAsSb avalanche photodiode with high gain-bandwidth product,” Optics Express. Vol. 24, pp. 24242-24247, 2016.

[6] Texas Instruments. product datasheet: ONET2591TA, Dallas, Texas, USA.

[7] Maxim. product datasheet: 3970, Sunnyvale, CA, USA.

[8] Inphi. product datasheet: IN2844TA, Westlake Village, CA, USA.

[9] Inphi. product datasheet: 4335TA, Westlake Village, CA, USA.